



Towards catalytic measurements of single nanoparticles in situ

A PhD dissertation by

Hjalte Rørbech Ambjørner

Supervisor: Prof. Peter Christian Kjærgaard Vesborg

Co-supervisor: Ass. Prof. Christian Danvad Damsgaard

DTU Physics
Department of Physics
Technical University of Denmark
Fysikvej
Building 311
2800 Kongens Lyngby, Denmark

Preface

This PhD-thesis is written based on work carried out during the author's PhD-project in the ATOMICAR-group at the Department of Physics at the Technical University of Denmark. The project was supervised by professor Peter Christian Kjærgaard Vesborg and co-supervisor associate professor Christian Danvad Damsgaard.

It is the overall goal of the ATOMICAR-group to develop a device, which can facilitate the discovery of nanoparticles with outstanding catalytic properties, and the PhD-project of this author contributed to this development. This thesis reports of work aimed at the development of a chip with arrays of cavities in which catalytic processes can be monitored with ultrahigh sensitivity - an ATOMIC Insight Cavity Array Reactor (ATOMICAR). The author has mainly been concerned with the design, fabrication and characterization of samples, on which the present ATOMICAR-design is based.

During the project, preparations have been made to publish some of the insights gained while developing the ATOMICAR-device, and the draft of an article is included in the appendix of this thesis. It remains a draft (planned to be submitted in February), as focus has been on technical progress rather than on scientific investigations of phenomena discovered during the project. In order to reflect this, the thesis is structured as a guide to the prioritizations made in the design of the present version of the ATOMICAR-device, and it describes and discusses how the device can be build and used.

Kongens Lyngby, 14th December 2021

Hjalte Rørbech Ambjørner

Abstract

The aim of much modern catalysis research is to develop new catalysts, which can be utilized to convert excess green electricity to chemical energy. In pursuit of this goal, the composition and configuration of catalytically active nanoparticles are optimized to obtain the ideal catalyst. However, with presently available methods, it is not possible to measure the catalytic activity of single nanoparticles. Instead, the chemical activity of ensembles of nanoparticles is investigated, making it difficult to establish the true correlation between nanoparticle morphology and activity. If catalysts with extraordinary activities exist within these investigated ensembles, it is not likely that they will ever be discovered. Thus, there is a need for the development of a tool with which the catalytic activity of single nanoparticles can be studied. This thesis describes a new device consisting of a thin free-standing slab with arrays of electron transparent cavities sealed by sheets of few-layer-graphene. It is demonstrated that the total internal pressure of such sealed cavities can be tracked through measurements of the shape of the sealing membrane. Moreover, the partial pressures of gasses captured in cavities of the new device can be monitored via electron energy loss spectroscopy. Utilizing this, the catalytic activity of single nanoparticles can be studied with the novel device, provided that the nanoparticles catalyze a pressure altering reaction. Furthermore, the electron transparency of the cavities can be exploited to correlate the activity of investigated nanoparticles with their structural characteristics. To enable studies of the catalytic activity of single nanoparticles, a new method for isolating a single nanoparticle in a cavity has been developed. With the device, presented in this thesis, the field of catalysis is gaining a tool, which potentially can provide invaluable aid in the search for new catalytic nanoparticles enabling the transition to a sustainable society.

Resumé

Formålet med meget moderne katalyseforskning er at udvikle nye katalysatorer, som kan bruges til at omdanne overskydende grøn elektricitet til kemisk energi. For at nå det mål, bliver sammensætningen og konfigurationen af katalytisk aktive nanopartikler optimeret for at opnå den ideelle katalysator. Med de nuværende tilgængelige metoder er det dog ikke muligt at måle den katalytiske aktivitet af enkelte nanopartikler. I stedet undersøges den kemiske aktivitet af ensembler af nanopartikler, hvilket gør det vanskeligt at fastslå den sande sammenhæng mellem nanopartikel morfologi og aktivitet. Hvis der findes katalysatorer med ekstraordinære aktiviteter inden for disse undersøgte ensembler, er det ikke sandsynligt, at de nogensinde vil blive opdaget. Der er således behov for udvikling af et værktøj, hvormed den katalytiske aktivitet af enkelte nanopartikler kan studeres. Denne afhandling beskriver en ny enhed bestående af en tynd fritstående plade med rækker af elektrongennemsgtige kaviteter forseglet med ark af få-lags grafen. Det bliver demonstreret, at det totale indre tryk af sådanne forseglede kaviteter kan spores gennem målinger af den forseglede membrans form. Desuden kan partialtrykket af gasser fanget i kaviteter i den nye enhed overvåges via elektron-energitabs-spektroskopi. Ved at udnytte dette kan den katalytiske aktivitet af enkelte nanopartikler studeres med den nye enhed, forudsat at nanopartiklerne katalyserer en trykændrende reaktion. Desuden kan elektrongennemsgtigheden af kaviteterne udnyttes til at korrelere aktiviteten af undersøgte nanopartikler med deres strukturelle karakteristika. For at muliggøre undersøgelser af den katalytiske aktivitet af enkelte nanopartikler er der blevet udviklet en ny metode til isolering af en enkelt nanopartikel i en kavitet. Med apparatet, præsenteret i denne afhandling, får katalyseområdet et værktøj, som potentielt kan give uvurderlig hjælp i søgen efter nye katalytiske nanopartikler, der muliggør overgangen til et bæredygtigt samfund.

Acknowledgements

The PhD-project was funded by the European Research Council (ERC) under the European Union's Horizon 2020 research and innovation programme (grant agreement no. 758495). It has been crucial to the project that samples produced throughout the project could be investigated utilizing a transmission electron microscope situated at Haldor Topsoe A/S. This has been made possible by collaborations with the Center for Visualizing Catalytic Processes (VISION), which is sponsored by the Danish National Research Foundation (Grant no. DNRF146), and Haldor Topsoe A/S. In addition to this, facilities at DTU Nanolab – National Centre for Nano Fabrication and Characterization and DTU Physics - Center for Nanostructured Graphene have been used to fabricate and characterize samples.

The list of people, who have been important to my PhD-project, and whom I would like to thank, is long.

Sophie Emilie Rørbech Ambjørner, my wife and soulmate, has given me indispensable support during my PhD-education. She has shared my excitement and frustration about the project, and I am deeply grateful for the advice, academic as well as personal, she has given me. Without her wholehearted support, it would not have been possible to complete the project with this thesis. My family have also aided me extensively, which is both typical of them and much appreciated.

I would like to express my thanks to the rest of the ATOMICAR group: prof. Peter Christian Kjærgaard Vesborg, the postdocs Edwin Dollekamp and Zhongli Wang, and the PhD-students Yanxin Liu and Tobias Georg Bonczyk. In addition, I would like to thank Anton Simon Bjørnlund, PhD-student at VISION. It has been exciting and fun to work closely together with Tobias and Anton, and it has without doubt been a pleasure to share experimental sessions. Edwin, Yanxin, and Zhongli have all provided me with important help, and I appreciate our collaboration and fruitful discussions. I'm grateful for being given the opportunity by Peter to take part in the ATOMICAR-group's interesting activities and for his supervision of my education. His solutions to scientific problems have been inspiring and educational to me throughout the project. I would also like to thank my co-supervisor ass. prof. Christian Danvad Damsgaard, who has also always been helpful and considerate. Although, professor Stig Helveg has not officially been involved in my PhD-education, he has on a nearly weekly basis provided me with help, guidance, and advice, and I'm very thankful for this.

Mads Lützen, Jakob Bruun Pedersen, Anton Lyksborg-Andersen, and Thomas Erik Lyck Smitshuysen have all been a part of my daily life at DTU, both before

and during my PhD-education. I have enjoyed our discussions about life, science in general, and politics, and I look forward to more.

I'm thankful for the technical advice and help that I have received from the staff at DTU Nanolab, and for the invaluable technical support provided by Sven Ullmann and Sebastian Pirel Fredsgaard Jespersen from Haldor Topsoe A/S. The project could not have progressed as it did, if it were not for their help. Finally, I would like to thank Poul Lenvig Hansen for making it possible that I could spend my external stay at Haldor Topsoe A/S.

Abbreviations

TEM	Transmission Electron Microscope
EFTEM	Energy Filtered Transmission Electron Microscope
AFM	Atomic Force Microscopy
AM-AFM	Amplitude Mode - Atomic Force Microscopy
CM-AFM	Contact Mode - Atomic Force Microscopy
EELS	Electron Energy Loss Spectroscopy
SEM	Scanning Electron Microscopy
FLG	Few-Layer-Graphene
FEG	Field Electron Gun
E-cell	Environmental cell
GIF	GATAN Image Filter
ET	Everhart-Thornley

Contents

Preface	i
Abstract	iii
Resumé	v
Acknowledgements	vii
Abbreviations	ix
Contents	xi
1 Introduction	1
1.1 Motivation	1
1.1.1 The need for energy	1
1.1.2 The role of catalysis and a new tool	2
1.2 Background	3
1.2.1 What is catalysis?	3
1.2.2 The task of modern catalysis	5
1.2.3 The optimal catalyst is small	5
1.2.4 The catalysts respond to their surroundings	7
1.2.5 State of the art	8
1.3 Aim of the study	12
2 Methodology	15
2.1 Electron microscopy	15
2.1.1 Transmission Electron Microscopy	18
2.1.1.1 Electron Energy Loss Spectroscopy in the TEM	21
2.1.1.2 Energy Filtered TEM	26
2.1.2 Scanning Electron Microscopy	26
2.2 Atomic Force Microscopy	28
2.3 Cleanroom fabrication techniques	32
2.4 FLG transfer	35

3	ATOMICAR-design	37
3.1	Graphene: An impermeable seal	40
3.1.1	Measurement of the internal pressure of a FLG-sealed SiO ₂ cavity	41
3.2	How should an ATOMICAR-device be structured?	50
3.2.1	3D structure of the ATOMICAR-design	54
3.2.2	Fabrication procedure	59
3.3	Isolated single nanoparticles	63
3.4	Monitoring the internal pressure with EELS	65
3.5	Ongoing work	70
4	Discussion & Conclusion	73
	Appendix	76
	Bibliography	97

CHAPTER 1

Introduction

1.1 Motivation

1.1.1 The need for energy

In 2018, 79,801 people were employed within the Danish agricultural sector ([1]). Despite this small number, the Danish Agriculture & Food Council stated in a report from 2019 that the Danish food production can feed 15 million people ([2]). This enormous surplus of food is an example of the general material wealth of the western countries, in which the production of goods has skyrocketed the last centuries ([3]). With the aid of machines and large energy reserves, the material wealth that can be produced per person can reach astronomical scales. All over the globe, countries have exploited this fact to increase the amount of wealth that can be distributed within and across these nations. The benefits of this development are obvious, but the huge consumption of energy that has accompanied it is problematic.

Today, the global energy consumption is primarily based on coal, oil, and gas ([4]). Unfortunately, this use of resources risks the general stability of the climate due to the impact of the derived emission of CO₂ (and other green house gasses) on the climate ([5]). In response to this, there has been an increasing political demand for increased energy efficiency and a shift to alternative energy sources. This is exemplified by the Climate law of EU, which legally binds EU to become climate neutral by 2050 ([6]). The shift to alternative energy resources is a necessity, if the material wealth is to be sustained during such a transition.

Although the relationship between economic growth and energy consumption is under debate in economic literature ([7]), it is not a purely economic or political issue. Whenever a wheel turns or any work is carried out, energy is consumed. This is a simple law of nature; the first law of thermodynamics ([8]). The specific size of our society's energy consumption is a political issue, but it is a fact of nature that we need an energy source in order to sustain any material wealth. Accordingly, the development of alternative energy sources is an important scientific task. Indeed, there has been considerable technical progress during the last couple of decades, and as a result of that, a greater part of our electrical energy stems from sustainable sources such as solar- and windpower ([4]). Unfortunately, sustainable sources are nowhere near our largest source of energy, and their intermittency prevents them from being so (see the following section). When looking for disciplines of science, which could

present further developments, the field of catalysis is an obvious candidate. With catalysis, the speed of chemical reactions can be optimized and, as will be argued below, some of the obstacles that hinders a transition to a sustainable society could be overcome with efficient chemical synthesis of “green” fuels (used here as designating fuels without an overall negative impact on the climate).

1.1.2 The role of catalysis and a new tool

Sustainable electricity has received much attention in the recent decades, but a transition to a global sustainable energy consumption is not likely to be achieved only through carbon-neutral electricity. Commercial transportation is difficult to electrify, and the chemical industry relies heavily on fossil fuels ([9]). Furthermore, the energy production from important sustainable energy sources like solar- and windpower is inherently unstable: electricity is only produced when the sun shines or the wind blows. Different strategies have been suggested to address these challenges, but synthesized green fuels would be able to solve all of the listed issues. By using excess electrical power to store energy in chemical bonds (hydrogen, methane, methanol) and synthesize important ([10]) chemicals, such as ammonia, the use of fossil fuels could be phased out ([11]). This strategy of energy conversion is often referred to as power-to-X (P2X ([11])), X being the product synthesized. Catalysis plays an essential role in P2X, in fact it is the “2” in P2X.

By definition, a catalyst is a compound that enhance the reaction rate of a chemical reaction without itself being consumed ([10]). Catalysts are omnipresent both in biological organisms and in the chemical industry, and the present importance is difficult to overestimate. Catalysis is already an important factor in the refinement of oils, just as it is in the mitigation of the environmental consequences of the use of fossil fuels ([10]). The rate, at which synthetic fuels can be produced, is vital for the success of P2X and the green energy transition. In order to meet the daily need for energy and chemicals, catalysts must be utilized to enhance the reaction rate of the chemical processes involved in P2X.

Since Earth is a bounded system, we only have limited amounts of steel and rare earth elements for wind turbines, solar cells or other energy producing technologies. This puts constraints on the amount of electrical energy that can, even potentially, be produced. In ref. [12] Vesborg et al. concludes that it takes about 50 years of dysprosium production to scale the energy production from wind turbines to a level just comparable to the global consumption of energy. Technological innovations may change this number, but the conclusion is the same; the amount of electrical energy that we can produce is limited. As a result, P2X technologies must be energy efficient in order to be able to produce enough products to fulfill the global need. If only a small part of the electrical power, consumed by the P2X process, is used to produce the desired product, the need for electricity increases. Since the total available electrical energy is bounded, the resulting amounts of the product produced may not suffice. Furthermore, the rate at which the product is formed determines the scale at which

the P2X process has to take place to keep up with energy demand. Thereby energy efficiency and reaction speed are important parameters for the applicability of the synthesis of green fuels and chemicals. Since catalysts can enhance the reaction rate, and thus the energy efficiency of chemical processes, it follows that the development of P2X technologies is, in its essence, a matter of finding good catalysts.

Different types of catalysis exist, although this thesis will only focus on so-called heterogeneous thermal catalysis (chemical reactions taking place on the surface of a solid driven by thermal energy) for solid catalysts and gaseous reactants. The exclusion of other subjects is not due to their lack of importance, but because this thesis describes work aimed at the development of a new tool for the field of heterogeneous thermal catalysis. Today, it is not possible to measure the catalytic performance of single catalytic particles of relevant sizes. Instead, thousands of particles are characterized with respect to their catalytic activity at the same time, and then the accumulated catalytic performance is interpreted through structural and compositional analysis of single particles. This is problematic as the catalytic performance differ from particle to particle. Consequently, the field of catalysis aims at optimizing the activity of single particles without monitoring it. Instead, the accumulated activity of several particles is assumed to be representative for a single particle. This thesis describes the partial development of a new tool, which could solve this problem. Before the concept of the tool is described in Section 1.3, the capabilities that such a tool must have, as well as previous efforts to measure single particle catalysis will be briefly introduced in the following section.

1.2 Background

1.2.1 What is catalysis?

As mentioned in the previous section, a catalyst is a compound that accelerates a chemical reaction. Preferably, this is carried out with minimal loss of energy to the production of unwanted byproducts. In Figure 1.1, the effect of a catalyst on a chemical reaction is illustrated. The reaction with and without a catalyst is illustrated for a reaction in which two reactants, A and B, form the products C and D. The stippled line in Figure 1.1 marks the reaction path without a catalyst. It shows that in order to progress from the energy state of the reactants to that of the products, a large energy barrier has to be overcome (stippled line). As a result, abundant amounts of energy must be supplied to the reactants, for their energy to be raised above the energy barrier. Note that the energy landscape also describes the reaction from the chemical species C and D to A and B. Consequently, a chemical equilibrium is established, when A and B is converted to C and D at the same rate as the reverse reaction takes place. A catalyst does not change the equilibrium concentrations of chemical species, but it provides an alternative route for the reactants through the energy landscape on its surface ([10]). Through this alternative route, the reaction can

proceed faster, due to the lower energy barriers on the path, and chemical equilibrium is reached faster. Catalysts are often composed of metals and are dispersed as small particles on a support that either enhance the property of the catalysts or simply acts as a carrier. The geometrical position, in which the catalytic reaction proceeds on the surface of the catalyst, is defined as "the active site".

The relation between the reaction rate constant (determining the relationship between concentration of reactants and chemical reaction rate), k , of a reaction and an energy barrier height can be described by an Arrhenius equation ([10]):

$$k = \nu(T) e^{\left(\frac{-E_a}{k_b T}\right)}, \quad (1.1)$$

where ν is a prefactor dependent on temperature, T , k_b is the Boltzmann constant, and E_a is the activation energy, i.e. the energy barrier that reactants need to surmount in order to be converted to products. This energy barrier is in transition state theory the potential energy barrier for a single reaction step ([10]). Furthermore, catalysts also control the amounts of undesired side products that the reactants can combine to - a catalyst has a certain "selectivity". This has huge implications for the energy efficiency of the reaction. Today, known catalysts cannot facilitate sufficiently energy effective and fast synthesis of green fuels to meet the society's needs. Therefore, the present task for the field of catalysis is to identify new types of catalysts. If these are to be identified experimentally, we need to look for catalytic particles with outstanding catalytic activity and selectivity, i.e. measure the catalytic activity of single particles, as argued in the following sections.

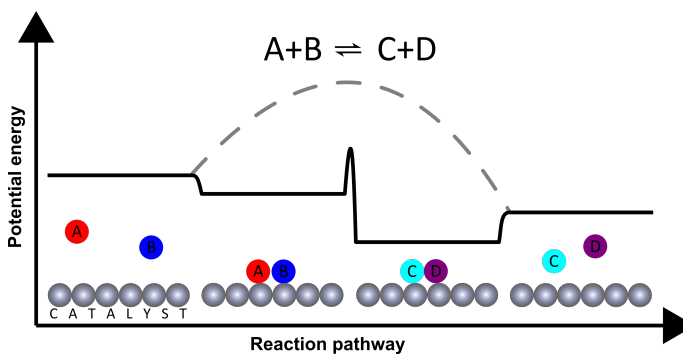


Figure 1.1. Sketch of the action of a catalyst on the energy landscape of a reaction between the reactants A and B forming the products C and D. Without the catalyst, the reaction is slowed by a high energy barrier (stippled line), but when the catalyst provides a modified path with lower barriers, the reaction can run faster. Figure inspired by ref. [10]

1.2.2 The task of modern catalysis

Modern catalysis is faced with a difficult task. Theoretical research has revealed that the binding energy of reaction intermediates are not independent of each other, e.g. the binding energies of CH, CH₂, CH₃ on transition metals are all linearly dependent on the binding energy of a carbon atom ([13]). This relationship between reaction intermediates is called scaling relations. The dependencies translate to free energy paths ([14]), in which the intermediate steps of a reaction cannot independently be optimized ([15]). Unfortunately, the scaling relations rarely allow for optimal combination of bonding energies of intermediate reactants. The task is therefore to find new types of sites for the catalytic reactions of interest ([15][16]). As a result of this, immense work has been conducted in order to invent new catalysts that deviate from common scaling relations, such that the optimal parameters for catalysis can be achieved (e.g. : [17][18][19]).

A supplementary approach to the theory-guided invention of new catalysts, is to measure the catalytic activity of single catalytic particles, and thereby gain insights that could pave the way for the design of new catalysts. Prepared catalytic particles often vary in both size and shape, and it is highly probable that they also deviate in catalytic reactivity as a result of that. This is plausible as huge differences in catalytic activities have been observed in studies where either the support of the particles, the particles' strain or composition have deliberately been tuned on ensemble level ([20]). Unfortunately, the methods used for measuring the catalytic activity suffer from ensemble-averaging. The catalytic activity is measured as a collective property of a huge number of particles, and this makes it impossible to identify particles with outstanding catalytic properties. Furthermore, it is not possible to correlate the activity and particle structure on particle level. By measuring on a single particle basis this problem is avoided. Many different strategies have been employed in order to measure the catalytic activity of single catalytic particles, including, but not limited to, single-molecule fluorescence microscopy, electro-chemical scanning probes, and surface plasmon resonance spectroscopy ([21]). Work representative for the different approaches is reviewed below in Section 1.2.5. Before the state of the art of research on single particle catalysis can be reviewed, the nature of modern catalysts has to be briefly described. This description will then be used as a basis for evaluating to which extent the state of the art can deliver the knowledge about single particle catalysis that is needed.

1.2.3 The optimal catalyst is small

As described in the previous section, catalysis takes place at the surface of the catalyst, and the size of the active site is comparable to the size of the reactants and products (few atoms wide). This combined with the fact that catalytic metal particles are faceted, due to the crystalline nature of metals, often makes the optimal catalytic particle very small. Atoms bound in different facets experience a varying number

of adjacent atoms, and especially atoms at transitions between facets are bound to less neighboring atoms. This has huge implications for the reactivity of the different atoms on the particle. Atoms with fewer neighboring atoms are more reactive ([22]), meaning that they form stronger bonds with reactants. The strength of catalysts' bond to reaction intermediates is often linearly related to the activation energy for achieving these reaction intermediates. Such a linear relationship is referred to as a Brønsted–Evans–Polanyi relation ([10]). As a result, the more energetically favorable the final state of a reaction is compared to the initial state, the lower the activation energy is, and the faster the reaction proceeds through the reaction step on the catalyst. Reducing the size of the catalytic particles increases the percentage of atoms with fewer neighboring atoms with the consequent higher percentage of reactive metal atoms. However, there is a limit to how reactive the optimal catalytic particles are. If the products are too strongly bound to the catalytic substrate, the products are more likely to be stuck at the surface, as described with a Brønsted–Evans–Polanyi relation with a negative proportionality factor. Consequently, the effect of adsorption and desorption need to be balanced in order to achieve the optimal catalyst ([22]). The size of noble metal catalysts has been observed to influence the rate of product formation in numerous different catalytic reactions ([23]). Notably gold, otherwise regarded as inactive, becomes active for CO oxidation when organized in sufficiently small particles ([24]).

From the above, it is clear that catalysts should be small to maximize catalytic activity, but in addition to this scientific argument, there is also an economic reason for reducing the size of catalysts. Catalysts often consist of expensive metals e.g. palladium, rhodium and platinum ([10]). As a result, the optimal particle size is, in general, small, due to the fact that catalysis takes place on the surface of the catalyst (the surface area of the catalytic particle is increased compared to its mass, when the diameter is reduced). For some reactions, it can be advantageous to reduce the particle size below a few nanometers, and recently there has been much effort in determining the reactivity of extremely small particle sizes ([25]). In these size ranges the description of the catalyst as a metal breaks down, but for the sake of this work, the important conclusion is that the optimal size of catalytic particles in general is about 10 nm or even smaller ([23][25]). As catalysts essentially are nanoparticles and the active sites are composed of a few atoms, a sub-atomic spatial resolution is necessary to characterize the catalytic performance of catalysts. Another consequence of the size of catalysts, is that it is difficult to isolate them from other catalysts once an ensemble of catalysts have been synthesized. This is why single particle catalysis measurements pose a difficult challenge. In addition to this, catalysts respond to their environment. This in effect adds the additional requirement that a tool, made to examine the catalytic activity of single particles must be able to facilitate the study of the catalyst, *while* it catalyses a reaction. Experiments need to be carried out *in situ*.

1.2.4 The catalysts respond to their surroundings

The environment surrounding a nanoparticle can have pronounced influence on the shape of the particle. As an example of this, Cu particles dispersed on ZnO have been shown to reversibly change shape at 220°C, when they are alternately subjected to gas atmospheres of either pure H₂ or H₂/H₂O (3 : 1) at 1.5 mbar total pressure ([26]). The fact that the particle shape changes are reversible, underlines the need for *in situ* studies. Since the shape changes are not permanent, they can only be observed under the conditions that create them. Adsorption of gas molecules on a crystal facet changes the surface energy of that facet, which in return affects the equilibrium shape of the particle. This is of great importance of the catalytic activity, as different particle shapes have different catalytic activities, due to the difference in exposed facets and edges. The nature of the attachment of nanoparticles to their support also depend the environment of the catalysts. At 5 mbar of H₂/CO (95 : 5) Cu particles show increased wetting of the ZnO support as compared to in a pure H₂ atmosphere ([26]). In conclusion, the environment surrounding a nanoparticle can affect the shape both through interaction with the support of the nanoparticle and with the nanoparticle itself.

Even during a reaction, a variation in gas composition can induce morphological changes in a catalytic particle. In 2014, Vendelbo et al. ([27]) presented images of platinum particles' oscillatory shape changes during CO oxidation in a plug-flow reactor. They noted that the extent of the changing morphology depended on the particle size and position, indicating that local gas compositions had a large effect on the behaviour of the platinum particles. This is an example further emphasizing the need for *in situ* studies. As the reaction itself alter the local environment of the catalytic particle, which again affects the particle, the catalytic mechanism of a particle is not always accurately represented in studies in which no reaction takes place during measurement.

The fact that the temperature, pressure, and chemical species of the environment of the catalyst changes the equilibrium particle shape can be understood by examining the equilibrium coverage, θ_A , of a non-reacting species A on a surface:

$$\theta_A = \frac{K_A p_A}{1 + K_A p_A} \quad K_A(T) = e^{\left(\frac{-\Delta G^\circ}{RT}\right)}. \quad (1.2)$$

Here p_a is the partial pressure of the species, and K_A , the equilibrium constant, depends on the temperature, T , and the energy gained or lost in the reaction of adsorption, ΔG° , via the gas constant, R . The higher the pressure, the higher the coverage at a specific temperature. The higher the temperature, the lower the coverage of the species A (provided ΔG is negative). The coverage of the A species on a surface changes the energy, γ , of that surface - the surface energy ([28]):

$$\gamma = \gamma_{surface} + \theta_A \cdot \frac{E_{ads}}{A_{at}}. \quad (1.3)$$

Here $\gamma_{surface}$ is the energy of the surface without adsorbates, and E_{ads} and A_{at} is the energy associated with adsorption and the area of an atom on the surface, respectively. The most stable configuration of a particle is the shape, which minimizes the surface energy. E_{ads} and $\gamma_{surface}$ can vary from crystal facet to crystal facet, and therefore the most energetically favorable particle shape depends on the coverage of reactants on the catalyst. Equation 1.2 and 1.3 indicates that in general, the conditions under which catalysis takes place alters the performance of the catalyst through changes of the particle. This phenomenon have been observed in a number of studies ([29]), and single particle studies must seek to investigate catalysis at temperatures, pressures and gas composition mimicking industrial relevant conditions.

The fact that reactions have to be studied while they proceed put high demands on the equipment used to characterize the catalysts. It is very difficult to study catalysts with sufficient spatial resolution at pressures close to ambient, and usually synthesis of chemicals takes place at much higher pressures. Methanol is often perceived as an attractive green fuel ([30]), but it is often synthesized at 200 – 300°C and 3.5 – 10 MPa ([31]), making it difficult to study at the formation of methanol *in situ* at industrially relevant conditions. Potentially, without the possibility to investigate catalysis under high pressures and temperatures, the field of catalysis could miss important information that could drive the development of new catalysts. As a consequence, single particles studies should allow *in situ* studies at industrially relevant conditions. In the following Section 1.2.5, the state of the art of single particle experiments will be briefly reviewed. Here the focus is both on how single particles are studied, but also on whether the conducted experiments potentially could be representative for catalysis carried out under industrially relevant conditions. Furthermore, as described in Section 1.2.3, the optimal particle size is small, and small particles need to be studied if the dynamics of industrial synthesis is to be mimicked. Finally, sub-atom spatial resolution is needed to study the active sites of catalysis.

1.2.5 State of the art

There have been many attempts to reveal the dynamics of catalysis at the single nanoparticle level, and single-molecule fluorescence microscopy is a very popular approach. In 2008, Xu et al. ([32]) studied the conversion of resazurin to the fluorescent resorufin over gold nanoparticles approximately 6 nm in diameter. The gold particles were immobilized on a glass slide and exposed to the reactant molecules in a solution. Fluorescent molecules were excited with a laser experiencing total internal reflection on the backside of the glass slide. Small bursts of fluorescence were attributed to single events of catalytic conversion of reactants, and the kinetics of the reaction was studied as a function of reactant concentration. This study illustrates both the pros

and cons with single molecule fluorescence microscopy. As the studied reaction itself generates the signal, one can obtain unparalleled spatial resolution of the catalytic reactivity and several particles can be investigated simultaneously. However, the method requires the product to stay attached to the catalytic particle long enough to be imaged, which limits the reaction conditions that can be studied. The particles release product molecules into the same volume, if the particles are not isolated, and thereby the location of the catalytic conversions can only be identified at very low conversion rates. Finally, the particles cannot be examined with sufficient resolution to relate catalytic performance with structural descriptors.

Some of these problems are addressed with great success with the design of a nano-fluidic device by Levin et al. ([33]). In this design, silicon fabrication techniques were used to create micro channels in an oxidized silicon wafer, and gold nanoparticles were deposited with electron beam evaporation. Finally, the micro channels were sealed by fusion bonding a pyrex lid to the structures. With this device, single nanoparticles of different sizes (nm-range) could be studied under the same flow conditions. The catalyzed reduction of fluorescein was studied on gold nanoparticles of different sizes, and both the effect of reactant concentration and particle size could be investigated for single particles not influencing each other. Another approach has recently been employed to study the conversion of resazurin to the fluorescent resorufin on single CdS nanoparticles ([34]). In this study, nanoparticles were immobilized on a glass slide and isolated from each other in microwells by a PDMS sheet with cavities. Differences in catalytic activity could be observed from microwell to microwell, and high concentrations of reactants could be used as the method did not rely on single conversions to be distinguishable. In both studies, the catalytic conversion was measured at the single particle level and heterogeneity of nanoparticle activity could be observed. While both studies are examples of clever engineering and experimental design, they do not allow characterization of single nanoparticles with sufficient spatial resolution. As the active sites are atomically small, such spatial resolution is needed to correlate the impressively local measurement of catalytic activity with the structure of the nanoparticle. This inhibits the knowledge that can be gained, if a promising single particle is identified. In addition to this, it is not obvious how knowledge gained on the catalysis of fluorescent molecules is applicable in the design of better catalyst for e.g. methanol synthesis. While a lot of knowledge can be gained about the specific processes studied, it is not clear whether these studies are representative of catalytic processes carried out in industry. This is problematic, because, as described above, the catalytic performance of particles is altered by process conditions, and therefore knowledge gained for one process might not be relevant for other processes.

Instead of isolating nanoparticles from the surrounding environment, Lai et al. ([35]) limited the extent of the volume of the reactants to sizes smaller than the distance between their studied nanoparticles. Scanning electrochemical cell microscopy was performed on particle level, by using a cone with two chambers connected through a droplet of air-saturated electrolyte at the end. This imaging technique makes it possible to visualize and correlate the positions of nanoparticles with regions exhibiting electrochemical activity. The conductivity between the two chambers was measured

at different potentials while the droplet was scanned across platinum nanoparticles (approximately 100 nm in size) dispersed on a long carbon nanotube situated on a SiO₂ surface. The current flow between probe and sample surface was measured and related to the catalytic reaction of hydrogen evolution or oxygen reduction, depending on the potential of the scanning probe. The conductivity of the droplet changed, when a platinum particle entered the electrolyte droplet, and in this way catalytic activity was determined with approximately 1 micron spatial resolution and could be correlated with nanoparticle positions. These nanoparticles could then be examined in a scanning electron microscope, and the relation between overall morphology and activity could be discussed. This method makes it possible to measure relevant electrochemical reactions on a single particle basis, which in itself is quite impressive. Still, the nanoparticles were not examined with sufficient spatial resolution with electron microscopes to reveal specific sites, all though scanning electron microscopy images could give important information. If the experiment was carried out on an electron transparent substrate, it would be possible to solve this issue. However, this method does not allow for spatial *in situ* characterization of the nanoparticles, and as a result this method can only reveal which appearance particles with outstanding catalytic activities have, when no catalysis is taking place.

X-ray techniques can offer both compositional, chemical and structural information about single nanoparticles at elevated temperatures and pressures ([21]). The capabilities of X-rays techniques can be exemplified by a recent study, in which the strain of the facets of a Pt₆₀Rh₄₀ particle (approximately 100 nm in diameter) was examined during CO oxidation at 700 K and 50 mbar (8 : 4 : 38 mixture of CO : O₂ : Ar). The strain changed during reaction, which via simulations was interpreted as a result of migration of Rh to the surface of the particle. In this study, the particle was not isolated from other particles and the activity was still investigated for the whole ensemble of particles. In order to achieve information from single isolated nanoparticles in a parallel manner appropriate reactors needs to be designed. Such a device has not been designed yet, to this author's knowledge, but it is not in principle impossible. The spatial resolution is however few nano-meter for X-ray methods ([36]), making it difficult to identify the reactive sites experimentally solely with X-ray techniques.

Other optical methods are also being developed to probe catalysis at the single particle level. Single particle plasmonics is an example of that. The plasmon frequency of small particles is very sensitive to the structural or chemical changes close to the particle. This has been exploited to gain information about catalytic behaviour on small length scales ([37]). Similarly, plasmon enhanced raman spectroscopy is also being developed to investigate single particle phenomena. However, the general problem for these two techniques is that the signal for single particles is very low. This is often solved by so-called "antennas", larger structures with greater signal intensity or other structures that enhance the signal in the neighborhood of the particles of interest ([37][38]). The locality of the measurement is then dependent on the size of these antennas or enhancers, and sufficient spatial resolution cannot be obtained. If this problem was solved, these two optical methods could be combined with the nano-fluidic device by Levin et al. ([33]) with isolated single nanoparticles. In this

way, both the requirement that experiments should be carried out under relevant *in situ* conditions and that characterization of the single nanoparticles should be carried out with sub-atomic resolution would be met.

In 2021, a new approach to single particle catalysis was presented by Suchorski et al. ([39]). In their study, *in situ* field electron microscopy was used to examine hydrogen oxidation on different facets of a curved rhodium rod 650 nm in radius. The investigations revealed facet depending catalytic rates, and the interaction between different facets and reaction fronts. Using field ion microscopy, the ionized reaction product H_2O was used to visualize the reaction. The method can only be utilized at low pressure (10^{-5} to 10^{-6} mbar in this study), as pressures approaching ambient pressures will obscure signal collection. Furthermore, this method does not allow investigation of the active sites with appropriate resolution.

With miniaturized flow-reactors, developed during the last decades, catalysts can be studied *in situ* with atomic resolution in transmission electron microscopes through electron transparent windows (e.g. [40][41][42]). This type of reactors have been instrumental in investigations of the catalytic activity of nanoparticles (e.g. [26][27][43][44]), and they will probably remain to be. Importantly, none of them allows activity studies of single nanoparticles, and therefore they cannot solve the scientific challenge described in this chapter.

The methods described in the previous can without doubt be combined in ways in which they compensate each others pros and cons, thereby important insights can be gained. Furthermore, experimental limitations can often be compensated for with simulations to obtain knowledge enough to improve the performance of catalysts. However, such studies have not yet solved the problem of finding new catalytic sites. In this thesis, the development of a new tool, which can facilitate measurements of single particle catalysis, is described. It is the hope that a finalized tool, will pave the way for discoveries of important new catalytic sites.

1.3 Aim of the study

To sum up, there is need for the development of a tool that can facilitate measurements of the catalytic activity of single particles to reveal particles with outstanding catalytic performance. In addition to this, the developed device should allow for a subsequent characterization of promising particles, in order to identify active sites responsible for the exceptional catalytic activity. As argued, characterization and inspection of particles with atomic resolution is necessary, if new active sites are to be found experimentally. Furthermore, catalytic measurements should be conducted at temperatures and pressures representative for industrial conditions. The design that is suggested by Prof. Peter Christian Kjærsgaard Vesborg to fulfill this goal is sketched on Figure 1.2.

Conceptually, the design is very simple. A slab with an array of cavities is used as a carrier of the particles to be studied. In the cavities of the device, nanoparticles are isolated from the environment by a membrane covering the front surface of the slab. By insuring low coverage of particles on the surface of the device before sealing, a single (to a few) particle(s) can be studied individually. In principle, reactants can be introduced both during sealing of the cavities or subsequently, if the leak rates are finite. The membrane, covering the cavities, will deflect in response to a pressure change, and by tracking the shape of the membrane, the total conversion of reactants to products can be studied for reactions that alters the pressure (methanol synthesis, methanation, ammonia synthesis and many more). After the initial screening of the catalytic performance, promising particles can be investigated with sub-atomic resolution with a transmission electron microscope through electron transparent cavity

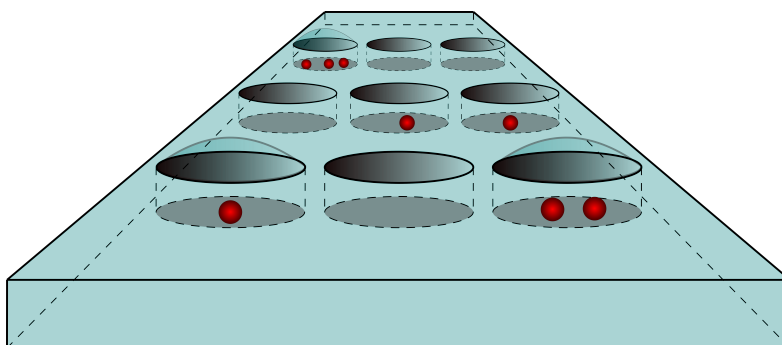


Figure 1.2. Reactor for catalytic screening of single particle catalysts. Cavities with few nanoparticles are sealed with a thin membrane, which bulges depending on the pressure difference across the membrane. The strain of the membrane indicates the conversion of products for reactions, in which the number of molecules changes during reaction. Spectroscopy can be employed to study the evolution of different gas species, while electron transparent bottoms of the cavities facilitate sub-atomic spatial resolution.

bottoms. The author of this thesis has been responsible for the design and fabrication of the slab, while other members of the ATOMICAR group have focused on the development of the membrane and the transfer of the membrane to the slab. The aim of this thesis, is to describe efforts by the author aimed at the realization of a device such as that presented in Figure 1.2. In Chapter 2 of the thesis, the methods used to characterize the devices produced are presented. Chapter 3 describes the fabrication of the present version of the device, and its capabilities. ATOMICAR is an abbreviation for Atomic Insight Cavity Array Reactor, and in this thesis, devices based on the design shown in Figure 1.2 is referred to as an "ATOMICAR-device".

CHAPTER 2

Methodology

All of the features investigated in this thesis are too small to be visually inspected. Nanoparticles are small, obviously, and so must the structures of the ATOMICAR-design be (described in Section 3). As a result, a combination of optical microscopy, Atomic Force Microscopy (AFM), Scanning Electron Microscopy (SEM), and Transmission Electron Microscopy (TEM) have been employed to inspect and characterize the surface, cross section and projection of the fabricated ATOMICAR-devices. The following sections provide a theoretical background, sufficient for a discussion of the data obtained with the listed microscopy techniques. Optical microscopy is not considered, as optical images often are intuitive to interpret. Electron microscopy is first described, and then follows a section about AFM. Finally, cleanroom fabrication techniques used to construct ATOMICAR-devices are described. The sections only describe the type of equipment used in the PhD-project, which forms the basis of this thesis. The only exception is Section 2.4, which briefly sketches, how Few-Layer-Graphene (FLG) can be transferred to a sample. As described in Chapter 3, thin sheets of FLG are used to seal the ATOMICAR-devices, and superficial background knowledge about FLG-transfer techniques is necessary to understand, why the ATOMICAR-devices are structured, as they are. During the PhD-project, Zhongli Wang and Edwin Dollekamp (postdocs of the ATOMICAR-group) were responsible for transferring sheets of FLG to ATOMICAR-devices. This chapter does not at all exhaustively describe the capabilities of the equipment used. In an attempt to keep the thesis relatively concise, the descriptions are kept brief.

2.1 Electron microscopy

The spatial resolution, δ , of a microscope is one of its most important characteristics. For microscopes using radiation to generate images, the Rayleigh criterion ([45]) can be used to estimate the relation between resolution and the wavelength of the radiation:

$$\delta \propto \lambda. \tag{2.1}$$

In this equation, λ is the wavelength of the radiation used for imaging (light/electrons). By reducing the wavelength, the resolution can be improved. Every particle has an associated wavelength, and this fact can be described by the de Broglie wavelength ([45]):

$$\lambda = \frac{h}{p}, \quad (2.2)$$

where h and p are Planck's constant and the momentum, respectively. In conclusion, the larger the momentum of the radiation, the better the resolution. Electrons are charged particles, meaning that they can easily be accelerated. In electron microscopes, the electrons are accelerated to high velocities (greater than half the speed of light [45]) and the resulting resolution, determined by the electrons' wavelength, is smaller than atoms. In reality, the resolution of electron microscopes is not limited by the wavelength of electrons, but by imperfections in the lenses used in electron microscopy ([45]).

In electron microscopes, an electron gun delivers electrons to the condenser system, which illuminates the sample of interest. There exist different types of electron guns, but for both the SEM and TEM used for this thesis, the gun is a so-called "Field Emission Gun" (FEG). A biased extractor anode in front of the FEG creates a constant current of electrons emanating from sharpened tip of the FEG. Further down the electron microscope column, a second anode accelerates the electrons to the desired kinetic energy and associated wavelength ([45]). In the case of this work, electrons are accelerated to 300 keV in the TEM and to energies between 10 keV and 30 keV in the SEM. After the electrons have been emitted from the electron gun, subsequent electron lenses are used to control the total current in the electron beam and the area of illumination on the sample. The manipulation of the electron trajectories in electron microscopes can be understood through two equations (Lorentz and Ampère's law for a constant electric field) ([46][45]):

$$F = e(E + v \times B) \quad \int J \cdot dA = \oint H \cdot dl. \quad (2.3)$$

Here e is the elementary charge, E is the electric field, v is the velocity of the electrons, B and H are the total magnetic field and the magnetic field without magnetization, respectively, and J is current. The first equation states that the trajectory of electrons can be controlled with either an electric field or by a magnetic field perpendicular to the direction of motion of the electron. Electrical currents create magnetic fields, as described by the second equation, and this is exploited to create electromagnetic lenses. Electrostatic lenses are in general used to deflect the electron beam, whereas magnetic fields are used to focus and diverge the beam.

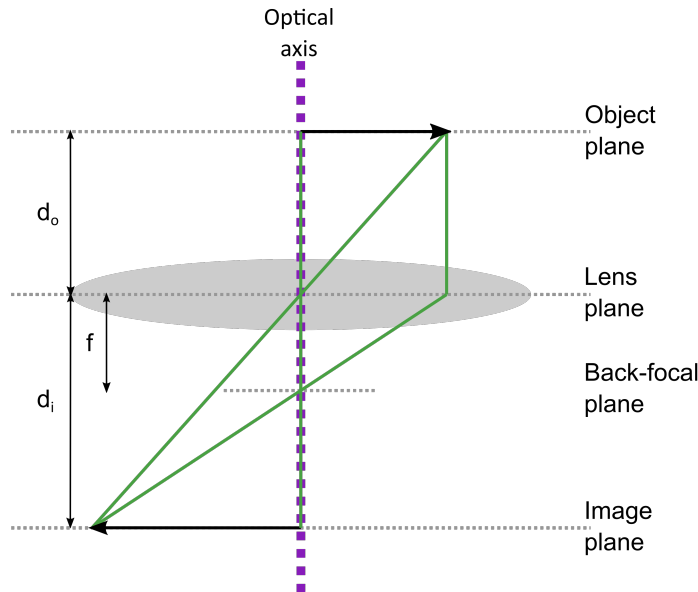


Figure 2.1. Illustration of the imaging of an arrow with electrons using an electromagnetic lens. An arrow is positioned in the object plane of the lens and illuminated by electrons. The electromagnetic lens then bends the trajectory of the transmitted electrons (green lines) to create a magnified image of the arrow in the image plane. All electrons bend to the same angle by the object (the arrow), are focused to the same point in the back-focal plane. Figure based on ref. [45]

The action of a lens on the motion of electrons is sketched in Figure 2.1. In this example, the electron lens creates a magnified image of an arrow positioned in the object plane. The axis of symmetry of the lens is called the optical axis, and in Figure 2.1 it is indicated with a purple line. This axis needs to be aligned for subsequent lenses, if the image of the object plane is to be mapped from one lens to the other without distortions. An electron lens focuses electrons originating from a point in the object plane to a point in the image plane, but during focus, all electrons travelling from the object plane with the same angle to the optical axis pass the same point in the back-focal plane. This is also shown in Figure 2.1. The plane in front of the lens, at the same distance to the lens as the back-focal plane, is called the front-focal plane (not drawn on Figure 2.1). This plane is very important for the illumination in the TEM. The distances from object to lens (d_o), from image to lens (d_i), and from lens to focal plane (f) are not independent. These distances are related through the lens equation ([45]):

$$\frac{1}{f} = \frac{1}{d_o} + \frac{1}{d_i}. \quad (2.4)$$

In practice, both d_o and d_i for the whole system of lenses are fixed in electron microscopes, as the geometrical position of the electron gun and sample are fixed (if the sample is required to be at a specific distance to the image forming lenses - called eucentric height ([45])). The image plane of the first lens is then the object plane of the next, and only f is actually controlled for each lens. Increasing the focusing power of a lens reduces its focal length, and then the image of the object moves closer to the lens, if the object is not moved. In this case, the image is demagnified ([45]):

$$\text{Magnification} = \frac{d_i}{d_o}. \quad (2.5)$$

Several lenses are combined in sequence to magnify or demagnify the electron beam on the sample or the electron detector (in the case of the TEM). In SEMs, an objective lens is used to focus the electron beam to a small spot on the sample, and different detectors are used to collect electrons travelling back from the sample surface ([47]). Conversely, in TEMs the transmitted signal is used to form images of the sample and the electron detector(s) is/are mounted below the sample ([45]).

Both in SEMs and TEMs, it is important that the density of gas molecules is low all the way down the microscope column. Otherwise, the beam electrons will scatter on the gas molecules, and the microscopes' ability to focus will deteriorate drastically. The SEM used for this thesis is always operated with a pressure at the sample below 10^{-2} Pa, whereas the pressure at the sample is below 10^{-5} mbar, unless otherwise specified, when the TEM is used.

2.1.1 Transmission Electron Microscopy

For this thesis, a FEI Titan 80-300 ETEM ([48]) was used. TEMs vary in construction, but here, only this type of TEM is considered. The TEM is constructed, such that gas can be led into the immediate surroundings of samples inserted into the TEM. Pumps and apertures ensure that the gas pressure quickly drops outside the region containing the sample, and in this way gas/electron beam interaction is minimized. The cell, in which gas can be introduced, is called the E-cell (Environmental cell). Note that this section is based on a manual provided by the microscope manufacturer ([49]).

A sample suited for TEM is thin. As the name suggests, images are formed by the transmitted beam of electrons, and only the projection of the sample of interest is examined in the TEM. Since electrons interact strongly with matter, TEM is mostly useful for samples less than 100 nm thick ([45]). This is important for the construction

of the ATOMICAR-design. The thinner the bottoms of the cavities are, the lower the signal they create, the easier it will be to image nanoparticles in the cavities. Furthermore, the total cavity depth should not exceed a few microns, otherwise the total projected gas density will reach a magnitude, which prevents atomic resolution ([41]).

The quality of an image depends on the signal to noise ratio. The higher the signal is above the noise floor, the easier it is to distinguish features in an image. Therefore, the areal electron dose rate on the sample is a very important parameter in the TEM, as it determines how fast a high quality image of the specimen can be obtained. However, the highly energetic beam electrons inflict damage on the sample illuminated and can even induce phenomena obscuring experiments conducted with a TEM ([50]). On the other hand, sample drift can be problematic, if long exposure times of the electron detectors are needed to obtain high quality data. These two effects have to be balanced such that the integrity of the sample is sustained, while the image acquisition time is minimized. In a TEM, the areal electron dose rate is controlled through the total dose of the beam reaching the sample and the area of illumination.

The total current of electrons illuminating the specimen is manipulated by changing the magnification of the electron beam on a diaphragm with a hole, called the C2 aperture. Electrons that do not pass through the aperture are excluded from the beam, as the diaphragm is too thick to allow electrons to be transmitted. The magnification of the beam on the C2 aperture is determined by the parameters "Gun lens" and "Spot size", which correspond to focusing powers of lenses in the first part of the condenser system (measured in arbitrary units from 1 to 8 and 11, respectively). The higher the "Gun lens" and "Spot size", the lower the beam current. Different C2 aperture sizes can be used to further change the total beam current.

The lenses below the C2 aperture control the width of the, ideally, circular beam on the sample. In the TEM used for this thesis, two lenses (C2 and C3) above the sample act in unison and their combined strengths determine the area on the sample illuminated by the electron beam. The image plane of these two combined lenses is aligned with the front focal plane of the objective lens, immediately above the sample. As the object distance from the objective lens then becomes infinitely large, see equation 2.4, the beam illuminates the sample with an almost parallel beam. This is important, when the contrast in the final image is to be interpreted.

The objective lens is a so-called "twin lens" - a split lens, in the middle of which the sample is inserted. Besides being involved in the illumination of the sample, the objective lens also focuses the electron beam transmitted through the sample. By definition, focus is achieved, when all electrons originating from a specific point in the object plane are collected in a point in the image plane, as described in the previous section. If the objective lens could collect all electrons from the object plane, no contrast would be visible in the final image. This is due to the fact that contrast is created by differences in interaction between electron beam and sample. As a consequence, an objective aperture is used to define and enhance contrast in the final image. This aperture is inserted in the back-focal plane of the objective lens to

exclude electrons scattered to specific angles.

As described in the previous section, electrons emerging from the object plane of a lens with a specific angle to the optical axis are focused to the same point in the back-focal plane. Therefore, an aperture positioned in the back-focal plane of the objective lens effectively determines the scattering angles allowed for electrons contributing to the final image. The thickness, mass, and crystallinity of a sample determine the degree to which it scatters the electron beam. In this way, the objective aperture can be used to create images of the sample thickness/mass or crystallinity.

Electron scattering is traditionally divided into two categories: elastic and inelastic scattering. A scattering event is considered elastic, if beam electrons lose negligible amounts of energy in the interaction with the sample. If the energy loss involved in the scattering event is considerable, the scattering is inelastic. Although elastically scattered electrons make up most of the transmitted beam (for thin samples), the inelastically scattered electrons are very important for this thesis' work, and will be described in more detail in Section 2.1.1.1. However, since the elastically scattered and unscattered electrons makes up most of the transmitted beam, images are often mainly formed with these electrons. The two most important types of elastic scattering are Bragg scattering and Rutherford scattering ([45]). Periodically appearing crystal planes deflect electrons by characteristic angles described by Bragg's law:

$$n\lambda = 2d\sin\theta_b, \quad (2.6)$$

where n is an integer, λ is the wavelength of the electrons, d is the distance between the crystal planes, and θ_b is the characteristic Bragg angle. Whereas, Bragg scattering scatters to specific angles, Rutherford scattering scatters electrons to a continuum of angles. The probability for Rutherford scattering is proportional to the atomic number of the atoms (with a range of exponents): $\propto Z^{1-2}$. Logically, the more atoms that the beam electrons have to pass, the more likely it is that the electrons interact with the atoms of the sample. Thickness contrast and mass contrast are therefore indistinguishably in images obtained with elastically scattered electrons. As a result, the term "mass-thickness" contrast is used.

Regions of greater mass or thickness, scatter electrons more, and by excluding electrons, which are deflected above a specific angle, these heavier/thicker regions will appear darker in the final image. Diffraction contrast is obtained in a similar way. Crystalline specimens deflect electrons to characteristic angles, and if electrons with these scattering angles are excluded from the final image, crystalline areas will appear darker in the final image. The parallel illumination of the sample provides a constant background to the deflection-related contrast, making contrast interpretation easier.

Contrast can be created in a third way. Exploiting the particle/wave-duality of electrons, so-called phase contrast can be achieved. Electrons scattered by different crystal facets will emerge from the sample with different angles and arrive in the final image after travelling slightly different distances - with different phase shifts.

If these waves of electrons are allowed to interfere in the image plane, interference patterns will appear with periodic structures reflecting the distance between the crystal facets ([45]). In this way, the area of a specific crystallinity can be identified. Phase-contrast is used to image nanoparticles, as it reveals projected crystal structure. Images presented in this thesis do not contain noteworthy crystalline or high resolution phase contrast. This is a consequence of the focus of this thesis, which is on the ATOMICAR-design rather than the use of it to image single nanoparticles. However, during the project, these types of image formation have been used extensively, and they are also described in this section to convey the capabilities of a TEM.

Another way to create large contrast in an image is to move the sample out of focus. By moving the sample out of the object plane of the objective lens, or by changing the objective plane position via a change in the lens strength, the image will be misaligned with the next part of the TEM, the projector system. This final part of the TEM magnifies the image from the objective lens and projects it to electron detectors mounted at the bottom of the TEM (in imaging mode). Lenses in this part of the TEM simply just work in unison to create different total magnifications. When the image is out of focus, the contrast is delocalized compared to its origin making it difficult to interpret. Furthermore, different interference phenomena can create new structures ([45]). However, the new and delocalized contrast can be seen at lower magnifications, and in combination with highly magnified focused images, defocused images can give useful overviews of the sample. In order to find and locate single nanoparticles on much larger electron transparent cavity bottoms, defocused images are used in the work presented in this thesis.

Besides image mode (described above), the TEM has another operating mode, diffraction mode. In diffraction mode, the back-focal plane of the objective lens is the object plane of the projector system. The final image, in this imaging mode, is not a real space image of the illuminated part of the sample, but an image of the scattering angles that the illuminating beam has suffered upon interaction with the sample. Such an image is highly useful, as characteristic crystal scattering can be identified, but it also contains area-averaged information for Electron Energy Loss Spectroscopy (EELS), introduced in the following section.

Electron detectors are used to collect and form digital images based on the transmitted electron beam. These detectors mounted at the bottom of the microscope column convert electrons impinging on their surface to currents that can be digitized. The images presented in this thesis are acquired with a Gatan US1000 CCD camera.

2.1.1.1 Electron Energy Loss Spectroscopy in the TEM

In EELS, the energy losses of the transmitted beam electrons are measured. Sample thickness and atomic composition determine the frequency of the specific energy losses, and therefore important sample characteristics can be derived from EELS. In this thesis, EELS is used to track the partial pressure of gasses captured inside sealed cavities and to assess the thickness of the electron transparent cavity bottoms.

The probability of inelastic scattering with a specific resulting energy loss can be described with a scattering cross section, $\sigma(E)$, which is the probability of scattering with the consequent energy loss E per projected areal density of atoms in the sample. Depending on the atomic species present in the sample, $\sigma(E)$ shows distinct features, from which both information about atomic bonding and composition can be determined. The magnitude of the total scattering cross section also contains valuable information. Since beam electrons have kinetic energies much larger than the energy losses associated with common inelastic scattering events and because angular deflections are small, successive scattering events are often assumed to be independent. Based on this assumption, Poisson statistics can be used to describe the probability that a beam electron does not scatter inelastically while passing through the sample:

$$I_0 = I_{total} e^{-\frac{t}{\lambda}}, \quad (2.7)$$

where t is the sample thickness, and λ is the mean distance travelled by beam electrons between scattering events, the mean free path ($\lambda = 1/\sigma\rho$, ρ being the density of atoms). Via this equation, a measurement of the total electron beam current and the amount of unscattered or elastically scattered electrons is an indirect measure of the sample thickness in terms of the mean free path. This and the fact that the mean free path easily can be found from reference measurements or theoretical models, make EELS a very strong tool for characterization of thin samples.

Electrons bound in the sample can be regarded as either valence- or core-electrons. Simply put, atomic bonding is a result of the sharing of electrons between adjacent atoms. These shared electrons, called valence-electrons, are not tightly bound to the specific atoms, and therefore they can be excited to do collective oscillations, called plasmons ([51]). In fact, energy losses associated with plasmon excitation are the most common, and $\sigma(E)$ peaks at a characteristic energy called the "plasmon energy". This energy is dependent on the density of valence electrons, and therefore it is not unique for specific samples. In the work related to this thesis, the plasmon losses are not analyzed directly, and therefore this type of energy loss will not be described further here.

The term "core-electrons" is used to describe electrons tightly bound to specific atoms. This type of electrons has binding energies specific to the atom that they are bound to. As quantum mechanics taught us, bound electrons only exist in quantized energy states, and transitions between different bound states can only happen, if the electrons receive energy quanta as large as the difference in energy between the states. A result of this fact is that EELS measurements will contain distinct features, if e.g. oxygen is present in the sample. In this way, the composition of the sample can be investigated by the use of EELS.

The scattering cross section for exciting the strongest bound oxygen (K-shell) electron has an onset at 532 eV ([52]), below which no excitation can happen. This is due to the fact that there are no available empty states accessible for the K-shell

electron with lower energies (relative to the K-shell energy). Above the onset of core loss scattering, the scattering cross section takes on a shape depending on the bonding configuration of the atomic species scattered upon. The first unoccupied states that the core electron can be excited to are its valence states, which have energies depending on the atomic bonding configurations. Consequently, the initial part of the loss spectrum from core-losses can then be used to identify chemical configurations. The higher the energy the core electron is excited to, the closer it gets to become an unbound electron. Most core-loss excitations have an approximate saw-tooth like shape. A sharp onset and then a decreasing intensity ([51]).

If electrons are only scattered once by the sample, the cross sections for different types of scattering phenomena are just added. The amount of electrons scattered by e.g. a K-shell electron to an energy loss E is independent of other scattering events resulting in the same energy loss. In this case, such other scattering events can be considered to act as a background signal for the signal of interest, and this background can be fitted and removed. Far away from the onset of an energy loss onset, the scattering cross section can be approximate with a power function ([51]). This is evident in different figures shown in Section 3.4. The background removed EELS data, is proportional to the number of atoms illuminated by the beam. The intensity of electrons measured to have scattered on e.g. an oxygen innermost core-electron can be described as follows ([51]):

$$I(E, \beta) \approx I_0(\beta) \sigma_O(E, \beta) N_O, \quad (2.8)$$

where $I(E)$ is the measured intensity of electrons with energy loss E , I_0 is the intensity of the beam not inelastically scattered, N_O is the projected areal density of oxygen atoms, and $\sigma_O(E, \beta)$ is the scattering cross section for scattering with energy loss E up to a scattering angle β . The equation above is based on the assumption that electrons only scatter once. If plural scattering is considerable, there might be several ways to exit the sample with the energy loss E . To solve this problem, it is often assumed that double scattering only happens when electrons first scatter on plasmons and then scatter on core-electrons ([51]). Since the most probable inelastic scattering is plasmon excitation, it is for thin samples a good approximation. In reality, however, the spectrum obtained with EELS is a sum of single, double, and higher order scattering events broadened by the finite energy resolution of the GIF. To fully treat all possible scattering event combinations with the resulting energy loss E , the full electron energy loss spectrum is needed up to E . In this thesis, only double scattering involving plasmon scattering is considered.

Just as for elastic scattering, inelastic scattering also changes the angle of the beam electrons path to the optical axis. The angular distribution of inelastic scattering can be approximated to be ([51]):

$$\frac{\delta^2 \sigma}{\delta E \delta \Omega} \approx \frac{4\gamma^2 R}{E k_0^2} \left(\frac{1}{\theta^2 + \theta_E^2} \right) \frac{\delta f}{\delta E}. \quad (2.9)$$

In this equation, R is the Rydberg energy (13.6 eV), γ is the relativistic correction factor, k_0 is the momentum of the beam electron before scattering, E is the energy loss, $\delta f/\delta E$ is the dipole oscillator strength, θ is the scattering angle and $\theta_E = E/\gamma m_0 v^2$. This approximation is valid for small deflections of the electron beam, a condition, which is often satisfied. In the TEM used for this work, EELS measurements are integrated over all scattering angles up to a collection angle. Depending on the operation of the TEM, this maximal allowed angle is either determined with the objective aperture or with the entrance aperture of the spectrometer used for collecting EELS signal. Depending on the energy losses of interest, the optimal maximal allowed scattering angle might differ. The probability of scattering above a few times θ_E is low, and consequently allowing electrons with larger deflection angles just increases the background signal in the energy loss region of interest.

To conduct EELS, a system for dispersing the transmitted beam electrons according to their energy is needed. In this work, a so-called Gatan Image Filter (post-column GATAN Image Filter (GIF) Tridiem 863) has been used. This equipment bends the electron paths according to the energy of the electrons and focuses them on an electron detector. In this way, a one dimensional image of the number of electrons having suffered specific energy losses can be collected. Due to the limited size of the electron detector, and the need for a sufficient energy dispersion to distinguish features, different parts of the energy loss spectrum have to be investigated one at a time. Spectra containing low energy losses from interaction between valence electrons and beam electrons are referred to as "Low-loss"-spectra, and the term "core-loss"-spectra is used for spectra containing higher energy losses from inelastic scattering between beam electrons and core-electrons.

In Figure 2.2, the GIF used for the work of this thesis is sketched ([53]). When entering the GIF, the beam electrons are first focused and aligned, before they arrive at the drift tube. It can be argued that the most important part of a GIF is the drift tube, as it disperses the electrons according to their energy. The bend drift tube sustains a magnetic field always perpendicular to the center of symmetry of the tube, and this bends the electrons through a radius of curvature (R) that can be described as follows ([51]):

$$R = \frac{\gamma m_0}{eB} v, \quad (2.10)$$

where m_0 is the electron rest mass, e the charge, B the magnetic field strength, v is the electron speed, and the relativistic factor γ corrects for the final speed of light ($\gamma = 1/(1 - v^2/c^2)^{0.5}$). The beam electrons, which have suffered energy losses, have

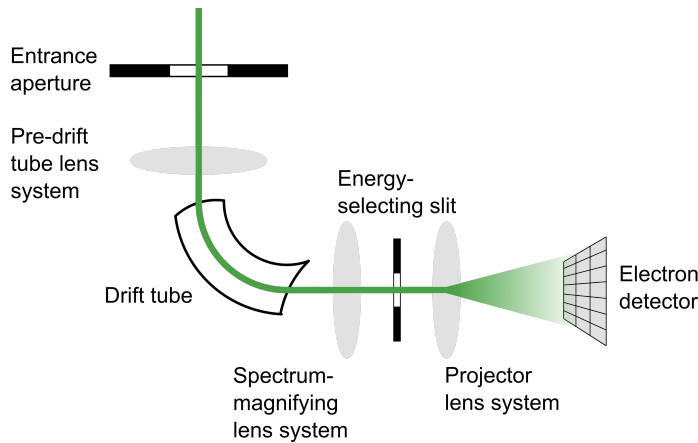


Figure 2.2. Sketch of GIF used to separate transmitted beam electrons according to their energy loss. A set of lens systems are used to map the electron beam from entrance aperture to electron detector. During this mapping, a so-called drift tube is used to disperse electrons as a function of their energy in the plane of the energy selecting slit. The GIF can either be used to acquire EELS data or to form energy filtered images.

lower kinetic energy and are therefore bend more by the drift tube. In this way, the electrons are dispersed at the end of the drift tube according to their energy loss. At the end of the drift tube, a slit can be inserted to exclude electrons with energy losses outside an energy interval. To make this selection precise, the entrance and exit faces of the drift tube are angled with respect to the symmetry axis of the drift tube. This geometry ensures spatial focusing of the image formed by the electrons entering the GIF. However, the focusing ability of the drift tube is not perfect, and curved drift tube faces and lenses compensate for that.

The energy-selecting slit has a specific physical width. To change the energy interval allowed to pass through the slit, a lens system is positioned after the drift tube and used to control the magnification of the electron beam on the slit. The following lenses project the energy selected pattern onto the electron detector at the end of the GIF structure. If the energy selective slit is retracted, a greater part of the energy loss spectrum passes to the electron detector and EELS spectra can be recorded. This operation mode of the GIF is called "spectroscopy mode". The projector system can also be used to form an image equivalent to the one entering the GIF aperture. In this mode, referred to as "imaging mode", an inserted energy selecting slit determines the energies of the electron beam, which are allowed to pass to the electron detector. Thereby, images of the sample can be formed of electrons scattered on e.g. oxygen. This technique is called Energy Filtered TEM, and is the subject of the following section.

2.1.1.2 Energy Filtered TEM

Whereas EELS data gives image averaged data, Energy Filtered TEM (EFTEM) provides spatially resolved electron energy loss data. Every operation that can be performed on EELS spectra, can be carried out spatially resolved with EFTEM. In order to do so, a stack of images is acquired with EFTEM while allowing different energy intervals to pass the energy selecting slit. The stack of images can be combined, and thereby EELS spectra are in effect collected for each pixel in the EFTEM image. The energy resolution is determined by the width, in terms of energy, of the energy-selective slit. EFTEM, however, comes at the expense of a greatly reduced current of electrons reaching the electron detector at the end of the GIF. The probability for inelastic scattering is quite low and decreasing towards higher energy losses. As a result of that, spatially resolved images of the e.g. density variations of oxygen in the sample will suffer from very low electron counts in the pixels. In principle, this can be compensated for by adjusting the exposure time of the electron detector and the areal dose rate, but sample drift or damage might compromise the images.

EFTEM was used in this PhD study to measure local variations in thickness of the electron transparent bottoms in the ATOMICAR-design. As only the low-loss part of the EELS spectrum is needed for this type of EFTEM, electron counts are sufficient to obtain good images. The thickness of the electron transparent bottoms of the ATOMICAR-design is very important. In order to obtain high resolution images of nanoparticles caught in cavities of the ATOMICAR-design, the bottoms must be thin.

To obtain t/λ image, two images are acquired for each imaged area. One is collected with an energy-selecting slit filtering everything but elastically scattered electrons from the image, and one without the slit. The unfiltered image contains counts of electrons of all energy losses at each pixel, whereas the filtered image is only composed of the elastically scattered electrons. By taking the logarithm of the ratio of the two image a t/λ map can be obtained. Knowledge of the mean free path, λ , can then be used to convert such a map into a thickness map.

2.1.2 Scanning Electron Microscopy

Contrary to a TEM, a SEM probes the surface of a sample. However, from electron gun to objective lens, a SEM and a TEM are very much alike technologically. In the SEM used for this PhD study, a FEG serves as the electron source, and a condenser lens system is used to control the total current. Finally, an objective lens is used to focus the beam electrons to a spot on the sample surface ([54]). The acceleration voltage in the SEM is low compared to in a TEM (200 V to 30 kV ([54])), because lower acceleration voltages result in a greater probability of interaction between electron beam and sample ([47]). This is advantageous, as it results in shorter mean free paths and in the end, smaller total penetration depth of the beam electrons, and thereby relatively more signal is created close to the surface. A SEM of the type "Quanta FEG 200 ESEM" from FEI was used to acquire images for this thesis.

The design of a SEM is outlined in Figure 2.3. The purpose of the electron optics in a SEM is to demagnify the image of the electron gun as much as possible ([55]). This is partly done by the condenser system and partly by the objective lens, which focuses the demagnified image of the FEG on the sample. Apertures in front of both objective lens and the condenser lenses are used to limit large angular deflection from the optical axis, and as a result, the total current of electrons in the beam is not conserved for all spot sizes; the smaller the spot of electrons on the sample is, the lower the total current. In the SEM used for this PhD study, the spot size can be changed in discrete steps measured from 1 to 7 in arbitrary units ([54]). Different aperture sizes can also be used to further change the beam current and size. Again, smaller sizes result in better resolution but less total beam current.

The electron beam is scanned in a raster pattern across the sample, and the signal created at each position is collected independently ([54]). The time during which the beam is parked at the same position is called the "dwell time". An image of the sample is created, by assigning each beam position to a pixel in a digital image. The magnification of the image is then determined by how close the pixels and thereby beam positions are.

The final parameter to choose, when operating a SEM is the working distance. This is the geometric distance between objective lens and sample surface. Long working distances result in a probe shape that is small over greater distances and thereby more of the sample can be in focus at once. The downside of long working distances is that it deteriorates the resolution, i.e. the minimal probe size is larger ([55]).

The beam electrons gradually lose their energy to the sample, as they pass through it, and the volume, in which this energy exchange takes place, is called the "interaction volume" ([47]). This volume is illustrated on the sample in Figure 2.3 with a black line. As indicated in the figure, the volume is much larger than the size of the beam spot. Consequently, a lot of signal is generated by the electron beam at different depths of the sample, and the SEM operator must take this into consideration, when analyzing images. Upon interaction with the sample, the electron beam spot creates a number of so-called secondary and backscattered electrons ([55]). Secondary electrons are created all over the interaction volume, but the low energy electrons can only escape the sample close to the surface. At the edges, a greater part of the interaction volume is close to the surface of the sample, and as a result more electrons are emitted from the sample, when the beam is parked at edges. The low energy electrons are collected with an Everhart-Thornley (ET) detector ([54]), which attracts the low energy electrons with a positively charged cage in front of its electron detector. The ET detector is positioned at an angle to the surface normal of the sample, and as a result of that parts of the sample are not in the line of sight of the detector. The combined effect of the "edge effect" and the position of the ET detector creates a 3D illusion, making secondary electrons signal perfect for gaining topographical information about the sample.

The probability of backscattering of beam electrons during interaction with a sample atom depends on the atomic weight of the sample - the heavier the atoms,

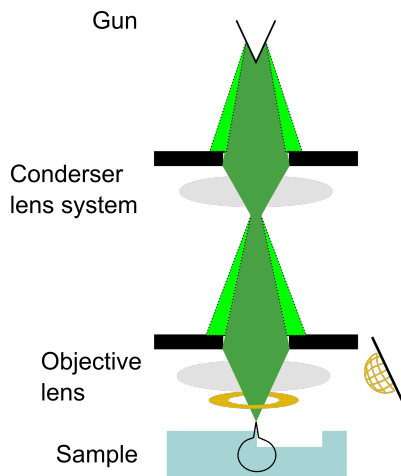


Figure 2.3. A sketch of a SEM. An electron gun delivers a steady stream of electrons, which is then focused by the condenser system to a small spot. This spot is then focused on the sample by the objective lens. The beam electrons deposit energy in a large volume of the sample, indicated with a black line. This energy exchange creates free low energy electrons, which are collected by an Everhart-Thornley (ET) detector drawn to the right of the sample. Some of the beam electrons are backscattered and these type of electrons are collected with an electron detector positioned at the exit of the objective lens. Both detectors are colored yellow.

the more likely scattering is ([55]). As a result, the relative intensity of backscattered electrons between different beam positions indicates differences in atomic composition. Since the backscattered electrons are reflected towards the incoming beam, an electron detector is positioned at the exit of the objective lens to detect this type of signal. The energy of backscattered electrons is high, and as a result, they can escape from greater depths of the sample, and therefore both lateral and horizontal resolution are worse in images generated with a backscattered electron signal as compared to those made using secondary electrons. The electron beam also creates other signals e.g. X-rays, but only secondary electrons have been used to form images for this thesis. Images presented in this thesis were exclusively acquired with an ET detector.

2.2 Atomic Force Microscopy

When an oscillator is driven close to resonance, the amplitude of its motion is sensitive to external forces. This is the working principle of Amplitude Modulated Atomic Force Microscopy (AM-AFM) ([56]). With AM-AFM, the surface topology of a sample can be measured with a resolution below one nanometer. Such measurements have been crucial to the design of the ATOMICAR-devices, as most features of the design

are about a few microns or even smaller. However, for the samples presented in this thesis, AFM measurements are not straightforward to perform, if the measurements are to be scientifically trustworthy. This section seeks to describe theory, which can be used to evaluate the quality of the AM-AFM measurements presented in Chapter 3.

Using AM-AFM, relative height maps of the sample can be obtained in the following way: A cantilever with a sharp tip at the end is oscillated close to its resonance by a piezo element at its bottom. The piezo movement can be described by its amplitude of motion, A_{piezo} , and its frequency, ω : $z_{piezo} = A_{piezo}\cos(\omega t)$. This gives rise to a cantilever motion about its equilibrium distance to the sample, which in steady state can be described as $z_{cant} = A_{cant}\cos(\omega t + \phi)$, where ϕ is a phase shift between the motion of the cantilever tip and the piezo element. As the sharp tip is brought close to a sample, the trajectory of the tip enters the potential of the surface. The interaction between sample and tip delays the movement of the cantilever head relative to the oscillation of the piezo element, and the phase shift deviates from the case of maximal energy transfer from piezo element to cantilever ([56]).

It can be experimentally proven that the cantilever motion stays sinusoidal while the tip enters the surface potential ([57]). From this observation, the relation between cantilever oscillation amplitude and phase shift can be derived from simple energy considerations to be (at resonance [57]):

$$\sin(-\phi) = \frac{A}{A_{free}} \left(\frac{\langle E_{ts} \rangle}{\langle E_{cant} \rangle} + 1 \right), \quad (2.11)$$

where $\langle E_{ts} \rangle$ and $\langle E_{cant} \rangle$ are the energy dissipated per oscillation to the sample and the energy dissipated in the medium, in which the cantilever oscillates (air or liquid). In equation 2.11, $A_{free} = Q_{cant}A_{piezo}$, where Q_{cant} is the quality factor of the cantilever ([56]). The amplitude of the cantilever tip motion is reduced, compared to the oscillation without sample interaction, if either the phase shift between piezo element and cantilever tip movement differs from $-\pi/2$, or if energy is dissipated to the sample. Assuming only conservative tip-sample interaction, one can derive the following expression from the equation of motion of the cantilever, when it is driven at resonance ([56]):

$$\cos(\phi) = \frac{-2Q}{kAA_{free}} \langle F_{ts} \cdot z \rangle \quad A = A_{free}\sin(-\phi). \quad (2.12)$$

Here $\langle F_{ts} \cdot z \rangle$ is the force between tip and sample multiplied by the cantilever oscillation around its equilibrium position averaged over one period of oscillation, and k is the spring constant of the cantilever. In the derivation of equation 2.12, z is negative below the equilibrium position of the cantilever. It can be concluded from equation

2.12 that an average positive tip-sample interaction will result in a phase shift below $-\pi/2$, and an average repulsive interaction will give a phase shift above $-\pi/2$. Via the phase shift, tip-sample interaction reduces the oscillation amplitude of the cantilever, as does dissipation of energy to the sample ([56]).

In AM-AFM, the amplitude of the cantilever motion is monitored by measuring the reflection of a laser on the cantilever head with a photodetector, and a feedback system keeps the amplitude constant by either retracting or approaching the base of the cantilever from/to the sample surface. This is sketched in Figure 2.4. When the amplitude is held constant with the feedback system, and there is no change in energy dissipation to sample, the tip-sample force must be constant. Under the assumption that the average tip-sample force is constant across the sample, a map of the retraction and approach of the cantilever base by the feedback loop can be interpreted as a height map of the sample surface. Images obtained with AFM are composed of line scans, and the AFM operator uses the forward and backward scan of the same lines to optimize imaging parameters and obtain reproducible line scans.

A FlexAFM from Nanosurf and a Dimension Icon from Bruker (situated in the cleanroom) were used to conduct the measurements presented in this thesis, and in this equipment, the feedback system is a so-called PID system controlled by the user ([58]). Cantilever oscillation amplitude, piezo driving amplitude and driving frequency are interdependent parameters, and they can be set by the user or suggested by the software. The cantilever is approached the sample until the oscillation amplitude is reduced to a set-point amplitude, and then the cantilever head is scanned across the sample, while the feedback system ensures a constant oscillation amplitude of the cantilever. The response of the feedback system to a change in cantilever oscillation amplitude is determined by three parameters P-, I-, and D-gain (all measured in arbitrary units). Both the movement of the cantilever base and the oscillation of it are measured in V, and the difference between the set point and actual amplitude can be used as the signal controlling the movement of the cantilever base. The voltage fed into the piezo, controlling the distance between sample and cantilever base, is determined from the sum of the error signal, integral error signal, and differential error signal, scaled by the P-, I-, and D-gain (only P- and I-gain for Dimension Icon). The best choice of parameters depends on sample topography, scanning speed, oscillation amplitude and set point amplitude. As a rule of thumb, the selected parameters, should reproduce the same image of the sample surface, and reference structures should be accurately represented, i.e. flat areas should be imaged as flat. Other microscopy techniques can be used for reference.

The equations stated so far do not describe whether a specific oscillatory cantilever motion exists or not. Even though the phase, and thereby also the cantilever oscillation amplitude, can be imagined to change continuously, as $\langle F_{ts} \cdot z \rangle$ is continuously changed during sample approach, this is in fact not what happens. In general, z exhibit a jump in amplitude during approach, as one type of stable oscillatory motion vanishes, and the cantilever settles in a motion with a higher oscillation amplitude. This behavior is heavily dependent on the driving frequency. The ratio A/A_{free} is maximized at ω_0 without tip-sample interaction, and importantly only one

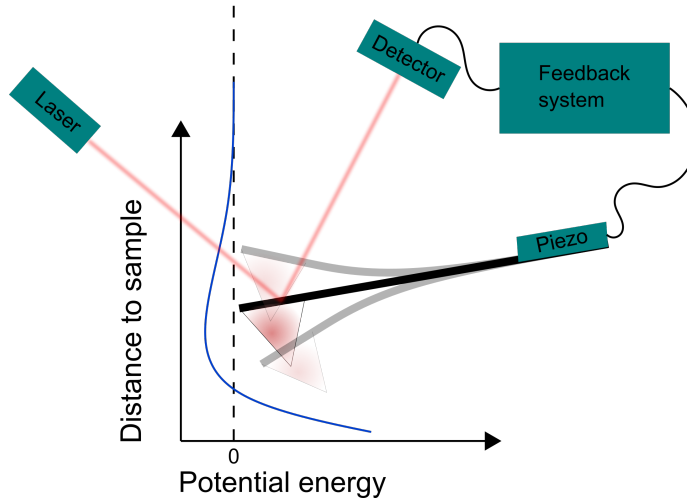


Figure 2.4. AFM working principle: A cantilever with a sharp tip at the end is oscillated in the sample surface potential. The oscillation is tracked with a laser and a photodetector, and a feedback system controls the cantilever motion and average distance to sample with a piezo element. A change in average distance to the sample results in different oscillation amplitude, as the average sample-tip force is changed. This fact can be used to construct topological images of the sample surface, when the average distance to the sample is held constant by the feedback system.

oscillatory motion is stable for each driving frequency. As the sample is approached, several A/A_{free} can become stable at the same driving frequency, and unstable scanning can result in a “jump” from one type of oscillation to the other. Furthermore, one type of oscillation can become unstable, and the tip motion will “jump” to a stable motion. Fortunately, this type of “jump” between modes will be accompanied by a sudden change in phase shift ([56]). It is important to ensure stable phase shifts, otherwise the image acquired with the AFM will appear to have unphysical steps in height. This can be ensured by using an appropriate equilibrium distance to the sample or by operating at a driving frequency, at which only one type of oscillation can be sustained ([59]).

In summary, AM-AFM image acquisition is optimal, when the oscillation amplitude is kept constant by the gains while scanning. Furthermore, the phase signal should not show sudden jumps. In the present PhD study, only AM-AFM was used and thus, the terms “AFM” and “AM-AFM” are used interchangeably.

2.3 Cleanroom fabrication techniques

All samples examined in this thesis have been fabricated using cleanroom facilities at DTU Nanolab - National Centre for Nano Fabrication and Characterization ([60]). A cleanroom is a dust free environment ([61]). The cleanliness of a cleanroom is ensured by air filters, which remove particles from the air, and by keeping strict rules about the cleanliness of samples allowed in the cleanroom. Furthermore, cleanroom users are to wear cleanroom suits that minimize the release of particles from clothes to the cleanroom environment. The dust free environment is a necessity when the ATOMICAR-devices are to be fabricated. This section introduces the utilized cleanroom fabrication techniques conceptually, without elaborating on technical details. The actual operation of the cleanroom machinery used is controlled by "recipes" (long lists of instructions to the software controlling the used equipment) developed by equipment manufacturers and cleanroom employees. Since, it has not been necessary to deviate from these "recipes", it is outside the scope of this thesis to discuss the recipes in all their intricacies.

Micro-fabrication is the basis of modern society. Integrated circuits and minuscule sensors form indispensable parts of modern electronic devices, and these tiny devices are produced with micro-fabrication technologies ([61]). As the term suggests, micro-fabrication denotes the procedure of realizing micron-sized features. Methods specifically developed for micro-fabrication are needed, if structures at these small length scales are to be produced. Due to the complexity of the task, there exists many different strategies and methods, but only those relevant to the present ATOMICAR-design will be discussed in this section. The techniques employed to fabricate the ATOMICAR-devices can be divided into three categories: 1) Thin film growth or deposition, 2) Mask definition, and 3) Etch. In the following, these three steps will be sketched.

Micro-fabricated samples are often produced on single-crystalline silicon wafers, and this is also the case for the ATOMICAR-device. Structures can be defined on the surface of the wafer by combining thin film deposition and growth with wet and dry etches through a mask. In the production of the ATOMICAR-devices, thin layers have been deposited using two methods; Low Pressure Chemical Vapor Deposition (LPCVD) and Plasma Enhanced Chemical Vapor Deposition (PECVD). LPCVD is a batch process in which several wafers are exposed to reactant molecules at high temperatures and low pressures in a furnace. In Figure 2.5, LPCVD is schematically illustrated for a wafer carrier, called a "boat", with wafers situated in a furnace. SiO_2 and Si are deposited on the samples described in this thesis, but SiO_2 is also grown. This is achieved by exposing a "boat" with wafers to water vapor at ambient pressures inside a furnace, similar in design to those used for LPCVD. All furnaces used for LPCVD or oxidation of silicon are horizontal furnaces from Tempress.

PECVD is an alternative to LPCVD. Using a plasma, reactant molecules are dissociated and excited, and as a result, less thermal energy is needed to aid the reaction of deposition [61]. This is advantageous, if the sample will be damaged by

heating or if high deposition rates are needed. The setup (STS Mesc Multiplex CVD) used to carry out PECVD is very similar to that used for dry-etching and is therefore not separately treated. Figure 2.6 sketches a plasma chamber of the type used for this project. The plasma composition determines whether reactants are deposited, or if the reactants etches the sample. Coils are used to create and sustain a plasma, and a set of biased plates are used to direct ionized molecules towards the sample.

A very important step in a cleanroom process flow is mask definition. Masks protect certain areas of the sample while others are left exposed, and therefore patterns can be transferred from mask to sample with an etch. Photo-lithography ([61][62]) allows for the definition of masks with feature sizes about a micron, and it is the only lithography method used in the work related to this thesis. Photo-lithography is carried out in the following way: The sample is coated with a thin layer of a polymer solution, called a resist (AZ 5214E. Wafers primed with HMDS). The resist is then baked in order to evaporate solvents and harden the resist. In this project, the resists used are positive photo-resists, meaning that the polymer structure of the resist is altered if illuminated with light at specific wavelengths. This altered polymer structure has a higher solubility in solvents compared to the unexposed resist. The resist can be developed with solvents such that the areas of the resist, which have been exposed to light, are removed, whereas unexposed areas are left unaltered. In this way, a structure can be defined in the resist and this structure serves as a mask for the subsequent etching steps. After etching, the mask can be removed either chemically or by cleaning in an oxygen plasma. As the design of the ATOMICAR-devices changed during the PhD-project, a laser-writer (Heidelberg Instruments MLA150 WM I Maskless Aligner, s/n HI 1054) is used to expose the resist. The machine exposes samples according to digital drawings of the areas to be exposed, and as a result, new patterns can be defined in resist, whenever a new drawing has been made. Alternatively, a hard mask can be made utilizing a non-transparent material. If the sample with resist is exposed through the mask, the pattern defined in the mask can be transferred to the resist.

When etching, the selectivity and etch rate are essential. By timing etch duration, the depth of etched structures can be controlled to some extent, but the etch rate might be non-uniform over the wafer. This is problematic, as samples fabricated in different areas of the wafer must be characterized individually. Furthermore, the etch rate might change a little from time to time making it difficult to define well-defined structures. A highly selective etch only etches one type of material, leaving the rest of the sample unaltered. A layer composed of a material different from the material targeted by the etchant can be used to limit the geometric extent of the etch, a so-called stop layer.

Etching is commonly divided into two categories: anisotropic and isotropic etching ([61][62]). The former is used to describe etching with a preferred direction and the latter describes the opposite case. Both types of etches can be needed depending on the desired geometry of micro-structures. Etches can be subdivided into "wet" and "dry" etches, i.e. etch with or without a solution.

Wet etches are often selective to some extent, but lack directionality. Conversely,

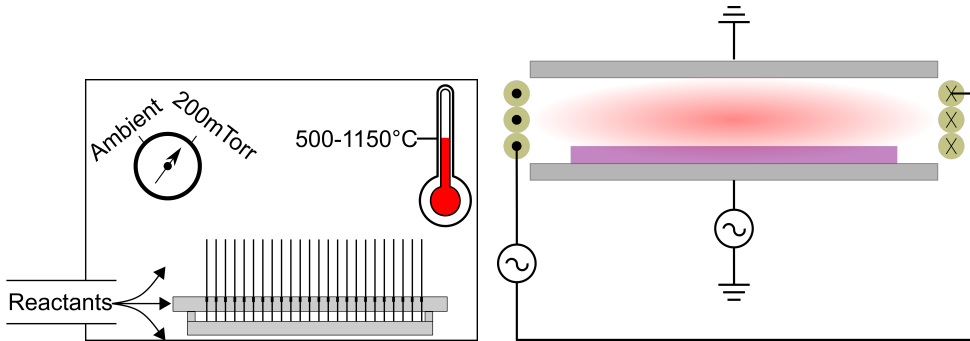


Figure 2.5. Thin film growth or deposition in a furnace. Wafers (long black lines) are held by a "boat" (gray cross sectional drawing), and positioned in the flow of reactant gasses. Depending on the process in question the pressure can be very low to 1 bar. To accelerate the deposition rate high temperatures are needed.

Figure 2.6. Plasma chamber for etching or deposition. Two circuits with alternating currents are used to create a plasma and direct it towards the sample. Wires, colored yellow in the drawing, form a coil around the chamber, and the sample wafer (purple) is positioned downstream of the plasma flow.

dry physical etches (sputtering with collimated ions) are highly anisotropic, but sputtering does not distinguish between materials rather bonding energies. Chemical dry etching with plasma combines these two methods ([61][62]). Using a plasma, reactants can be made more reactive, and the ions of the plasma can be used to control the direction of the etch. An illustration of a plasma chamber with this purpose is shown in Figure 2.6. This type of etches creates geometries with straight sidewalls, but the etch rate is too low for deep etches. In order to achieve deep etches of silicon, a so-called "Bosch etch" can be employed. This type of etch is divided into an isotropic etch step followed by a step in which the sample is passivated with a thin protective layer of polymer, which is removed by ion in regions in the line of sight of the plasma. Iterating these two steps creates deep trenches very fast. To etch silicon oxide and silicon, an Advanced Oxide Etcher (AOE) (STS MESC Multiplex ICP serial no. 32843) and an Advanced Deep Reactive Ion Etching (DRIE) Pegasus (Serial number MP0636) have been used. Both a "Bosch etch", dry etches of silicon and silicon oxide, and a isotropic dry silicon etch have been used to fabricate the present ATOMICAR-device.

Using thin film growth or deposition, masks and etches repeatedly, three dimensional structures can be created layer by layer. Since dust particles are comparable in size to the structures defined with microfabrication techniques, they can obscure pattern transfer from resist to wafer ([61]). In addition to this, dust particles can be embedded in between layers of thin films altering the sample topology or other thin film characteristics. This is the reason why microfabrication needs to be carried out in a cleanroom.

2.4 FLG transfer

FLG is nearly the optimal seal of a tool like the ATOMICAR-device. In Chapter 3, the capabilities of graphene, and its use for the ATOMICAR-design will be discussed. To prepare the reader for this, this section briefly sketches how FLG is transferred to a substrate. This author has not been directly involved in the procedures described below, however the transfer techniques are sketched to get a coherent thesis. After years, where many different sealing techniques have been explored by the postdocs Edwin Dollekamp and Zhongli Wang, we settled on using two techniques. The first technique is referred to as "mechanical exfoliation" and the second method is in this thesis called "CAB transfer".

Mechanical exfoliation ([63]) is in principle the most simple technique that can be employed to transfer FLG to a substrate. In the ATOMICAR-group, it is standard procedure that a sample is prepared for mechanical exfoliation by cleaning it with solvents (acetone and IPA or 2-propanol and DI water). Afterwards, the sample is placed for 8-10 minutes in an oxygen plasma chamber (Plasma Etch, PE-50) at about 140 W to further clean it. As quickly as possible after this step, a graphite crystal held between two pieces of Scotch tape is exfoliated by pulling the two pieces of tape apart, and one of the freshly cleaved graphite flakes is then pressed against the substrate. When the tape is removed from the substrate, most of the graphite is left on the tape, but a random number of flakes of random thickness are left on the substrate. In our experience, the transfer yield depends on the substrate and substrate preparation. Both a low substrate surface roughness and oxygen plasma cleaning are essential for a good transfer yield. Mechanical exfoliation is the preferred transfer technique in the group, as it is the experience that the lowest leak rates can be achieved with this technique. Furthermore, the substrate is not heated during sealing, and if the substrate is prepared well, it is unlikely that any contamination is caught in between the FLG and substrate. Although, the technique has a number of advantages, the random nature of it makes it very unlikely that specific cavities are sealed. While this is not important, when the density of cavities to be sealed is high, it is quite an issue, if a specific cavity has to be sealed, e.g. a cavity with a single nanoparticle. In addition to this, ATOMICAR-devices have to be able to withstand the pressure applied, when the cleaved graphite crystal is pressed against it.

The CAB transfer technique is based on ref. [64]. In this technique, a polymer stamp with FLG is used to transfer FLG to a substrate at a specific position. The first step of the procedure is to exfoliate graphite on a 90 nm thick SiO₂ layer on a silicon wafer. Using an optical microscope, a sheet of FLG can be identified. After detection of the FLG flake, 20 g/100 ml Cellulose Acetate Butyrate (CAB) in ethyl acetate is spin-coated on the sample (EMS 6000 Photoresist Spinner) at 1000 rpm for 1 min with an acceleration of 200 rpm. The CAB is then cured for 6 min at 60°C. Then, the FLG flake of interest is found again, and a $\approx 2 \times 2$ mm² square is scratched around the flake of interest. Placing a droplet of deionized water on top of this cut results in the intercalation of water in between the CAB and wafer, which makes it possible

to lift the CAB piece with a tweezer. The CAB piece is then placed on a Gel Pak® film (PF-X4-17mil), which is situated on a microscope slide. The microscope slide is then flipped and positioned on a micromanipulator - the FLG stamp is prepared. A substrate with cavities is placed on a heater with a sticky adhesive and aligned with the CAB piece with the FLG. The sample is then heated to 80 – 135°C, and the CAB with FLG is lowered and brought into contact with the sample. After everything has cooled down, the microscope slide is lifted. The CAB with FLG remains at the sample, and finally, the CAB is dissolved for 5 min in acetone. At the end of the procedure, only the FLG remains at the desired location on the substrate. This method is obviously useful, when FLG sheets are to be transferred to a specific location on a substrate. It has not yet been determined, whether reactants for the catalytic processes to be studied with the ATOMICAR-device are to be loaded during FLG transfer or afterwards. For the purpose of this thesis, it has been sufficient to track the leak of ambient air to prove that the internal pressure of sealed cavities can be tracked, but for future experiments, it might be a huge issue, if catalysis initiates during transfer of FLG at elevated temperatures. Interesting phenomena might not be discovered, if the catalytic process is not monitored, when it starts. Both methods described have obvious advantages and disadvantages, and it remains to be settled, which one can be used for studies of catalysis.

Numerous different methods ([65]) have been developed to transfer FLG to a substrate, although in the ATOMICAR group, the two methods described in this section are in general perceived to be the most relevant methods for the ATOMICAR-project.

CHAPTER 3

ATOMICAR-design

In Chapter 1, the need for a new tool with the ability to measure single particle catalysis *in situ* was discussed. This chapter will discuss and present one of many versions of the ATOMICAR-design, which was developed during the PhD project of this author. The design, presented in the following chapter, is the latest version, and alternative design strategies, which have been explored during the PhD project will be discussed where relevant. Firstly, it is discussed what characteristics an ATOMICAR-device must have, and then the approach to develop such a device is presented. Different design strategies can be imagined and different designs of such a tool will need to fulfill varying specifications. However, a device based on the ATOMICAR-concept must satisfy the following requirements, independent of the specific way the ATOMICAR-design is realized:

- The cavities of the reactor need to be sufficiently small for single particle catalysis to have a measurable impact on the pressure and gas composition of sealed cavities.
- The reactor should allow experiments to be conducted at high pressures and at several hundreds of degrees Celsius.
- The reactor should have negligible background activity.
- The membrane covering the cavities need to be highly flexible in order for small pressure changes to be detected.
- The bottoms of the cavities should be electron transparent, if active nanoparticles are to be characterized with sufficient resolution.

The higher, the pressure and temperature can be in experiments conducted with the reactor, the better. As a minimum, pressures above 1 bar and temperatures above 300 °C should be possible. In this case, the achievable temperatures would match those used in industry for e.g. methanol synthesis, and the maximal pressure would be comparable to those commonly used in *in situ* TEM studies of catalysts (e.g. [27][43][44]). Of course, an ideal ATOMICAR-design would facilitate activity measurements without any detection limit, i.e. even a single conversion of reactants to products would be measurable. However, this would require a cavity size comparable to the size of nanoparticles, and a very flexible membrane sealing off the cavities.

In a small volume, the catalyst only need to convert a small number of molecules, before an appreciable pressure change is achieved (if the catalysed reaction changes the number of molecules). The more flexible the membrane sealing the cavities is, the smaller a pressure change can be while still inducing a measurable membrane deflection.

In general, membranes tend to get less flexible, when their diameter is reduced ([66][67]), and this makes the optimal cavity size a compromise. Since, the membrane used to detect pressure changes in the ATOMICAR concept is suspended across the cavities, the optimal size of a cavity is not as small as nanoparticles. The intuitive solution to this problem is a very shallow cavity, maximising the area over which the membranes are suspended, while keeping the volume small. However, in structures like the one depicted in Figure 1.2, a shallow cavity is realized by making the free-standing slab thin. This is problematic, as the transfer of a sealing membrane to the slab might fracture it, as a thin slab is fragile. Furthermore, it is preferable that gasses captured in the cavities can be studied with EELS in a TEM, and this requires the cavity to have a certain depth. This point will be further elaborated in Section 3.4. Therefore, instead of choosing a cavity volume giving the highest sensitivity toward chemical conversion, the cavity dimensions should be selected such that relevant differences in catalytic activities create distinguishable internal cavity pressures. The requirements have to this point largely been discussed without stating exact numbers. Without knowledge about how critical each requirement is, it is difficult to do an optimization. To some extent, the design and choice of materials determine, how critical each parameter is, and therefore the design must be more specific, before it can be optimized. The most difficult task is to detect catalytic conversion of single nanoparticles, hence the first task is to choose an appropriate cavity size and sealing membrane. In order to estimate the approximate size of the cavities, common catalytic conversion rates should be considered.

A nanoparticle's activity is often measured in terms of its turnover frequency (TOF) - the speed at which products are catalyzed. The TOF depends on the catalyst, the chemical process, temperature and pressure, but for methanol synthesis, reported TOFs are approximately between 0.001/s and 0.1/s per exposed metal atom at conditions relevant to industry (supplementary information of ref. [68]). Assuming that methanol is synthesized directly from H_2 and CO_2 , and that the only by-product is H_2O , each catalytic conversion will consume two molecules ([69]). Assuming a constant TOF of 0.01/s and 10,000 exposed metal atoms (10 nm particle with 71.6% of the surface covered with metal atoms each with a surface area of $0.3 \times 0.3 \text{ nm}^2$), the total number of molecules consumed within 8 hours (a practical period of time) is $57.6 \cdot 10^5$. If it is then required that this number of molecules should correspond to a pressure change of 0.1 bar in a cavity at 500 K, the cavity volume can be calculated from the ideal gas law ([8]):

$$pV = nRT \rightarrow V = \frac{nRT}{p} \approx 4\mu\text{m}^3. \quad (3.1)$$

Here $P, V, n, R,$ and T is the pressure, volume, number of molecules, the gas constant, and the temperature, respectively. From this simple calculation, it can be concluded that if the cavity volume is $4\mu\text{m}^3$, and a pressure change of 0.1 bar can be detected, then mediocre catalytic activities can be distinguished from each other. As a starting point, it is reasonable to conclude that as long as the cavity volume is a few μm^3 , then it is sufficiently small. Catalytic processes with lower TOFs can be studied in this volume, if the nanoparticles studied are composed of more active atoms. The greater amount of catalytic active sites will compensate for the lower activity per site.

A volume this small is difficult to fabricate in a controlled manner without micro-fabrication techniques, especially when it is also required that the structure in which cavities are made should be able to withstand high pressures and temperatures. This second requirement rules out the use of materials like polymers. Mostly metal composites can withstand high temperatures and pressures. However, many metals are catalytically active. Few materials are considered as inert as silicon oxide and silicon nitride, and therefore it is natural to use these two materials as main constituents of the slab in the ATOMICAR-design. In conclusion, the ATOMICAR-structure should be constructed of silicon oxide, silicon nitride or a material with similar properties, and microfabrication should be used to define structures.

A negligible background activity is crucial, if the activity of single nanoparticles is to be distinguished from each other. There should not even be small amounts of reactive metals in the cavities besides the nanoparticles. In the DTU Nanolab cleanroom some of the equipment contains traces of metals, and this equipment is problematic to use in the fabrication of an ATOMICAR-device. Consequently, this equipment is avoided in the process flow of the present design.

The electron transparency of a material depends on the thickness of the material and density ([45]). The thinner and lighter the material is, the more transparent the material is. Several microfabricated devices for *in situ* studies of catalysis in TEMs (also mentioned in Chapter 1) have been developed. Often, the sample is observed through two windows in this type of devices; one at the top and one at the bottom of the reactor. Combined window thicknesses between 16 nm and 100 nm of SiNx or carbon have been shown to be sufficiently electron transparent for studies of nanoparticles ([70][40][41][71]). The electron transparent window thickness is a figure of merit for electron transparent reactors, and the cavity bottoms of the ATOMICAR design should not exceed 100 nm in thickness.

Until now, the seal of the cavities in the ATOMICAR-design has not been extensively discussed. However, the usefulness of a device based on the ATOMICAR-design, depends on whether the seal is sufficiently leak-tight. Furthermore, the seal should be very thin for two reasons: Firstly, the thinner the membrane is, the more flexible it is, and secondly, a thin seal will have less influence on the overall electron transparency of the cavities. Unfortunately, most material's permeability depends on their thickness according to Fick's law ([72]):

$$J = -D\nabla n. \quad (3.2)$$

In this equation, J is the particle flux, D is the diffusivity, and ∇n is the concentration gradient of particles. The flux of particles through a membrane separating the cavities from the surrounding environment will increase as the thickness of the membrane decreases. Only a material with $D = 0$ can be practically impermeable to gases and at the same time be thin enough to have negligible effect on the overall electron transparency of the reactor. It wasn't before 2008 a material with these properties was known. In the following section, the discovery of the impermeability of graphene is discussed, and it is described why graphene in theory could serve as the ideal sealing membrane in the ATOMICAR-design.

3.1 Graphene: An impermeable seal

In a pioneering study from 2008, Bunch et al. ([73]) reported that FLG is impermeable to all gasses, even helium. This conclusion was based on observations of the leak rate of molecules from cavities sealed with few layers of graphite. The studied cavities were square shaped with side lengths varying from 2.5 – 4.8 μm and depths between 250 nm and 3 μm . Dry etching was used to etch the cavities into oxidized silicon wafers with either 285 nm or 440 nm of oxide. Using Scotch tape, FLG was mechanically exfoliated on the cavity structures, and the cavities were then filled with a loading gas or emptied in a pressure chamber. The FLG-membranes suspended across sealed cavities bulged, if a pressure difference across them was established, and the strain in the membranes was monitored by optical measurements of the resonance frequency of the membranes at different ambient pressures. As the internal pressure of the cavities equilibrated with the ambient atmosphere, the gradual relaxation of the membranes was tracked. From these measurements, the leak rates of helium, argon and ambient air were calculated. Quite astonishingly, the leak rates were independent of the number of graphene layers sealing the cavities. Bunch et al. (2008) concluded that graphene practically is impermeable to gasses. The precision with which this could be concluded was limited by the finite leak rate of the sealed cavities, which varied between 300 and 10^6 atoms per second depending on the gas. Recently, graphene-sealed cavities etched in graphite crystals was investigated by Sun et al ([74]). This study verified the impermeability of graphene towards all gasses except hydrogen with a precision of a few molecules per hour. The discovery of the impermeability of graphene towards most gasses has sparked the development of a number of graphene-based devices such as pressure sensors, electron-transparent liquid cells, and devices with molecular valves or sieving properties ([75][76][77][78][79][80][81][82][83][84][85]).

In itself, the impermeability of graphene makes it a promising membrane material for the ATOMICAR-design. In addition to that, the fact that graphene consists of only one layer of atoms makes it nearly ideal for the ATOMICAR-design, as it is

difficult to imagine a thinner electron transparent window. It has been observed that bilayer-graphene-sealed SiO_2 cavities can be pressurized to 25 bar above ambient pressure before the graphene-sheets starts to delaminate from the SiO_2 substrate ([86]). Exploiting this property of graphene, the ATOMICAR-reactor could facilitate experiments very close to industrially relevant conditions. Based on these reports in literature, graphene was selected as the sealing membrane of the present ATOMICAR-design. In practice, both graphene and FLG have been used, as both can serve as a thin impermeable membrane, and the transfer yield of mechanically exfoliated FLG is higher than that of graphene.

The first objective of the ATOMICAR group was to reproduce the observations of Bunch et al. ([73]). Bunch et al. reported leak rates between approximately 300 and 2000 molecules per second for ambient air, which is acceptable for the ATOMICAR-project. With these leak rates only very active single atom catalysts can be studied, but nanoparticles can be examined if the collective TOF of the whole particle is large enough. As a consequence, the development of the ATOMICAR-design was prioritized at the expense of studies of the leak rates. When we fabricated many samples similar to those studied by Bunch et al., we observed, just as they did, a great variety of leak rates. Some cavities actually had leak rates too large to be measured. However, since the leak rates were sufficiently low for enough samples, it was not deemed strategic to proceed investigations of the leak rates further. At this stage in the ATOMICAR-project, samples are screened for their leak rates after sealing, before they are considered for further experiments. If the leak rates are low enough, the samples are used.

As described in Section 1.3, the shape of a membrane suspended across a cavity gives indications of the pressure difference across the membrane. In the following section, it will be demonstrated how deflections of a FLG-membrane suspended across a sealed cavity can be used to deduce the internal pressure of the sealed cavity. The same procedures can be employed to determine if any catalysis is taking place inside a sealed cavity. In this way, the following section presents a procedure, which is fundamental to the ATOMICAR-project.

3.1.1 Measurement of the internal pressure of a FLG-sealed SiO_2 cavity

Leak tests of FLG-sealed cavities can be carried out under ambient conditions. However, it is advantageous to conduct leak tests in a chamber with a controllable pressure. In the case that this is not possible, very leak tight cavities cannot be distinguished from cavities that equilibrate instantaneously with the ambient atmosphere, if the cavities are sealed at ambient pressures. Both types of cavities will be in equilibrium with the external pressure of the cavity, when scanned at ambient conditions, and as a result, the FLG-membrane will not deflect in both cases. To solve this issue, the ATOMICAR-group acquired an acrylic pressure chamber, which is large enough to contain an AFM. The PhD-students Tobias Georg Bonczyk and Yanxin

Liu made a setup such that the acrylic chamber pressure can be controlled by a PID loop on a computer dedicated to the setup. In Figure 3.1, a side-view of the setup is shown alongside a zoom on the AFM used by the group - A FlexAFM from NanoSurf. Samples to be investigated are positioned under the AFM situated in the pressure chamber, and the pressure of the chamber is controlled by the adjustment of the position of two valves; one of which is connected to a pump and the other is connected to either N_2 , Ar, or ambient air. The whole setup stands on an anti-vibration stage. The acrylic pressure chamber weighs less than a steel chamber of the same size would, and in this way the total weight positioned on the anti-vibration stage does not exceed the limit of what the stage can handle. Another group have used a similar setup to measure a difference in the leak rate of gasses going in or out of a sealed cavity ([87]). The two methods for measuring the internal pressure of sealed cavities discussed in this section is developed conceptually at group meetings, and Tobias Georg Bonczyk, Yanxin Liu, Zhongli Wang, Edwin Dollekamp, Peter Christian Kjærgaard Vesborg all contributed to the idea.

To sketch how the internal pressure of a cavity can be deduced from AM-AFM measurements of the FLG-membrane sealing the cavity, the leak test of a specific sample is presented. This sample was characterized thoroughly, as it had a low leak rate, which makes it important to be careful regarding the precision of the AFM measurements. When the leak rate of a cavity is low, the rate of change of the shape of the FLG-membrane is slow. If a minute change in the membrane's shape is to be

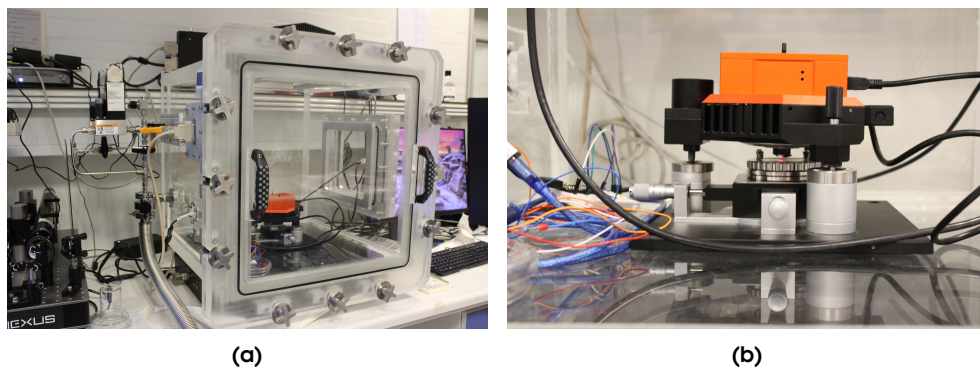


Figure 3.1. (a) Side-view image of the setup used for measuring the internal pressure of sealed cavities. On the left side of the chamber, two pressure controllers can be seen and feedthroughs are installed on both the left and right side of the chamber. Using these, the AFM can be operated while the chamber is closed. (b) The AFM scanner head is positioned on three cylinders above a sample chuck. The sample to be investigated is positioned on the chuck, and the AFM tip is approached the sample until the set-point amplitude is reached. Then a scan can be initiated. On the image, the micromanipulators used to move the sample stage is also seen. The laser light used to measure the deflection of the AFM cantilever can be glimpsed.

detected, high precision is needed. Alternatively, the experiment duration has to be very long for any change to be measured.

The sample to be presented was fabricated as follows: A $1.2\ \mu\text{m}$ thick SiO_2 layer was grown on a polished (100) silicon wafer using thermal (wet) oxidation at 1100°C for 3 hours and 42 min. Structures were defined in a positive resist mask and transferred $1.3\ \mu\text{m}$ into the substrate via a dry etch ($\text{He}/\text{C}_4\text{F}_8/\text{H}_2$). The resist was removed with an O_2 plasma, and a sample was cut from the wafer with a diamond pen. A postdoc in the group, Zhongli Wang, sealed cavities on the sample by mechanically exfoliating a few layers (2 nm thick as measured with an AFM) of FLG onto the sample. An optical image of the sample in question is shown in Figure 3.2. In this image, the SiO_2 layer is blue, and the etched structures appear gray, as the bottom of the etched structures reach the silicon wafer. The area of the sample covered with graphite is darker, and the cavity studied on this sample is indicated with a red arrow. A sample fabricated in this way is expected to be mostly flat. The substrate, made of thermal oxide, is flat, and the thin FLG-sheet is expected to largely conform to the sample ([86]). The etch in the SiO_2 layer is anisotropic, and the cavity walls are therefore presumably straight.

The leak test of the cavity was performed at minimal chamber pressure - below 6 mbar, limited by chamber leak rate. During these measurements, the AFM was equipped with a TAP150GD-G tip from BudgetSensors® with a spring constant of 5 N/m. The sample was placed manually below the AFM scanner head, and as a result of dust particles and sample/sample-holder roughness, the sample was tilted slightly. To accommodate for this, the overall most common tilt in the direction of the AFM scan was removed from the raw data using MATLAB. Furthermore, the most common height on each line was then subtracted line by line. As discussed in Section 2.2, the AFM-topography image is actually an image of the relative positions of the cantilever bottom during scanning. To validate the interpretation of the AFM images as topographic images, the error between set-point amplitude and actual amplitude

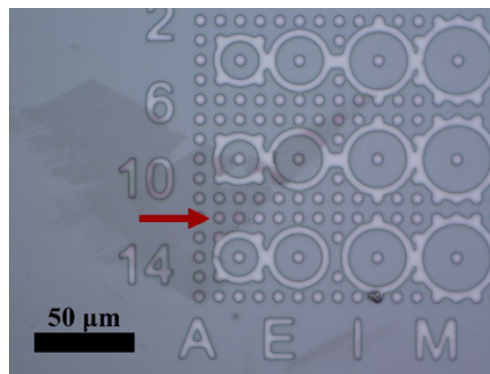


Figure 3.2. Optical image of sample with studied cavity indicated by red arrow.

must be examined. An AM-AFM image obtained below 6 mbar chamber pressure is shown alongside the corresponding error and phase-signals on Figure 3.3a-3.3c.

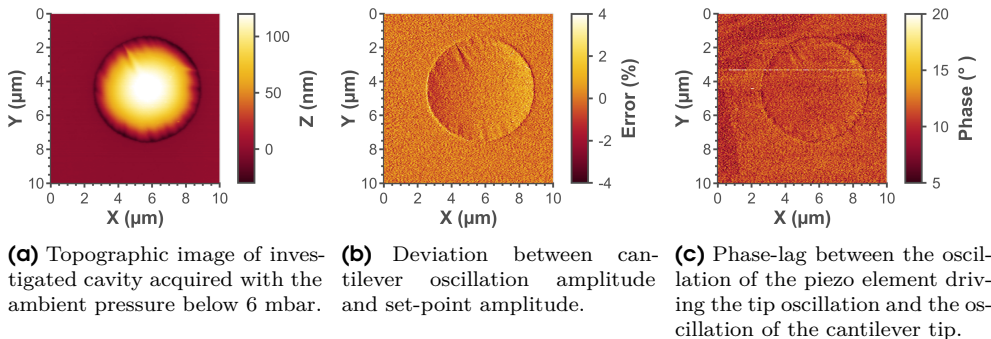


Figure 3.3. AM-AFM signal from a scan of a cavity sealed by FLG (obtained at minimal chamber pressure).

The topographic image in Figure 3.3a is smooth and without indications of an unstable scan. As expected, the sample is flat, except for at the cavities. From the dark contrast at the edge of the cavity, it can be seen that the FLG-sheet follows the sidewalls of the cavity before it releases and bends outwards in response to the pressure difference between internal and external cavity pressure. Similar behaviour is also reported in literature ([73]). To verify that the scan in fact was stable, figure 3.3b should be examined. As a rule of thumb, the deviation between actual oscillation amplitude of the AFM cantilever and the set-point amplitude should be small and constant in areas assumed to be flat. In addition, a similarly low and constant error signal should resume after sudden changes in the topography of the sample inevitably results in higher error signals. The error on the amplitude is seemingly constant in the flat areas of the sample, and at the center of the membrane. The first notable change in the error signal appears, when the cantilever tip is scanned across the cavity edge. The sudden change to a larger average distance to the sample can be seen as a higher oscillation amplitude. Since, the membrane represents a gradual change in surface topology towards the average cantilever position, the error signal is more negative in areas where the PID loop always have to withdraw a little from the sample. The average distance to sample is decreased, and as a result of that, the tip oscillation is reduced. The PID-gains are tuned appropriately, as the cantilever adjust to the changing topography and return to an average error similar to that observed on the flat substrate. On the right side of the bulging membrane, the cantilever have to adjust to the opposite situation. First, the membrane-tip distance is increased, as membrane's deflection decreases towards the edge of the cavity. Then there is a step in height from membrane to substrate. The resulting error signal is opposite in sign to that observed, when scanning the left side of the cavity.

The image of the phase-lag between piezo elements motion and the cantilevers trajectory should not exhibit sudden jumps. In 3.3c, it can be seen that in general

the interaction between sample and cantilever tip is constant. There is some variation in the dissipation of energy to the sample, as can be seen for the areas with darker contrast. A line scan stands out with a larger phase than seen in the rest of the scan. The abrupt nature of the change in the signal indicates that the cantilever oscillation jumped between two modes in this region of the scan. Had this jump between modes happened closer to the center of the membrane and been more dominant in the image, the image had to be discarded. In this case the topographic image is accepted as valid.

To quantify the deflection of the membrane, the maximal deflection of the membrane was determined with MATLAB. The X- and Y-coordinate of the highest point in the background-corrected image were found after using a median filter, and the maximal deflection is defined as the median of 19 by 19 points centered on those coordinates. Cross-sections of the AFM data were used to define zero deflection. 19 lines centered on the line with the highest point is averaged, and a straight line was fitted to the points at which the graphite membrane detaches from the cavity walls. On this line, the Z-value with the same X-coordinate as the highest point was used as a reference height for zero-deflection. In Figure 3.4a, the linear fit is shown as a black line, and the point with the largest Z-coordinate is marked with a red circle. Note that the membrane is not perfectly symmetric.

The maximal deflections measured during the leak test is shown in Figure 3.4b. During the test, the chamber pressure was changed slightly to determine the relation between pressure difference and deflection, as discussed below. Points obtained at minimal chamber pressure is shown in black, and points colored red, blue and yellow

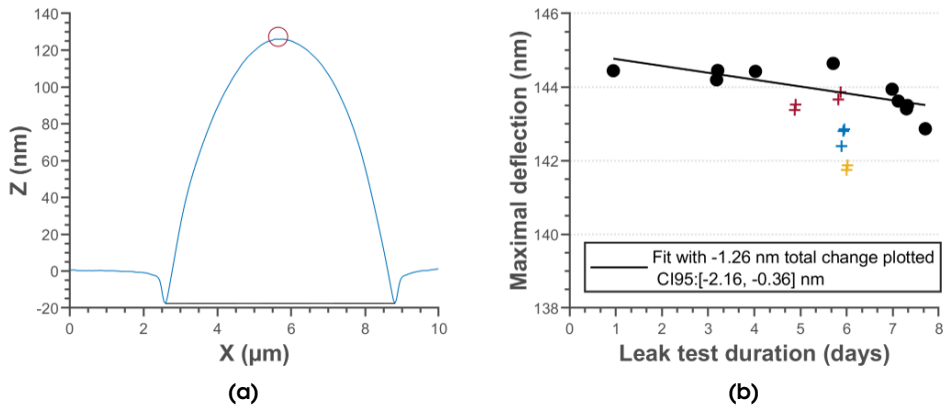


Figure 3.4. (a) Average of 19 lines centered on the scan line with the largest Z-coordinate. A straight line between the lowest points of the cross section is used to define zero deflection. (b) The maximal deflection tracked over time. Measurements colored black were acquired at minimal chamber pressure. As explained in the body text, the sensitivity of the membrane is measured by changing the chamber pressure. The red, blue, and yellow points are obtained at chamber pressures approximately 50 mbar, 100 mbar, and 150 mbar, respectively.

are acquired at chamber pressures at approximately 50 mbar, 100 mbar, and 150 mbar, respectively. Note that the chamber pressure was kept below 6 mbar, except during the pressure sweeps. The overall change in deflection is determined from a linear fit to the black points to be -1.26 nm and between -2.16 and -0.36 nm with 95% confidence interval (CI95). Initially, the chamber pressure was kept at minimal chamber pressure. This was done to get an indication of the leak rate. It is evident from the first measurement points that the rate of change of the maximal deflection is slow. In order to determine how slow, several approaches can be employed. The internal pressure could be determined from analytical models ([85][84]) of a pressurized membrane, but as can be seen in the topographic image of the cavity in Figure 3.3a, the membrane does not have an ideal shape: the membrane is somewhat folded. In addition, it has been reported that the deflection of FLG-membranes cannot be adequately described with analytical methods at all pressures, and therefore another approach has to be developed ([86]). Since the deflection changes slowly, the chamber pressure can be changed slightly in discrete steps while the deflection, δ , of the membrane is measured. In this way, the sensitivity of the membrane, $\Delta\delta/\Delta p$, can be determined experimentally. The duration of the leak tests are short compared to the overall leak test, and therefore it is assumed to have negligible effect on the overall change in internal pressure during the leak test. The maximal deflection measured during the pressure sweeps are plotted against pressure on Figure 3.5. The sensitivity of the membrane in the pressure range considered is then determined with a linear fit to be $-0.19 \text{ \AA}/\text{mbar}$ (CI95: -0.23 to $-0.15 \text{ \AA}/\text{mbar}$), as shown in Figure 3.5.

Now, with the sensitivity of the membrane and the change in deflection measured, the change of internal pressure of the cavity over the course of the leak test can be estimated to be 66 mbar (CI95: [17 mbar, 115 mbar]). This estimate can be validated visually by inspecting Figure 3.4b. None of the measurements collected

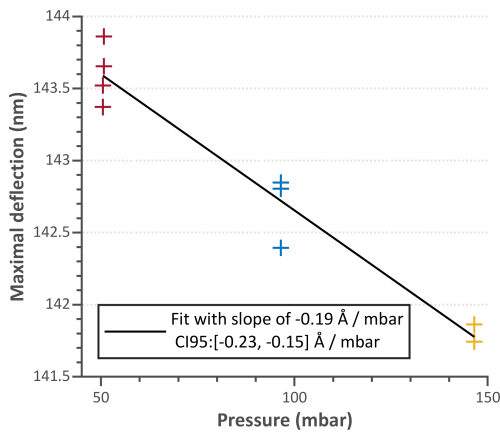


Figure 3.5. Sensitivity of suspended membrane. The pressure surrounding the sample is changed in discrete steps while the deflection of the FLG-membrane is measured.

at minimal chamber pressure (black circles) display deflections like those acquired at 150 mbar. Therefore the estimated upper bound of 115 mbar seems reasonable. Unfortunately, the measurements are not equally spaced in time in this experiment, as a lot of data had to be discarded. This might skew the apparent rate of change in maximal deflection, since the scatter is comparable in size to the total deflection. Furthermore, the lack of additional measurement points makes it difficult to estimate an uncertainty of the individual measurements. In principle, the uncertainty should be determined by measuring the same deflection several times. Unfortunately, the combination of long scan times and the fact that many scans exhibited unstable scanning behavior, made it impossible to collect more. Loud noises in the lab, dirt on the sample, or an exceedingly blunt cantilever tip might cause such unstable behavior. This demonstrates the drawback of the method, which both requires long and precise scans. Both lab conditions and tip-sample interaction have to be constant for long periods of time. Ideally, the leak test should be extended, if the leak rate was to be determined with greater accuracy, but the experiment convincingly demonstrates a procedure for determining the change in internal pressure of the cavity. It is evident from Figure 3.4b that the precision is about a nanometer. For the extraordinary slow change in internal pressure investigated here, greater precision would be preferable, but it is without doubt sufficient to determine changes in internal pressure relevant for catalysis. This can be seen by estimating the change in molecules per second.

Using a temperature of 293 K and the volume of the cavity, the pressure change can be converted to a time-averaged leak rate. Since the cavity depth and diameter is approximately 1.3 μm and 6.5 μm , respectively, the leak rate from the cavity can be estimated to be 121 molecules/s. The estimated leak rate is comparable in size to the expected total TOFs of nanoparticles, and so the accuracy is sufficient for tracking changes in internal pressure caused by a catalytic process. Furthermore, it can be concluded that with a FLG-sheet of this width and thickness a pressure change of $\propto 0.1$ bar can be detected, when the partial pressure difference is $\propto 1$ bar. Interestingly, the estimated leak rate is about three times lower than the lowest leak rate reported for ambient air in literature ([73][85]). A draft (see appendix) has been written based on the measurement of the record low leak rate, and a preliminary verification of the existence of low leak rates with EELS is included in the draft as well.

In the experiments discussed in this thesis, a change in the internal pressure of the cavity can only be due to a leak, but the same methods, described herein, could be employed while catalysis takes place in the cavities. In this case, the catalytic conversion of known partial pressures of reactants to products could be studied via measurements of the membrane's deflection. This method can be utilized to reveal changes in internal pressure of a sealed cavity, but the initial pressure should be known, before absolute pressures can be determined from this procedure. To measure the absolute internal pressure of a sealed cavity from the membrane shape another approach needs to be employed.

The method described in this section until this point can be time consuming as the requirement for precise AFM scans is in effect a requirement of very slow

scans. Alternatively, the chamber pressure can be changed until the deflection of the membrane changes from being outwards to inwards. At the point where the direction of the deflection changes, the internal pressure changes from being higher to being lower than the external pressure. In this way, the absolute internal pressure can be determined with the same accuracy as such a change in deflection can be determined. Since, the sensitivity of the suspended FLG-membrane is largest when the pressure difference across the membrane is small, the absolute internal cavity pressure can, in principle, be obtained with great precision. The maximal deflection, ω , of a pre-stressed cylindrical symmetric membrane under a transverse uniformly distributed load can be described analytically at the center of the membrane ([66]):

$$\omega = \left(\frac{a^4 q}{2hE} \right)^{1/3} K, \quad (3.3)$$

where a is the radius of the membrane, q is the load, in our case the pressure difference across the membrane, h is the height of the membrane, E is Young's modulus, and K is a constant for the membrane at a specific pressure difference. From this equation it is clear that the larger the pressure difference is, the less sensitive the membrane is. When the strain in the membrane is low, the measured deflection of the FLG-membrane might depend on the scanning parameters of the AFM. In this case, the membrane is more pliable, and it is therefore more likely that a flat membrane is not imaged as being so. It has been shown in literature that the distance from the equilibrium position of a cantilever to the sample differs from a FLG sheet on a SiO₂ substrate to a pliable FLG-sheet ([88]. see also supplementary information of ref. [73]). Hence, the assumption that the distance between the cantilever and the sample is constant throughout a scan of a cavity with a suspended FLG-membrane is not always valid, and in this case, the map of the relative position of the AFM cantilever is not a topographic map. Fortunately, the effect can be accounted for by calibration measurements of the oscillation amplitude of the cantilever as a function of the distance to the surface ([73][88]). In addition to this, it is important that the membrane is scanned using the same type of oscillation amplitude. If the the cantilever motion shifts between two types of oscillations, the deflection can be overestimated. An experiment was conducted to demonstrate this.

A cavity with a mechanically exfoliated FLG-membrane (≈ 10 nm thick) was scanned with a "soft" tip (TAP150GD-G tip from BudgetSensors® with a spring constant of 5 N/m) at varying oscillation amplitudes. The cavity is situated on an electron transparent sample, and hence the background is not flat, as there are large stresses in the thin films, in which the cavity is etched. As in the measurement described above, the most common tilt in the scan direction is found globally and the subtracted from each line of the raw image. Subsequently, the average of the most common heights in each line are then subtracted line by line. There is some drift between the acquisitions, and to correct for this, the maximum height of a feature

beside the cavity is used to align the scans. Line scans, which contain the maximum of the feature, from the different scans are presented in Figure 3.6.

At first glance, the difference in the profiles is surprising. It is often assumed that for otherwise constant scanning parameters, larger oscillation amplitudes correspond to larger tip-sample interaction. However, as seen on Figure 3.6, the maximal deflection of the membrane does not scale continuously with the oscillation amplitude. In fact, the linescans show a sudden jump in maximal deflection, when going from 1 V to 5 V, and for 4 V, the jump actually happens in the middle of the line scan. This indicates that in this specific experiment, the difference in maximal deflection is not due to a difference in oscillation amplitude entirely: The scans are acquired using different types of oscillations. As discussed in Section 2.2, it is known that several types of oscillations can exist at the same time in amplitude modulated AFM measurements. To examine, if this indeed was the case in this experiment, the driving frequency of the cantilever was tuned until the FLG-membrane could be imaged at 5 V using the same type of oscillation amplitude as used for lower oscillation amplitudes. It is evident from Figure 3.6 that the line scan acquired by using another part of the cantilevers resonance curve ("5Vtuned"), produces approximately the same profile as those obtained with oscillation amplitudes of 1 V and 2 V. From this experiment, it can be concluded that it is important that the tip-sample interaction is kept constant during a pressure sweep. A shift between the two types oscillations can change the measured deflection, and the data can be misinterpreted. In this situation the deflection change is overestimated, and the point, at which the sign of the deflection changes, might as well be overestimated.

In this section, it was discussed, how the shape of FLG-membranes, suspended across sealed cavities, can be used to deduct the change or absolute value of the internal pressure of these cavities. Besides this, AFM measurements can provide valuable insight into membrane symmetry and the adhesion to the side-walls of the cavities. However, it is a general problem that AFM measurements are relatively slow. This is not an issue for the experiments presented in this section, but it can be problematic. With the AFM used in this PhD-project, it is difficult to achieve precise AFM data (resolution about a 1 nm) of an area $10 \times 10 \mu\text{m}$ in size, if the total scan time per image is less than half an hour. In the case, that any statistical analysis is to be performed on the data, several scans are needed. AFM experiments can therefore be time consuming, which is impractical, and it can limit how accurately an internal pressure can be determined. Preferably, the change of the internal pressure of a cavity should be negligible within the time frame used to determine it. Otherwise, the precision, with which the internal pressure is known, is reduced. Therefore, highly accurate data can only be obtained with AFM for samples with a slow change in the internal pressure. To account for this, the scanning time can be increased at the expense of measurement accuracy, and larger differences in internal pressure is detectable with greater time resolution. Furthermore, the impact of a specific rate of catalytic conversion on the internal pressure of a sealed cavity can be tuned by choosing different cavity sizes. Thereby the rate of change of internal pressure can be engineered to accommodate for the slow acquisition time for AFM measurements.

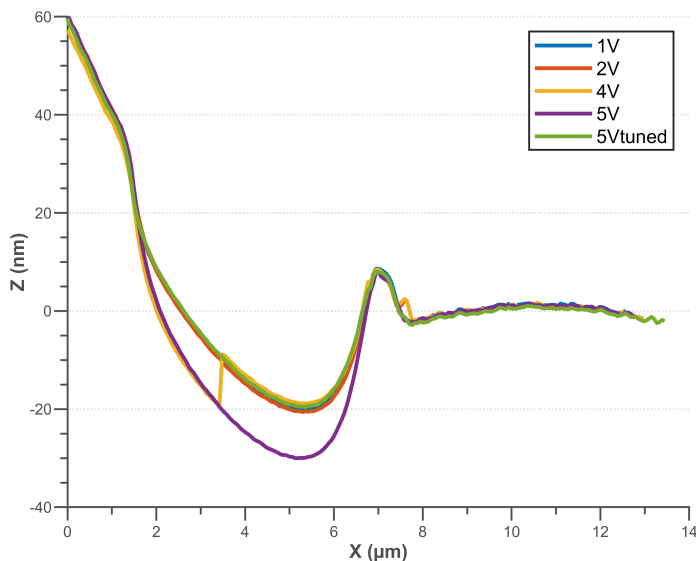


Figure 3.6. AFM linescan of cavity covered with FLG acquired at oscillation amplitude from 1 – 5 V. The linescan referred to as "5Vtuned" is acquired with a different driving frequency than the rest of the scans. Note that the scans acquired with 1 V and 2 V are overlapping.

In conclusion, time resolution and spatial resolution has to be balanced.

EELS can also be used to detect the change of the partial pressure of a gas-species, and it has the further advantage that the partial pressures, rather than the total pressure, can be measured. The gas composition of captured gasses can only be inferred from the measurement of the absolute pressure, if the ratio of products is known a priori. Alternatively, the total pressure is more an indication of a catalytic activity than a measurement. EELS signals are characteristic for the atomic species probed, and the intensity (for small t/λ) is proportional to the density of the gas species, as described in Section 2.1.1.1. Exploiting this fact, the partial pressures of captured gas species can in principle be monitored individually with EELS. This will be demonstrated in Section 3.4.

The two complimentary techniques can be combined and, in this way, many cavities can be screened with two independent methods, and then important chemical information can be obtained from spectroscopy. The following section will discuss the present ATOMICAR-design, which is electron transparent.

3.2 How should an ATOMICAR-device be structured?

After a transfer of FLG onto a sample has been attempted, the success of the transfer can be investigated using a microscopy technique. It is without doubt easiest to

evaluate the transfer, if the FLG is optically visible. Optical microscopes have a wide field of view, and the sample can easily be examined quickly. However, since FLG is very thin, it is difficult to see on wafers. However, appreciable contrast can be obtained on thin films ([89]), and it would be an advantage, if the ATOMICAR-device had a thin film on the front side. Several different thin films can be deposited or grown in the cleanroom, but if equipment with metal contamination is disregarded, the possibilities are limited to: Amorphous and poly-crystalline silicon, LPCVD SiO₂ and SiN_x and thermally grown SiO₂. These materials are also often assumed to be catalytically inactive, and they are therefore relevant for the ATOMICAR-project.

It is logical to assume that a strong adhesion between FLG and a substrate results in high transfer yield for FLG-transfer techniques. FLG adheres to substrates like SiO₂ via van der Waals interactions ([90]), and the total interaction strength is determined by the area of interaction and the polarizability ([10]) of substrate and FLG. The polarizability of metal oxides are relatively material independent ([91]), hence it is assumed in this thesis that it is the roughness of the substrate that determines the strength of the interaction. Note that all the considered materials are likely to have a native oxide layer ([92][93]). It is the ATOMICAR-groups experience that is difficult to transfer FLG to rough substrates, such as poly-crystalline silicon, and earlier version of the ATOMICAR-design with poly-crystalline silicon on the front side was nearly impossible to coat with FLG using mechanical exfoliation.

FLG is known to conform to substrates ([86]), but during a transfer process, FLG is initially on a carrier substrate (a polymer or a graphite-stack). These are relatively flat, and it is the roughness of the initial carrier of the FLG that the ATOMICAR-device needs to match. The preferred loading technique is mechanical exfoliation, and the graphite stacks are atomically flat ([94]). In conclusion: The front side of an ATOMICAR structure should therefore be a thin film and have the lowest possible surface roughness.

To investigate the roughness of the listed thin films, wafers were prepared with either amorphous silicon, LPCVD SiO₂, LPCVD SiN_x or thermally grown SiO₂. Approximately 172 nm of LPCVD SiO₂ were deposited with TEOS (tetraethoxysilane) over 20 min in a furnace at 712 – 720 °C at 190 mTorr. Another similar furnace was used to deposit 657 nm amorphous silicon at 562 – 565 °C and 200 mTorr in a SiH₄ gas flow. In yet another furnace, 354 nm LPCVD silicon nitride was deposited on a wafer at 810 – 845 °C and 150 mTorr in a flow of NH₃ and SiH₂Cl₂. In addition, a wafer was oxidized in a fourth furnace at atmospheric pressure at 1150 °C for 7 hours and 20 min with water vapor, which resulted in an oxide thickness of 2062 nm. Poly-crystalline silicon was not considered. The thin films were assessed with a VASE Ellipsometer (J.A. Woollam), and the thicknesses were determined from fits to the acquired optical data. Since, the thicknesses estimated from this method have been observed to correlate well with complementary methods of determining the thickness of films (AFM and SEM), it is used to ensure that the thin films were many atomic layers thick, although the precision of the estimated thicknesses is not generally determined.

Areas $0.5 \times 0.5 \mu\text{m}^2$ in size were scanned with the AFM from NanoSurf at three

positions at least $1 \mu\text{m}$ apart on each sample. Both forward and backward scans were considered as independent measurement points. In between the measurements the cantilever was withdrawn and approached to make the measurements truly independent. A Tap190Al-G cantilever from BudgetSensors® was mounted on the scanner head of the AFM, and using the open-source software Gwyddion, the tilt was removed from each line by linear interpolation. The roughness was determined as the root-mean-square of the heights for lines on the samples without large dirt particles, which was excluded manually from the data analysis. Besides these four wafers, a bare silicon wafer and an ATOMICAR-device was included for reference. The measured mean roughness is shown in Figure 3.7 (uncertainty estimated from the standard deviation). Prior to the roughness measurements, all wafers were stored in the cleanroom, and on the day the roughness measurements were carried out, the wafers were cleaned in a plasma asher from TePla (model 300 Semi Auto Plasma Processor) for 10 min at 1.25 mbar in a flow of O_2 and N_2 (flow ratio 400 : 70) and 1000 W.

The (100) silicon wafer is polished, and it is traditionally assumed to be atomically flat. With this in mind, the roughness measured on the silicon wafer can serve as a measurement of the minimal resolvable roughness with the AFM settings used. Thermally grown SiO_2 has a roughness very close to that of the bare silicon wafer, and the measured value is in close agreement with other groups measurements ([86]). Silicon nitride, LPCVD silicon oxide, and amorphous silicon exhibit greater roughness. In conclusion, thermally grown SiO_2 is the flattest thin film. From this, it is evident

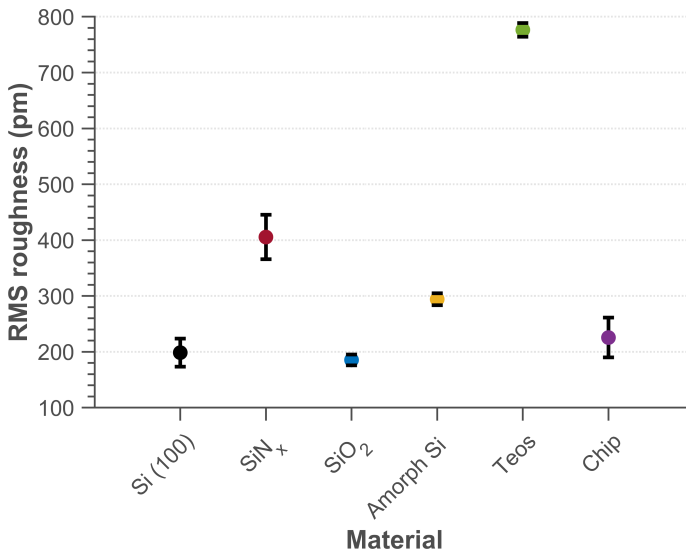


Figure 3.7. The roughness of different thin films deposited on silicon (100) wafers. A bare (100) silicon wafer is included as a reference. An ATOMICAR-device is also included to illustrate that the present design reach minimal roughness (called "chip").

that the front side of the ideal ATOMICAR device is composed of thermally grown SiO_2 . The present ATOMICAR-design is constructed to meet this requirement, and to illustrate the successful implementation of that in the design, the roughness is also measured on an ATOMICAR-device referred to as "chip". The ATOMICAR-device had been stored outside the cleanroom before this investigation, and it was therefore contaminated with many particles, making the roughness vary somewhat between measurements. It was cleaned in a plasma cleaner from SEREN - Industrial Power Systems (Model: PM313) at 120 W in a flow of oxygen for 10 min, but this only removes organic residue.

The ATOMICAR-devices are fabricated on a wafer, as will be described in detail in the following section, and then individual devices, "chips", are cut from the wafer. Before the wafer, with the "chip" investigated here, was cut into smaller pieces, the roughness was measured in the cleanroom with another AFM (equipped with a TAP150Al-G cantilever). The wafer was scanned over areas $0.5 \times 0.5 \mu\text{m}^2$ in size twice and the roughness was determined to be 179.9 pm and 175.7 pm, respectively. This underlines that the ATOMICAR-design has a front side roughness comparable to that of thermally grown SiO_2 . One of the main tasks of this PhD project has been to reach this goal, and the following section will describe a design that achieves this. Other materials could have been used, if the samples were polished, but great care have to be taken, if scratches ([95]) and variations in thin film thickness across the wafer is to be avoided with this method. If the height of the cavities vary, it is more cumbersome to distinguish between TOFs from measured FLG-membrane deflections, since a difference in volumes results in a difference in the rate of change of internal pressure for equal TOFs. Preliminary tests of polishing showed thickness variations, and since there was little know-how in the group about polishing, it was deemed easier to start with a flat front surface than creating one. Furthermore, many studies of the leak from FLG sealed cavities in literature is conducted on cavities etched into SiO_2 ([73][86][85][84][87][96]), and this is another argument for using SiO_2 as the front side material. The surface of a bare silicon wafer could in principle also be used, but as described above, this would make it difficult to find FLG transferred to the ATOMICAR-device.

Different topographies can have similar roughness. To verify that the front side of the ATOMICAR design indeed is locally flat, an image of thermal SiO_2 is shown on Figure 3.8 alongside an AFM scan of the ATOMICAR design acquired in the cleanroom. At first glance, the image shown in Figure 3.8a is of lower quality than that of Figure 3.8b, as there appears to be a small mismatch between the individual line scans. This is due to the fact that the variation in topography is close to the detection limit of the AFM at its present state, as concluded from scans of the (100) silicon wafer. More importantly, it can be seen that the low roughness measured on both samples is due to an overall small feature size. Now that it has been established that the front side of an ATOMICAR-derived design should be flat, and possibly of thermal oxide, the next design task is to fabricate electron transparent cavities in this substrate. Furthermore, the electron transparent regions should be able to withstand all FLG-loading methods considered. The pro and cons of different loading methods

were discussed in Section 2.4, and the ATOMICAR design should preferably not be limiting the choices. However, as part of the procedure of mechanically exfoliating FLG onto a substrate, a finger has to be pressed hard against the substrate. Thermally grown SiO_2 is a relatively weak material, and slab with electron transparent cavities cannot exclusively consist of SiO_2 . The solution to this problem is introduced in the following section.

3.2.1 3D structure of the ATOMICAR-design

Wafers are between $350 - 1000 \mu\text{m}$ in thickness, and are not electron transparent. Accordingly, cavities etched into a front side SiO_2 layer will not be electron transparent either, unless most of the material underneath the cavities are removed. The most simple solution to this problem is to create several freestanding slabs of SiO_2 in which cavities are etched. Various methods can be used to remove silicon underneath a membrane, either a wet etch or a dry etch can be used ([61]). Since, the preferred FLG-transfer method is mechanical exfoliation, the positions of transferred FLG-flakes on the ATOMICAR-devices are random. To compensate for this, the density of transparent cavities should be as high as possible and distributed over as wide a range as possible. The range of motion of the sample holder used for the TEM is only $2 \times 2 \text{ mm}^2$, making it even more important that the density of cavities is high. Otherwise, too many samples will not be sealed successfully.

With an anisotropic etch, many deep trenches can be positioned close together. Unfortunately, deep dry etches suffer from transport limitations, and the etch rate drops rapidly, when etching structures with high aspect ratios ([97]). Choosing the thinnest type of wafer, $350 \mu\text{m}$ in thickness, the highest aspect ratios can be achieved. The maximal achievable etch depth of a certain geometry is sample and process

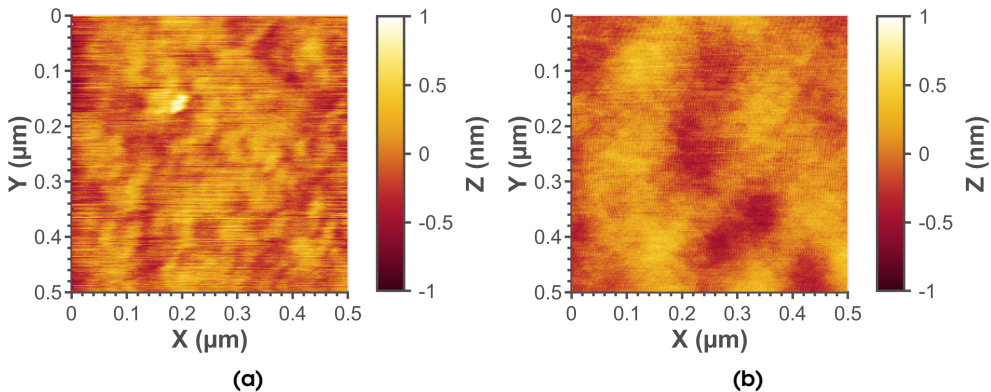


Figure 3.8. a) AFM topography image of thermally grown SiO_2 acquired as a part of the roughness measurements. b) AFM topography image of ATOMICAR-device obtained in the cleanroom.

specific. It depends on the areal density of structures to be etched into the wafer, the density of etchants, and plasma ion flux. To save time, the anisotropic etch of the bulk silicon wafer was not optimized, but etching recipes characterized by cleanroom personnel was used. The freestanding SiO_2 slabs were made $35\ \mu\text{m}$ wide, $300\ \mu\text{m}$ long, and as deep as the wafers.

Any deposited layer on top of the front side SiO_2 should be removed after it has served its purpose. Otherwise, the front side roughness will be increased. However, micro-fabrication relies on the possibility of defining structures layer by layer. Many microfabricated devices are fabricated from the bottom and up, and material underneath structures defined in this way is removed as the final step in the fabrication process. An ATOMICAR-device should only have structured SiO_2 on its front side, and since the oxide is grown directly on the surface of an untreated silicon wafer, one could conclude that the free standing slab can only be made of SiO_2 . However, SiO_2 is not a very strong material ([98]). Therefore, the free-standing slabs have to be several microns thick to withstand the pressure applied to it during mechanical exfoliation. This is unpreferable, as this will increase the volume of the cavities, making the internal pressure of the cavities less sensitive to catalysis. The problem will only increase, if the freestanding slabs are widened at some point to increase the cavity density on the front side, and therefore this type of design is not scalable to an optimal high density of cavities (wide freestanding slabs densely spaced). To circumvent this obstacle, the etch through the wafer was implemented as one of the first steps in the fabrication procedure, and thereby additional layers can be deposited on the backside of the oxide slabs after the silicon beneath them has been removed. With this method, the slabs can be constructed to be composed of layers of any type of material still with thermal SiO_2 on the front side. Alternating between different layers of silicon nitride, silicon oxide and silicon, the freestanding slabs can be made wider without compromising the depth of the cavities. This top-down growth of layers is a very important feature of the ATOMICAR design, and besides the possibility of engineering the strength of the slabs it also makes it easier to control the variation in cavity bottom thickness' across a wafer, as discussed below.

Dry etches have varying etch rates across the wafer. For the equipment used to etch silicon oxide, the variation is in the best case 0.7% (characterized by cleanroom personnel). In the case of a $2\ \mu\text{m}$ deep cavity, this is equivalent to 14 nm. This is a large variation in etch depth compared to the optimal bottom thickness (16–100 nm). It is therefore advantageous to introduce a so called "stop-layer". By implementing a silicon layer beneath thermal SiO_2 , this problem will be solved: Since the etch recipe used for etching silicon oxide has a much lower etch rate in silicon, the etch in effect stops on a silicon layer, and the etch depth is then constant across the wafer. If an subsequent silicon etch is selectively etching the silicon, and not the layer beneath it, the cavities will continue to have equal depths.

In the present design of the ATOMICAR chips, $2\ \mu\text{m}$ thermal SiO_2 is grown on a polished (100) silicon wafer. Then $1\ \mu\text{m}$ of LPCVD amorphous silicon is deposited on the backside of the freestanding SiO_2 slabs, after the material beneath the front side SiO_2 has been removed. The silicon layer is stronger than silicon oxide ([99]), and

in this way, the material with the largest strength is the one being bend the most, when the freestanding slabs are pressed from the front side. The chosen thickness are deliberately selected to be thicker than theoretically necessary, as the thin film tensile strength can vary and defects can weaken the structures. Furthermore, the slabs should also be thick enough to withstand the different process steps before the strengthening layer is deposited. It has been observed, both by the author and Tobias Georg Bonczyk, that slabs can be damaged in ways during the fabrication process making the samples unusable for further processing. Instead of characterizing the thinnest possible slab with the chosen slab width, it was decided that it was more important to reach a working device than optimizing a device that did not work yet.

The final layer on the bottom of the freestanding slabs will in the ATOMICAR-design also be the electron transparent bottom. Amorphous silicon has a low roughness, and it is therefore preferred above poly-crystalline silicon. In this way, the template on which the electron transparent bottoms are grown/deposited has a low roughness. In previous versions of the design, poly-crystalline silicon was preferred, as it grows faster in the furnace used for silicon deposition. However, this resulted in thickness variations in the deposited electron transparent cavity bottoms. Such a contrast is not convenient, when large overview images of the cavities are inspected to identify single nanoparticles. To keep the device simple until all requirements to its performance are met, no additional strengthening layers were deposited.

The cavity bottom material should not contain the atomic elements, which is also present in the gasses to be investigated with EELS. This would make it more difficult to study the evolution of the gas signal, if it is partially buried in the signal from the cavity bottom. SiO₂ was deposited on the backside of the freestanding slabs using TEOS, and thereby the leak rates of nitrogen in ambient air could be studied. Anton Simon Bjørnlund (PhD student at DTU VISION), has shown on earlier versions of the design that gaseous oxygen can also be studied through these membranes, whereas this is not possible on PECVD deposited SiO₂ available in the cleanroom. Deposited thin films preserve the roughness of the template, on which the film is grown upon, whereas the growth rate of oxide in silicon differs between different crystal facets ([62]). Therefore, an oxide grown on silicon deposited as amorphous (which will crystallize during oxidation [99]) will have an unfavourable shape ([100]). The evolution of the cross section of the ATOMICAR-devices through the fabrication process is illustrated in the next section.

SEM images of the front side and cross section of the present design are shown in Figure 3.9. The arrangement of freestanding slabs and cavities can be seen on the image of the front side (Figure 3.9a). By using an acceleration voltage of 30 keV, areas with freestanding slabs stands out from the bulk silicon substrate by their brighter contrast. In order to ease navigation between different freestanding slabs, the slabs have been arranged in 16 groups each with 9 slabs. Thereby the full x/y-range of the TEM sample-holder is used. The group number is denoted by a number on a horizontal slab, and the slab number is etched directly into the slab. During the transfer of FLG to the device, the center part of the numbers often break, but it does not affect the recognizability of the numbers. The cavities are arranged in

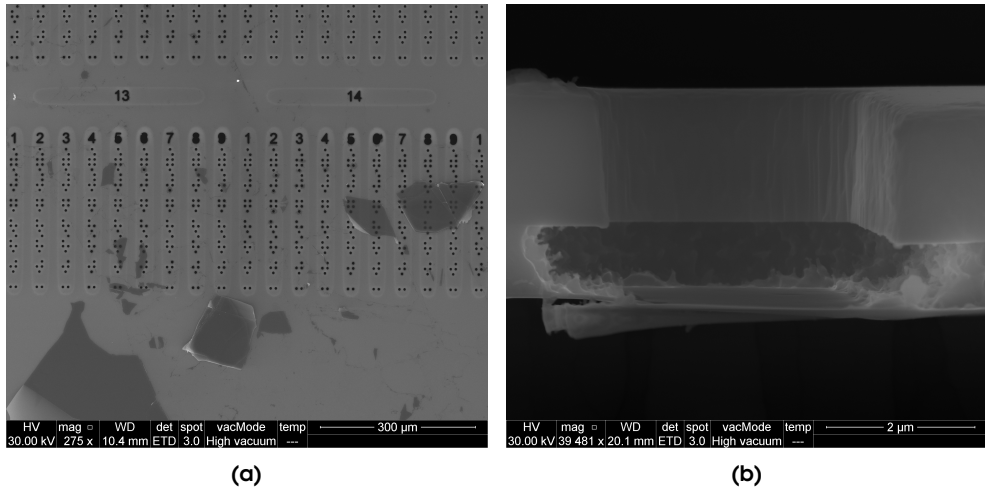


Figure 3.9. (a) Overview SEM image of the front side of ATOMICAR-device with FLG. The electron transparent cavities are etched into freestanding membranes (long oval structures) and distributed in a recognizable pattern. The freestanding slabs are arranged in 16 groups each containing 9 slabs. (b) Cross section of structure etched into a freestanding slab. At the top of the slab is an approximately $2\ \mu\text{m}$ thick thermal SiO_2 layer. Just below is a strengthening amorphous silicon layer, and at the bottom a thin TEOS-derived SiO_2 layer, which is seen suspended across the bottom of the etched structure.

patterns to ease the location of the different cavities on the specific slabs in the TEM. In the TEM used, the lowest magnification, which can be used without compromising the stability of the microscope imaging optics, is 3400. As a result, the electron microscopist will never have more than a few cavities in the field of view. This fact makes it difficult to navigate between the many cavities of the ATOMICAR-device, since only the cavities and slabs are sufficiently electron transparent to be studied in a TEM. Instead of using additional space for writing letters or numbers on the slabs, the cavities are arranged in patterns, which denote the position of the cavities on the individual slab. The cavities are arranged in groups, each with six cavity positions bounded by a cavity in the middle of the slab both above and below these six positions. Inspired by Braille numbers, the cavities are then placed (or not placed) at the six positions. With this arrangement, the position on the slab as well as the sample rotation can be identified at large magnifications.

The overview image in Figure 3.9a demonstrates that the device is strong enough to withstand FLG transfer. Graphite/FLG stacks was transferred to the device by Edwin Dollekamp (Postdoc in the ATOMICAR-group) using mechanical exfoliation, and areas covered by FLG/graphite can clearly be identified by their dark (or in some cases bright) contrast. As noted above, the density of cavities has to be high in order to ensure practical transfer yields to areas with cavities.

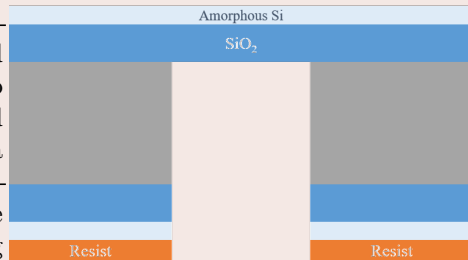
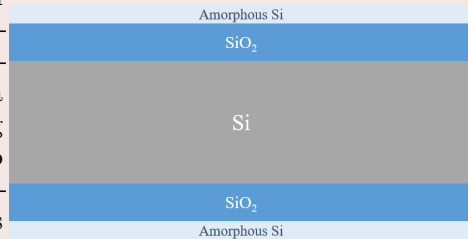
In Figure 3.9b, a SEM image of the cross section of a structure etched into a freestanding slab is shown. Both the front side thermal SiO₂ layer, the strengthening amorphous silicon layer, as well as the electron transparent bottom made of TEOS-derived SiO₂ can be identified. The anisotropic etch through thermal SiO₂ layer results in straight side walls with striations, i.e. resist mask roughness transferred into the SiO₂ ([101]). As discussed above, it is preferable, if the etch of the silicon only etches silicon. An isotropic etch of silicon was used to achieved this, and the isotropic nature of the etch can clearly be seen from the undercut of the etch- the etch of the silicon layer beneath the front side SiO₂ layer. The electron transparent bottom can be seen to be suspended across the bottom of the etched structure. The next section will present the fabrication procedure that has been used to achieve this type of device.

3.2.2 Fabrication procedure

PROTOCOL

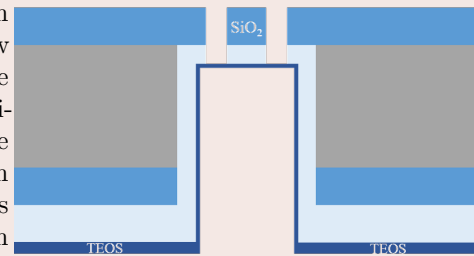
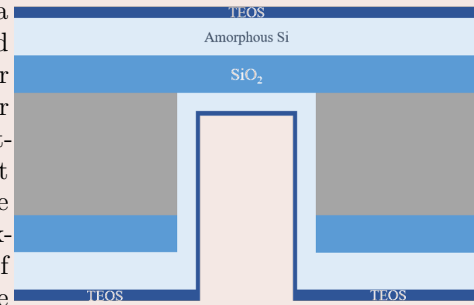
2 μm thermal SiO_2 was grown at 1150°C for 7 hours and 20 minutes on a $350\ \mu\text{m}$ thick double-side-polished wafer (100-orientation). Amorphous silicon was deposited at 200 mTorr over 7 hours at a temperature between $562 - 565^\circ\text{C}$ using SiH_4 . The additional layer was added to protect the front side of the wafer during process steps, in which the wafer is placed with the front side on different chucks.

A positive resist was used as a mask for two Bosch processes (C_4F_8 used during sidewall passivation and SF_6 and O_2 during etching), the last of which uses a low-frequency platen generator to avoid notching ([102]). Notching would be detrimental to the stability of the free-standing slabs, as the etch profile would deviate from a directional etch close to the front side SiO_2 , thus widening and weakening the slabs without making a larger transparent area. With these process steps, trenches were created on the backside of the wafer, and free-standing slabs were created on the front side. Before the Bosch processes were used, the protective Si and thermal oxide were removed in areas on the backside not covered by resist using two dry etches ($\text{He}/\text{C}_4\text{F}_8/\text{H}_2$ and $\text{C}_4\text{F}_8/\text{SF}_6$).

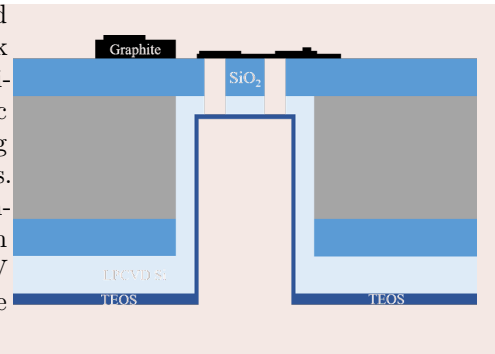


The resist was removed using oxygen plasma, and a second 1 μm thick amorphous silicon layer was deposited via a LPCVD-process (same parameters as before). The final thickness of the strengthening silicon layer is difficult to determine, as it was deposited through trenches in the backside of the wafer, and therefore not easily accessible in a non-destructive way. A TEOS-derived SiO_2 layer was deposited at 190 mTorr at 712 – 720°C over 15 min. This layer acts both as electron transparent bottom of the to-be-etched cavities, but also as a stop layer for etches in the strengthening silicon layer. Note, the oxide layer is thinner on the backside of the freestanding slabs than everywhere else. This is because the narrow opening of the trenches limits the transport of the gas-molecules to the backside of the free-standing slabs. Since, the TEOS-derived oxide is deposited at high temperatures, the deposited silicon layers probably crystallize during this fabrication step to some extent.

The deposited SiO_2 was removed from the front side using a dry etch of the oxide ($\text{He}/\text{C}_4\text{F}_8/\text{H}_2$), and then an isotropic silicon etch with SF_6 at low platen power was used to etch the LPCVD deposited silicon layer. A positive resist was used as a mask, and the oxide etch was used to create cavities in the thermal oxide layer. The etch was continued, after removing the resist with O_2 plasma, by using the isotropic etch process again.



Finally, the wafer was cut into chips and sealed with FLG. Tobias Georg Bonczyk uses a Laser Micromachining Tool (microSTRUCT vario from 3D-Micromac AG) to cut the wafers without damaging the electron transparent cavity bottoms. The samples are cut to fit in a Gatan Single Tilt Heating Holder model 628 with an inconel furnace or a FEI NanoEx IV holder ([103]), depending on whether the samples are to be heated or not.



At the end of this fabrication process, 50 identical ATOMICAR-devices have been fabricated on each wafer treated as described in the protocol. The wafers can then be inspected in an optical microscope, but the electron transparency of the cavities cannot be assessed without a TEM. To access the homogeneity of the electron transparent cavity bottoms, chips cut from the wafer can be investigated with EFTEM. If the isotropic silicon etch has not removed all of the silicon from the bottom of the cavity, small islands of silicon are left in spots across the cavity. This has been experienced with many batches of ATOMICAR-devices, and to investigate this phenomena Tobias Georg Bonczyk, Anton Simon Bjørnlund and this author in collaboration imaged and etched several chips for different periods of time with the isotropic silicon etch. Two t/λ images from this investigation are presented in Figure 3.10 (data treatment with DigitalMicrograph®). Both images were acquired at 300 kV, without objective aperture, and with an energy selecting slit 10 eV in width. It is important that the objective aperture is not inserted, otherwise the difference in collection efficiency between plasmon and zero-loss signal has to be considered. Unfortunately, the width of the free-standing slabs restrict the actual scattering angles in one direction. This is neglected in the following analysis, as the cutoff angle in the worst case is ≈ 20 mrad (determined from height of wafer and approximate smallest distance from cavity edge to slab edge). Since, the inelastically scattered electrons are scattered to higher angles than the elastically scattered electrons, the t/λ ratios are underestimated. According to theory, the higher the energy of the beam electrons is, the smaller the characteristic scattering angle is ([51]). With this in mind and the fact that it has been shown that the t/λ ratio is approximately constant above 25 mrad for SiO_2 at 200 kV ([104]), the underestimation is likely small.

In both images of Figure 3.10, the edge is included in the upper left corner of the image, and from the color scale, it can be seen that the thickness of the LPCVD silicon islands extending beyond the edge in some regions of Figure 3.10a are much thicker than TEOS-derived oxide layer. Thick regions can be found further away from the cavity edge on this sample, and this is problematic. It would be difficult to get atomic information about small single nanoparticles situated on top of an LPCVD island, let alone be able to see them. To solve this issue, ATOMICAR-devices can be taken back into the cleanroom, and the isotropic etch can be applied once more. After additional etching, images like 3.10b can be obtained. After this additional silicon

etch, the mean thickness is determined in the region only with a transparent bottom to be $0.27 \pm 0.03t/\lambda$, and it is evident from the image that the cavity bottom is quite homogeneous. According to ref. [104], this corresponds to a thickness of 67 ± 8 nm. With this thickness, atomic information can be gained, but future batches should preferably have thinner windows. Shorter duration of deposition of TEOS-derived oxide will achieve this.

The additional etch step has the disadvantage that the etch of the silicon layer below the SiO_2 layer is increased. This increases the total volume of the cavity, without widening the area a FLG can be suspended across. As a result, it requires longer time to investigate leak rates, or, at some point, catalysis with devices, which have been further etched. In addition to this, it also increases the area of the cavity bottom, making the electron transparent membrane wider. This probably makes it more fragile and flexible, which for even thinner membranes could result in too much bending of the cavity bottom. In conclusion, only devices that must have a homogeneous bottom thicknesses should be etched until all of the silicon is removed from the cavity bottoms, especially as the central part of the membrane have no silicon residues without additional etching. Further development of the ATOMICAR-device should seek to develop an anisotropic etch of the amorphous silicon layer, which does not etch SiO_2 .

With a device that can facilitate the investigation of nanoparticles, the next step is to deposit nanoparticles. There exists many ways to deposit nanoparticles on a sample, but the ATOMICAR project would benefit from a directional deposition of

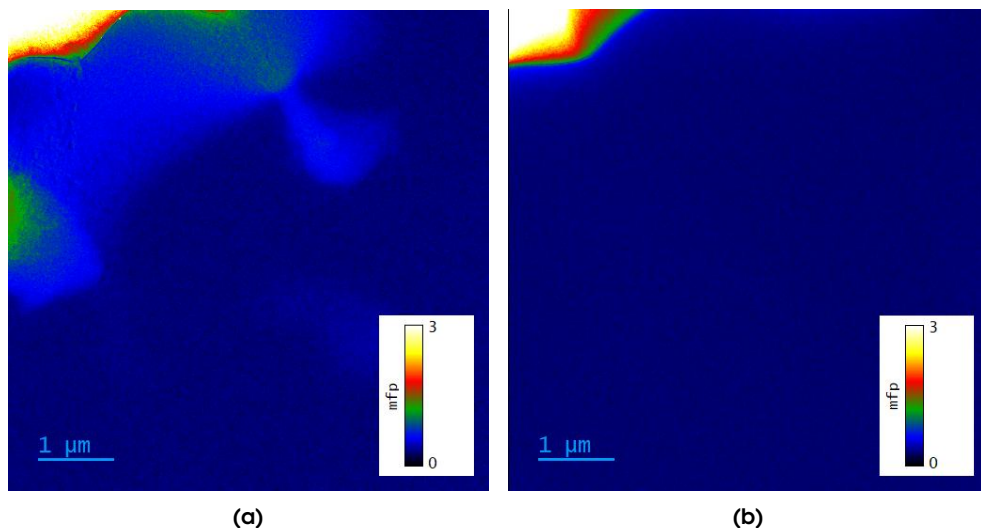


Figure 3.10. (a) t/λ map close to the edge of a cavity on chip cut from wafer. (b) t/λ map on another chip from the same wafer after additional etching with the isotropic silicon etch. Images acquired together with Anton Simon Bjørnlund.

nanoparticles. If nanoparticles are deposited mostly parallel to the surface normal of the ATOMICAR-devices, all nanoparticles landing in cavities will be visible in the TEM, except for those landing on cavity side walls. It is crucial that all nanoparticles landing in cavities are visible; otherwise, it is impossible to distinguish between a cavity with a very active nanoparticle or one with several catalytically active particles.

To achieve a directional deposition, nanoparticles have been deposited with a cluster source from Birmingham Instruments Inc. operated by Karl Krøjer Toudahl, Julius Lucas Needham and Rikke Plougmann ([105]). In this device, nanoparticles are, simply put, synthesized in a plasma and directed towards the sample with electric fields through apertures, and in this way the deposition of the nanoparticles becomes directional. Such a procedure distributes nanoparticles all over the cavities and on the front surface of the device. A mask is needed to exclusively deposit nanoparticles at the center of the electron transparent membrane, and limit the total number of nanoparticles deposited in the cavity to possibly enable single nanoparticle deposition. In the following section, it is proven that single particle deposition is possible.

3.3 Isolated single nanoparticles

The ideal mask is a hard mask that can be aligned with an ATOMICAR-device, and removed after a few nanoparticles have been deposited into each cavity. In the ATOMICAR group, the development of such a mask is ongoing work, but knowledge can be obtained from a preliminary approach that was developed in the ATOMICAR group. Based on an idea from Peter Christian Kjærgaard Vesborg, the PhD-students Tobias Georg Bonczyk, Anton Simon Bjørnlund and this author etched circular apertures in FLG-sheets covering electron transparent cavities on a previous version of the ATOMICAR design (the main difference being that the cavity bottom is made of PECVD SiO₂). Subsequently, nanoparticles were deposited through the etched apertures, and then the FLG-sheet was peeled off with Scotch tape®. In general, none to a few nanoparticles can be deposited per cavity in this way, if the aperture sizes are adjusted to the nanoparticle current and exposure time of the cluster source.

To etch the FLG, $\propto 10$ mbar of O₂ was introduced into the E-cell of the TEM, and the beam was focused to a circle approximately $\propto 1.5 \mu\text{m}$ in diameter. It has been reported in literature that electron beam ablation can be used to sculpture FLG in a TEM ([106]), but in our experiments, the FLG EELS signal seemed to stabilize after a period of electron beam irradiation with the microscope settings used. Inspired by studies of gas-assisted electron beam etching of suspended FLG-sheets with water vapor in a SEM [107], oxygen was introduced in the E-cell of the TEM to enhance the etch rate. This procedure proved successful. With gun lens setting 5, spot size 3, an extraction voltage of 4500 V, and a high tension of 300 kV, the FLG was continuously etched. During the etch, the FLG signal was tracked with EELS, and in this way, it could be determined, when all of the FLG had been burned away. An example of an etched FLG-aperture is shown in Figure 3.11 after nanoparticles have been

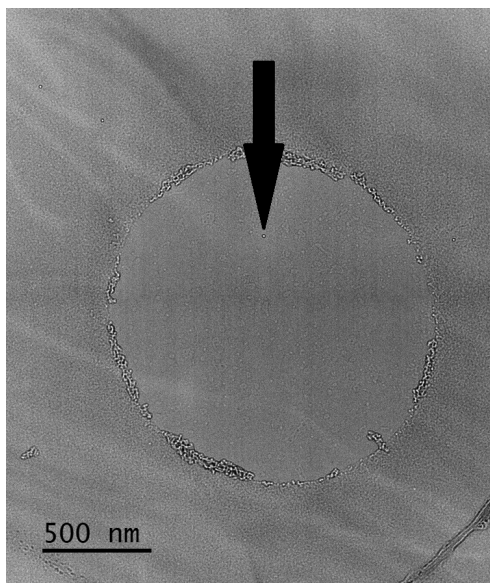


Figure 3.11. Defocused image of nanoparticles deposited on a FLG-sheet with a hole and suspended across a cavity. A single particle made it through the FLG-aperture of this cavity, and its location is indicated by a black arrow. Image acquired with Tobias Georg Bonczyk and Anton Simon Bjørnlund

deposited. The image is acquired out of focus to make the nanoparticles visible at low magnifications. A single platinum nanoparticle is deposited through the FLG-aperture and is highlighted with an arrow. There are other nanoparticles visible in the image, but they are lying on top of the FLG-sheet.

The etch of the FLG-sheet only takes a few minutes per cavity, and any type of FLG can be used in this procedure. After the FLG-sheet with the aperture has been peeled off, it would though require a lot of luck, if the cavities with a few nanoparticles are to be re-sealed by mechanical exfoliation of FLG. Instead, the FLG can be transferred to the device by a CAB transfer, as described in Section 2.4.

This intermittent method for isolating single nanoparticles is relatively easy to employ, however it has the obvious drawback that the ATOMICAR-device is heated during re-sealing of cavities with nanoparticles. This is problematic, if the cavities are to be sealed in an atmosphere with reactants for a catalytic process. However, if reactants are loaded subsequently exploiting the finite leak rates, the problem is circumvented. It is, however, important to note that larger molecules could have impractically low leak rates. Otherwise, another solution is to work with reactions that do not start at 60°C. Mechanical exfoliation of FLG is preferred in the group, as the experience is that it is possible to achieve the lowest leak rates with this method.

3.4 Monitoring the internal pressure with EELS

EELS and TEM have been used throughout the PhD-project to examine the different versions of the ATOMICAR-design, but whenever the design is altered, these characterizations become less relevant. Instead of reporting on older versions of the ATOMICAR-design, this section seeks to present, how EELS can be used to measure on captured gasses directly. The electron transparency of the cavities makes it possible to investigate the change in partial pressure of gasses captured inside sealed cavities. This section demonstrates this, and reports how this type of EELS measurements can be conducted. The fact that different atomic species gives distinct EELS signals is exemplified in Figure 3.12a. The figure presents an EELS spectrum (obtained approximately a day after inserting the sample in the TEM) containing signal from nitrogen ([108]) captured in the cavity, as well as the signal stemming from the FLG-membrane ([109]) and the oxygen in the cavity bottom. Beam electrons that scatter on K-shell electrons of carbon, nitrogen and oxygen suffer an energy loss of at least (approximately) 284 eV, 402 eV, and 532 eV, respectively ([52]). In this spectrum, the oxygen peak is aligned with an energy-loss of 532 eV to compensate for energy drift of the GIF, and therefore the onset of the element specific signal appear slightly shifted. The spectrum was acquired through an electron transparent cavity in an earlier version of the ATOMICAR-design sealed with mechanically exfoliated FLG. This version had TEOS-derived SiO₂ cavity bottoms about 100 nm in thickness, and the strengthening silicon was deposited in a poly-crystalline form. Figure 3.12a also presents the background-corrected data of the raw data, alongside background-corrected data from a spectrum obtained after more than an hour of continuous beam irradiation (dose rate measured on fluorescent screen of the TEM to be approximately 300 electrons/Å² s). MATLAB was used to fit a power-law functions in 30 eV wide windows in front of the elemental-specific signal in order to model the background below the elemental specific signal.

During this experiment, EELS spectra were acquired to track the nitrogen signal. The signal remained constant until it dropped abruptly, and the nitrogen signal vanished completely (see draft in appendix). The extensive electron beam illumination appear to damage the FLG, as can be seen from the decreasing carbon signal in Figure 3.12a, and the beaming might have established a leak pathway for the nitrogen molecules. This observation verify the interpretation that the nitrogen signal stems from a gas. The sample was sealed by mechanical exfoliation in ambient air, and so it was expected that nitrogen gas would be present in the cavities.

Instead of destroying the sample in order to verify that the nitrogen signal is from N₂ gas, another method can be employed. The nitrogen signal can be compared to reference spectra of nitrogen gas in the E-cell of the TEM collected through a hole in the sample. In Figure 3.12b, the nitrogen signal from captured nitrogen is compared to a reference spectrum of 1 mbar nitrogen in the E-cell. The similarity is striking, and in most cases, the comparison with a reference spectrum is used to interpret EELS data. Samples with argon captured in cavities have also been examined (see

draft in appendix). These samples were filled with argon by storing them in an argon atmosphere.

It is clear from Figure 3.12 that the gas signal is quite low compared to the background signal. As a result, the quantified nitrogen signal is sensitive to relatively small fluctuations in the background signal. The density of gasses is much smaller than that of solid materials, and this is the cause of the diminishing nitrogen signal. If the cavities were more shallow, the signal would be even smaller, as the projected gas density would decrease accordingly. As a result, the depth of the cavities cannot be too small, if the change in the partial pressure of captured gasses is to be tracked with EELS. Most of the background signal of the nitrogen peak stems from scattering on the cavity bottom and FLG-seal. Therefore, a thinner seal and cavity bottom will improve the nitrogen to background signal. However, after the sample has been made, these thicknesses cannot be changed. To maximize the signal, it can be exploited that most of the inelastic signal is mainly scattered to small angles. Since, the probability of scattering on plasmons is much higher than scattering on core-electrons, more signal from plasmon scattering can be found at higher scattering angles than e.g. that of core-loss scattering on N_2 . By operating the microscope in diffraction mode and using the entrance aperture of GIF to stop electrons scattered above a certain angle from travelling into the GIF, the ratio between the nitrogen signal and the

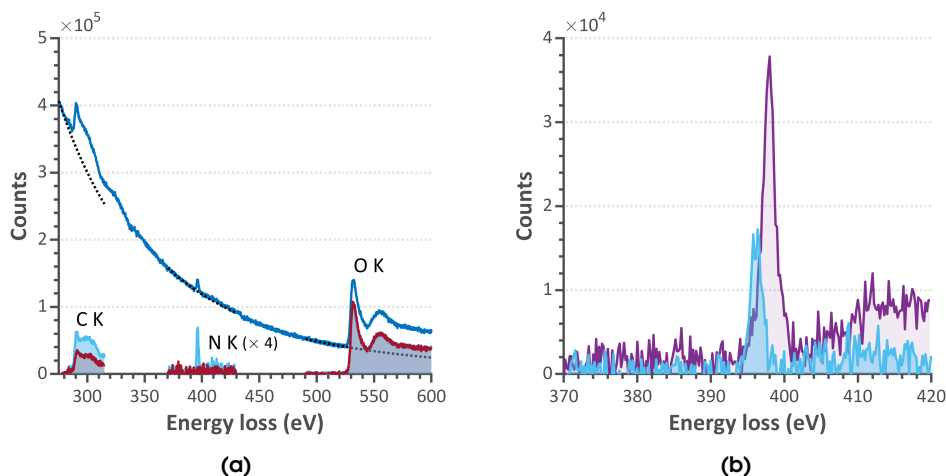


Figure 3.12. (a) Raw EELS data (dark blue) acquired prior to more than an hour of continuous electron beam irradiation. Fits to the background in front of the elemental specific peaks are shown with a black dotted line. The background-corrected data from before and after the extensive electron illumination is plotted in light blue and red, respectively. The approximate position of the carbon (C K), nitrogen (N K) and oxygen (O K) signal is indicated. Note that the background-corrected nitrogen signal is scaled by four. (b) Background corrected nitrogen signal (purple) plotted alongside raw signal of nitrogen gas (light blue) in the E-cell of the TEM. Both figures from draft included in appendix.

background can be maximized. Furthermore, the total current of electrons entering the GIF can be increased using the condenser system of the TEM to increase the current of electrons with all kinds of energy losses. Alternatively, the exposure time of the electron detector of the GIF can be increased. The former solution will increase the total electron beam current to the point that low-loss spectra cannot be obtained without saturation of the electron detector, and the latter solution can result in long exposures, during which the sample can drift.

When the change in partial pressure of a captured gas is to be determined with EELS, the signal has to be calibrated with the low-loss spectrum (or something proportional to it). Depending on the sample thickness and crystallinity, the probability of obtaining signal from a specific element can vary in magnitude (depending on acquisition parameters), but also the distribution as a function of energy-loss can change. To account for this, low-loss spectra should also be acquired. By scaling the summed core-loss EELS signal according to the low loss signal summed over an equally wide range of energy losses ([51]), the signal obtained is approximately proportional to the projected density of gas molecules. Only singly scattered signal is proportional to the density, but for thin samples, the error of summing core-loss scattering that have suffered additional scattering (like plasmon scattering), can be partly compensated for by calibrating with low-loss signal as just described ([51]). To acquire both low-loss and core-loss signal great care must be taken.

Low-loss and core-loss signal counts differ by many orders of magnitude. Consequently, it is for many microscope settings impossible to obtain the two without saturating the electron detector, when collecting low-loss electrons, or in the other extreme, nearly have no counts of core-loss electrons. If the settings of the TEM are changed in between the collection of low-loss and core-loss electrons, the two types of electron signals are not directly comparable. For example, a changed of spot size or current limiting aperture will change the C2-lens setting, which corresponds to parallel illumination. Consequently, the area illuminated on the sample has to be changed to obtain parallel illumination. The influence of different current changing operations could be characterized and compensated for, but Anton Simon Bjørnlund and this author decided instead to keep the settings of the TEM constant and instead changing the magnification of the energy-dispersed signal on the electron detector of the GIF.

Using spot size 6, gun lens 3, an extraction voltage of 3950 V, a 50 μm C2-aperture, 300 kV, and a dispersion of 0.03 eV/pixel for low-loss electrons and 0.2 eV/pixel for core-loss electrons, both types of signal could be obtained with exposure times of 0.001 s and 100 s, respectively. The nitrogen signal was optimal with a camera length of 195 mm and a 1 mm GIF-entrance aperture. The low-loss signal was collected as a sum of 100 exposures, and for the core loss 3 exposures were used. In order to ensure that the beam electrons are guided down the column of the TEM in the same way in each experiment, the diffraction lens is focused on the back-focal plane of the objective lens. In addition to this, the strength of the C2 lens is changed until the diffraction pattern is sharp - i.e. illumination of the sample is truly parallel.

As a proof of concept, a cavity on an ATOMICAR-device of the most recent

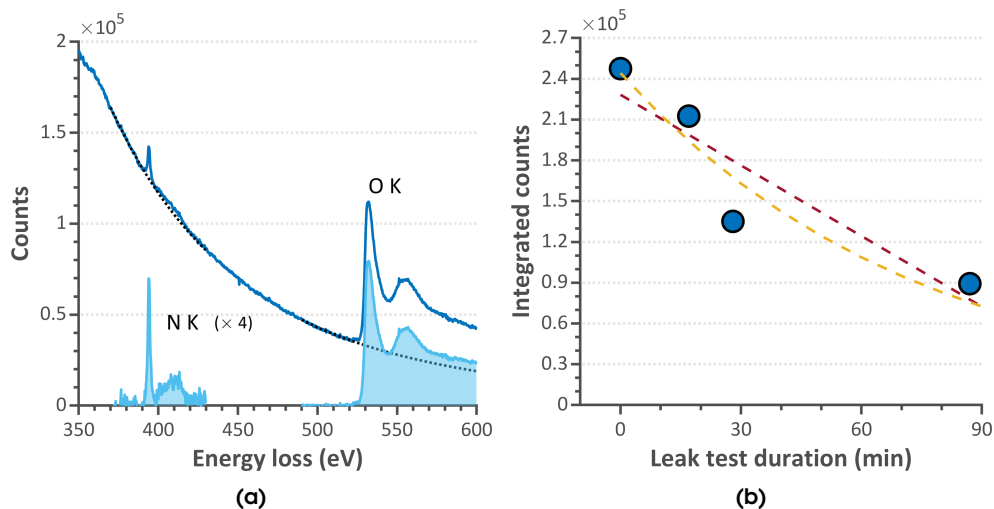


Figure 3.13. (a) Raw EELS and background corrected data from studies of nitrogen (N K) and oxygen (O K) signal in a cavity on a device of the most recent design. (b) Background corrected nitrogen signal summed 10 eV before and after center of nitrogen peak. Linear and exponential fit included. Data acquired with Anton Simon Bjørnlund.

design was investigated in this way after mechanical exfoliated FLG was used to seal the cavity in ambient air. A typical raw spectrum and the background corrected data is shown on Figure 3.13, alongside the nitrogen signal summed 10 eV before and after the nitrogen peak (found with a gaussian fit) for the four measurements of the experiment. Traditionally, core-loss signal is integrated from the point of steepest slope of the onset of the signal, but due to the shape of the nitrogen signal, this would disregard much of the signal. To correct for the background signal, a power-law function is fitted to a 20 eV wide region in front of the nitrogen signal. The nitrogen signal might have been even higher just when the sample was inserted, but due to fine-tuning of microscope parameters, and the study of the adjacent cavity (which was contaminated), the signal was not tracked when at its maximum.

Low-loss spectra were acquired after each core-loss signal collection. The beam was moved between the third and fourth measurement, with the consequent movement of the diffraction pattern with respect to the entrance aperture of the GIF. By aligning the two again, the fourth measurement of cavity could be collected. It is important that similar data can be obtained when revisiting cavities otherwise results are not reproducible, and it is difficult to investigate several different cavities in one experiment. To test that the fourth sample point reproduces the same trend as seen for the first three points, the data was fitted with both a linear (red line) and an exponential function (yellow line). Fortunately, the fourth measurement follows the trend of the rest of the points. If the leak rate was truly linear, it does not matter that the leak rate is high even though measurements took about 5 min to acquire.

Conversely, if the leak rate is actually exponentially decreasing, the time averages overestimates the true value. According to literature the leak rates are exponential [87], and this is also what is to be expected, if the leakage is purely diffusion driven. Since, the root-mean-square-errors are 4.6×10^5 and 2×10^4 for the linear and exponential fit, respectively, the exponential fit is the best. However, it is also obvious that more measurements are needed to determine the leak rate of this specific cavity with greater accuracy. Compared to the signal, the root-mean-square-error is an order of magnitude lower for the exponential fit. The relative error of course depends on how much nitrogen is present in the cavity, but it is quite clear that the method can be used to determine leak rates, and even better estimates can probably be made, for samples with lower leak rates. With a sample with a low leak rate, the relation between the magnitude of the nitrogen signal and the absolute partial pressure of nitrogen can be calibrated. Knowledge about absolute partial pressure would make it possible to compare the signal from different gasses, making the value of EELS measurements even higher.

Another important effect, discovered during the EELS measurements, is that the oxygen peak cannot always be used as a reference peak. During the leak test presented above, the oxygen signal increased, the general height of the background increased, and t/λ increased from 0.24 to 0.27 (data treatment with DigitalMicrograph®). This indicates that an oxygen containing contaminant is deposited during the measurements, and as a result, it is crucial that the low-loss spectrum is used for calibrations rather than the oxygen peak. This problem have been observed on other samples as well. In addition to this, other contaminants have EELS signals in the energy-loss region of N_2 , making it difficult to accurately determine the N_2 signal. An example of this can be found in Figure 3.14, where the raw data and background corrected data from the first and last measurement of a cavity is presented. Note that in between the first and last measurement nothing was done except acquiring spectra (and the microscope setting is the same for the two studied cavities). Both the increased oxygen signal and a nitrogen signal shape which is not equivalent to that of Figure 3.12b is seen on this figure. Hence, it is important to find a way of keeping the samples clean from contamination. The TEM is equipped with a cryo-pump, and this can be utilized to lower the pressure surrounding the samples in the TEM. However, this have not solved the problem completely for all measurements. Low-loss calibrations makes the problem of the changing oxygen-peak less severe, but areas with other nitrogen species than N_2 cannot easily be investigated. Further investigations of this phenomenon is needed.

Tobias Georg Bonczyk and Anton Simon Bjørnlund have recently used EELS to examine the leak rates of sealed cavities at elevated temperatures. A heating holder from Gatan was used to heat an ATOMICAR-device to 500°C while tracking the nitrogen EELS signal. This is a significant development for the ATOMICAR-group, as the experiment indicated that measurements can be conducted at industrial relevant temperatures. In these experiments, the entire heating holder was heated, and thermal drift prevented tracking of individual cavities during heating. In this way, thermal drift makes it impossible to study nanoparticles right after catalysis is

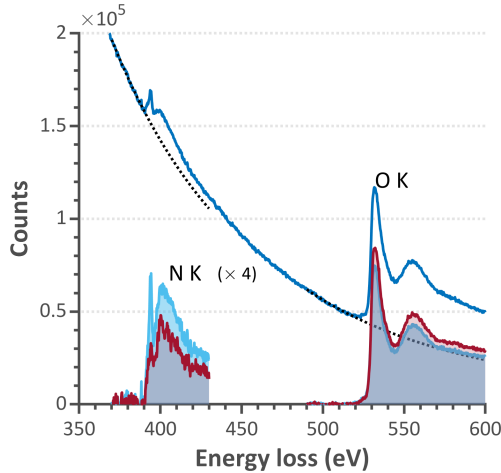


Figure 3.14. Raw data (blue) from first measurement and background corrected data from first (light blue) and last (red) measurement on cavity adjacent to that studied in Figure 3.13. Data acquired with Anton Simon Bjørnlund.

initiated. The following section describes efforts to solve this problem.

3.5 Ongoing work

This section presents ideas for the further refinement of the ATOMICAR-design. It is not the aim to discuss the different ideas in detail, but to sketch the potential of them.

All of the designs that have been developed during the PhD-project of this author used the full thickness of the free-standing slab as the cavity depth. It would be ideal, if the slab thickness and cavity depth could be decoupled, as this would allow for optimization of the cavity geometry while the free-standing slabs could be widened to increase the density of cavities. However, it is difficult to imagine how such a situation can be achieved, if only etching from the front side of the ATOMICAR-devices are considered. The material left as the cavity bottom will, in the present design, also be the thickness of the electron transparent region of the device. Hence, the etch of the cavities need to extent nearly all the way through the freestanding slab, in order to obtain sufficiently thin electron transparent bottoms. Etches from the backside could solve this issue, and experiments should be conducted to investigate, if it is possible to thin down parts of the freestanding slabs from the backside. This approach have not yet been explored in the ATOMICAR-group. In the case that the free standing slabs are to be thinned down from the backside, resist should be spray-coated rather than spin coated ([62]). Otherwise, the structures already etched from the backside will be filled with resist (see section 3.2.2). In photo-lithography, the resolution, with

which structures can be defined in a resist, depends on the distance between laser and resist. For instance, if a hard mask is used to pattern the resist, the square of the resolution (defined from the minimal resolvable linewidth) that can be obtained using photo-lithography depends approximately linearly on the distance between the mask used to pattern the resist and the resist ([62]). Neglecting the effect of the resist thickness, a 365 nm laser would theoretically have a resolution on the order of 11 μm on the backside of the freestanding slabs in the present design. As a consequence, the minimal area that can be thinned down from the backside of the free-standing slabs is quite large.

An alternative approach that this author have investigated is to utilize that silicon expands when oxidized. By only etching the front side oxide in the fourth step of the protocol, the strengthening silicon layer will be exposed to the environment both on the backside of the slabs and at the bottom of the cavities. If the silicon is then oxidized, the front of the silicon oxidation progressing from the bottom of the cavities etched on thermal SiO_2 will reach that of the oxidation from the backside of the slab before the whole of the strengthening silicon is oxidized. This process will leave the bottom of the cavities elevated, as compared to before the oxidation. If the front side is coated with silicon nitride, the SiO_2 beneath the nitride can be removed from the backside with HF to create an electron transparent silicon nitride bottom lifted above the bottom of the free-standing slab. A proof of concept of this approach has not yet been achieved, but preliminary tests show that the two oxidations fronts move as speculated. A cross section of a freestanding slab with a strengthening silicon layer oxidized both through cavities in the front side and from the backside is shown in Figure 3.15a. The slab consists of several layers including a silicon nitride layer passivating against oxidation from the front side in regions outside the cavity, but for the purpose of testing the design idea, only the oval-shaped SiO_2 structure at the bottom of the cavity and the oxide layer on the backside of the slab is important. A longer oxidation would make these two fronts connect, and possibly elevated nitride bottoms could be achieved.

A major weakness of the present design is that there is no integrated heater structure. Consequently, the whole device has to be heated, if experiments are to be conducted at elevated temperatures. This creates issues such as thermal drift. Furthermore, the narrow opening through the chips limits the scattering angles that can be investigated in the TEM. To avoid this problem, commercially available devices developed for *in situ* studies of catalysis places the catalysts on/in large thin membranes, which can be heated by joule heating [40][41][110][42]. The minute amount of material can be heated fast with small amounts of energy, and the relative long distance from heated region to bulk chip combined with the geometrical expansion from membrane to bulk chip ensures that the rest of the chip is basically in thermal equilibrium with the environment - even though the region with catalysts is heated.

By implementing a dip in a solution with KOH after step 2 in the protocol, most of the material in between the freestanding-slabs can be removed. On Figure 3.15b, an example of the effect of such a dip on ATOMICAR-structures is shown. Since, the etch rate of thermal SiO_2 by a KOH solution is lower than that of silicon, the

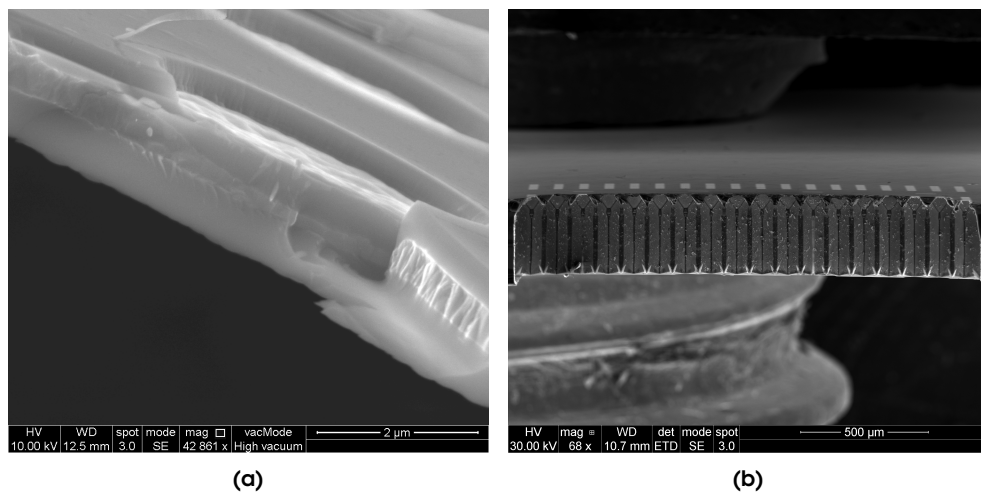


Figure 3.15. (a) Cross section of free-standing slab with a silicon layer oxidized both through cavities on the front side and from the backside. At the top of the slab is a SiO₂ layer, beneath that is a strengthening silicon layer. After cavities have been etched into the SiO₂ on the front side of the wafer, it is again oxidized in a furnace, and the profile of the oxidized silicon can be seen to progress both from the backside of the slab (lowest lying layer) and through the cavity (oval structure). (b) Cross section of sample after a dip in KOH solution. Note the triangular beams sustaining the front side. Unbroken freestanding slabs appear bright and rectangular.

slabs are largely left unetched. The etch rate of silicon varies between crystal facets ([62]), and as a result, triangular beams are left between the free-standing slabs after a KOH-etch. Using this method, it has been possible to remove most of the material beneath 2×2 mm² areas, while the triangular beams still support the membranes. During the KOH-etch, the front side can be protected by a thin PECVD silicon nitride layer on LPCVD silicon - both of which can be removed after the KOH-etch. The test structure shown in Figure 3.15b can still withstand mechanical exfoliation. Utilizing this method, heater structures defined on the center of a structure similar to that presented in Figure 3.15b could potentially heat ATOMICAR-devices, while the bulk chip is still at room temperature. On-chip heating would be very beneficial for ATOMICAR's efforts of measuring catalysis *in situ*, and it should be implemented in future versions of the ATOMICAR-design.

CHAPTER 4

Discussion & Conclusion

Prioritizations and choices made in the design of the present ATOMICAR-design have been discussed as the design has been presented in this thesis. Possible refinements of the design have already been elaborated on in the previous chapter, and therefore this brief chapter is dedicated to discussions of the methods employed in more general terms.

AM-AFM relies on the assumption that the interaction between cantilever and sample stays constant throughout the scan of the sample surface. However, as discussed in Sections 2.2 and 3.1.1, the assumption is not always justified, and in this case, great care must be taken to calibrate the measurements. Other types of AFM could have been employed to circumvent this issue, e.g. "Contact Mode AFM" (CM-AFM ([56])). Topographic information is obtained in CM-AFM by using the tip-sample force as the set-point parameter: The deflection of the AFM cantilever is kept constant, as the tip is dragged across the surface, and in this way, the interaction force between sample and cantilever is the same throughout the scan. Unfortunately, constant contact can result in sample damage, as the cantilever tip applies a force in the direction of the scan on the sample. This is not a preferable situation, if very thin graphene sheets are to be imaged.

Peak force tapping AFM ([111]) combines the strength of AM-AFM and CM-AFM. In this AFM technique, the cantilever is oscillated, while the tip-sample interaction force is monitored. Exploiting this setup, the peak tip-sample force can be controlled, while the oscillating cantilever is scanning the sample without applying a lateral force to it. A number of artifacts of AM-AFM scans discussed in this thesis could be avoided with this technique, however it requires specialized equipment to conduct Peak force tapping AFM. While this would ease the use of the AFM, it doesn't change the general characteristics of the AFM: high spatial resolution, but slow image acquisition speed. Additionally, AM-AFM can without doubt be used to track, the internal pressure of sealed cavities, and therefore, a more refined AFM technique might not drastically improve measurements of the shape of the FLG seals.

There exist other methods, which can be used to probe the tension in a suspended membrane. Bunch et al. ([112]) used optical methods to excite and detect oscillations in suspended graphene-sheets at their resonance frequency. Since the resonance

frequency of a membrane depends on its tension, this type of measurements can be used to determine the pressure difference across a sealing graphene-membrane ([73]). In the ATOMICAR group, the PhD-student Yanxin Liu has demonstrated that the resonance frequency of a cavity can be determined within one second with good accuracy, and therefore this type of optical measurements can be used complementary to AFM measurements, and to investigate many more cavities than is possible with an AFM. However, real space images still provide valuable information about FLG sheet shape, and they should be used to investigate whether optimal measurements change experimental conditions (the laser could heat the sample).

Mechanical exfoliation is preferred by the ATOMICAR-group, however this graphene transfer method is most efficient, if samples are cleaned in an oxygen plasma prior to graphene transfer. In the case that single nanoparticles have been isolated in each cavity, such a treatment could potentially oxidize the nanoparticles and alter their properties. The transfer yield of mechanical exfoliation has not been rigorously investigated as a function of time passed since plasma cleaning, but preliminary experiments indicate that samples do not need to be sealed directly after plasma cleaning. If samples were plasma cleaned in the vacuum of the used cluster source, before nanoparticles are deposited, and sealed immediately after the sample is removed from the cluster source, oxidation of the nanoparticles might be avoided.

When the thickness of the electron transparent bottoms is eventually made thinner, two issues may arise. First of all, thickness variations in the sealing FLG sheet may lead to large variations in t/λ from cavity to cavity, hence it becomes increasingly important that the acquired EELS spectra do not exclusively contain single-scatter signal. As long as low-loss spectra are acquired, fourier-ratio deconvolution can be used to account for this. Using fourier-ratio deconvolution, the single-scattered core-loss spectrum can be recovered from the acquired EELS spectra, and in this way, thickness variations will not affect the measurements. Whenever such a procedure is employed, it is important to ensure that the dispersion (in terms of $eV/pixel$) is calibrated for both low-loss and core-loss spectra. This type of calibration can be carried out with a sample of boron nitride and hydrogen in the E-cell of the TEM. Secondly, the thinner the cavity bottoms are, the larger the leak through them will be. Consequently, the optimal cavity bottom thickness might not be as thin, as if only electron transparency was prioritized.

Relevant TOFs are comparable in size to the leak rates reported by Bunch et al. ([73]). As a result, measurements of the internal pressure of cavities should be accurate, when the catalytic activity of single nanoparticles are to be investigated. In addition, cavity-to-cavity variations in the leak rate ([87]) will obscure qualitative comparisons of the evolution in the internal pressure of sealed cavities. Future work should aim to reduce the leak rates, as this will solve the problems listed in this paragraph.

Finally, it should be mentioned that during the period that this thesis has been written, the ATOMICAR-group have initiated work aimed at performing catalysis in the cavities of the present ATOMICAR-device.

In this thesis, the design of a novel tool has been presented, and it has been argued that it can facilitate studies of single particle catalysis. The device consists of arrays of micron sized electron transparent cavities in which a single to a few nanoparticles can be isolated from the environment by seals of few-layer-graphene (FLG). It has been demonstrated that the total internal pressure of these miniature cavities can be monitored via AFM measurements of the shape of the sealing membrane. Moreover, it is shown that the partial pressure of gasses kept in sealed cavities can be tracked with electron energy loss spectroscopy through the electron transparent cavity bottoms. Exploiting these two methods for probing the internal pressure of sealed cavities, pressure changing chemical reactions catalyzed by single nanoparticles can potentially be investigated with this new tool. In addition, a method for isolating single nanoparticles in the cavities has been invented. In this way, a platform for investigations of single particle catalysis has been developed, and it is the hope that the device can aid the search for new catalysts to the benefit of society.

Appendix

Record-low leak rates of graphite-sealed SiO₂

cavities

Hjalte Rørbech¹, Zhongli Wang¹, Yan-Xin Liu¹, Tobias G. Bonczyk¹, Edwin Dollekamp¹, Lau M. Kaas¹, Sofie Colding-Jørgensen^{2,3}, Anton S. Bjørnlund², Kristian S. Mølhave³, Stig Helveg², Peter C. K. Vesborg^{1,2}*

¹Surface Physics and Catalysis (SURFCAT), Department of Physics, Technical University of Denmark, DK-2800 Kgs. Lyngby, Denmark

²Center for Visualizing Catalytic Processes (VISION), Department of Physics, Technical University of Denmark, DK-2800 Kgs. Lyngby, Denmark

³National Centre for Nano Fabrication and Characterization (Nanolab), Technical University of Denmark, DK-2800 Kgs. Lyngby, Denmark

KEYWORDS: Membranes, Two-dimensional materials, Graphite-sealed, Cavities, Graphene, TEM, EELS

ABSTRACT. The remarkable ability of graphene to seal silicon-fabricated substrates has been utilized in numerous devices such as pressure sensors, molecular valves, and electron-transparent liquid reactors. However, graphene-sealed devices in general exhibit leak rates preventing them from reaching their full potential. In this study, we sealed a cavity etched in SiO₂ with mechanically

exfoliated graphite, and using an atomic force microscope to track the membrane deflection, we show that it is possible to achieve leak rates down to ~ 121 molecules/s for ambient air. This is three times lower than previously reported leak rates of similar structures. To provide independent evidence for this unexpected behavior, we fabricated electron-transparent cavities and verified the slow leak of ambient nitrogen directly using electron energy loss spectroscopy. Our results suggest that the performance of graphite/graphene-sealed devices can be improved further, and thus their application could be expanded.

TEXT. Today, it is well-established that graphene is impermeable to all gases [1-7], besides, perhaps, hydrogen [5]. This phenomenon was first described in pioneering work by Bunch et al. (2008) [2]. Since then, several fields of science have exploited this trait of graphene [8]. For example, devices that can selectively sieve molecules [6], devices with molecular valves [1], pressure sensors [9-12], and electron-transparent liquid cells have been developed based on this property of graphene [13-18].

In 2008, Bunch et al. [2] presented the pioneering study of gas diffusion in and out of cavities made in SiO₂ and sealed with mechanically exfoliated graphene. In their study, the pressure and species of the gas contained in the cavities were changed in a pressure chamber. This was achieved by letting the cavities equilibrate with the atmosphere of the chamber – either filled with a loading gas or pumped to vacuum. Using laser interferometry, Bunch et al. [2] tracked the resonance frequency of the graphene-membranes suspended across the sealed cavities, while the ambient pressure was changed. From these measurements, they estimated leak rates, which did not depend on the number of graphene layers sealing the cavities. Therefore, it was concluded that graphene

is impermeable to gasses. Recently, another study proved the impermeability of graphene with even lower experimental uncertainty in graphene-sealed graphite cavities [5].

In this work, we revisited SiO₂ as the cavity substrate and sealed plasma etched cavities with graphite. We detected a leak rate of ambient air, which is three times lower than what has hitherto been reported, by tracking the shape of a pressurized graphite-membrane with an atomic force microscope (AFM). Low leak rates are crucial for the utilization of the impermeability of graphene in any of the aforementioned technological applications (Pressure sensors, molecular valves, and electron-transparent liquid cells), and our finding suggests that the performance of such devices could be improved further.

The fact that the observed leak rate is exceptionally low raises the question, if the apparent slow outflow of molecules indeed is caused by a miniscule leak of ambient air or another phenomenon; especially as the examined structure is substantially similar to those described in literature [1-4, 6, 7]. We present a microchip containing cavities similar to those studied by Bunch et al. (2008) [2], but in an electron-beam transparent 3D layout, which, to our knowledge, for the first time permits direct Electron Energy Loss Spectroscopy (EELS) measurements on gasses captured with graphite. With this device, we observe cavities with a slow leakage of ambient nitrogen and validate our interpretation of our AFM investigations.

In the following, we first present a sample (referred to as Sample 1) cut from a wafer with cavities etched in thermal SiO₂. The cavities were sealed by mechanically exfoliating graphite on the sample in ambient air, and with this sample, we prove the existence of unusually leak-tight cavities. Secondly, we independently verify the existence of such cavities using an electron transparent sample (Sample 2) fabricated on another wafer. We use a third electron transparent

sample (Sample 3) from yet another wafer to demonstrate the capabilities of our electron transparent structures and motivate the applicability of the design.

After fabrication and sealing with mechanically exfoliated graphite (see Supplementary Information (SI)), we positioned Sample 1 under an AFM inside a chamber with controllable pressure. The chamber was pumped to a pressure below 6 mbar (limited by chamber leak rate), and the difference between the internal pressure of graphite-sealed cavities and the residual pressure of the AFM chamber caused the graphite membranes to bulge outwards. With the AFM, we tracked the maximal deflection of a graphite membrane sealing a cavity with a low leak rate. Figure 1a shows an optical image of the graphite flake on Sample 1 sealing the studied cavity (indicated with a red arrow). A representative background-removed (defined in the SI) AFM image of the cavity of interest is shown in Figure 1b. We defined the maximal deflection as the distance between the maximal Z-coordinate (median of 19 by 19 points in the central area) and a line 19 pixels wide between the lowest points in a cross section of the AFM image, as depicted in Figure 1c. Figure 1d shows the maximal deflection of the graphite sheet, covering the cavity, tracked at low pressure for 8 days. Due to a small, but evident, scatter in the measured maximal deflection, the measurements at minimal chamber pressure are fitted with a straight line to identify the total change in maximal deflection. The total change in deflection is -1.26 nm (95% confidence interval (CI95): -2.16 nm to -0.36 nm). This minute change, over the course of 8 days, suggests that the leak rate of the cavity is exceptionally small.

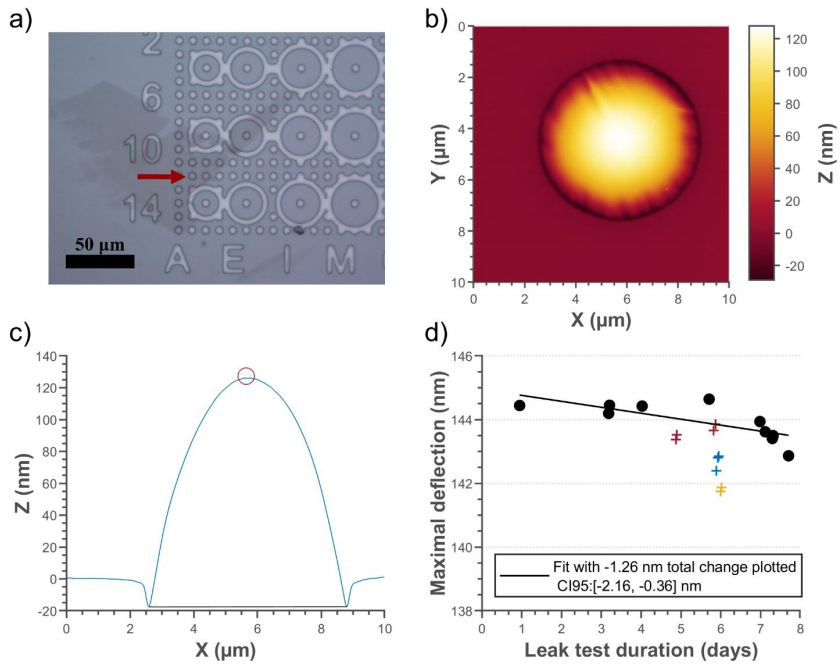


Figure 1. Leak test of a graphite-sealed cavity on Sample 1 with AFM in the pressure chamber. a) Optical image of Sample 1 with an arrow indicating the investigated cavity. b) Background-removed AFM image of the cavity with low leak rate. c) Average of 19 scan lines centered on the scan line with the maximal deflection. The red circle indicates the point of maximal deflection, and the black line is used to define zero deflection. d) Maximal outward deflection of the graphite membrane suspended over the leak-tight cavity at external pressures of 3-6 mbar (black circles). Measurements depicted as red, blue, or yellow crosses are from a pressure sweep introduced later. A linear fit to the black circles is plotted and the total deflection change of the fit is noted in the legend with 95 % confidence interval (CI95).

The leak rate of the cavity, causing a slow decrease in the membrane deflection, can be calculated by modelling the relationship between a pressure difference across a suspended graphite membrane and the membrane deflection [6]. For small changes in membrane deflection, the adequateness of the model depends on knowledge of the initial pressure inside the cavity, which is difficult to determine with accuracy for ambient air. However, we can leverage our ability to control the ambient pressure of the AFM to measure the derivative of the membrane deflection with respect to the pressure difference across the membrane, i.e., the sensitivity. Such variable-pressure tests were carried out during day 5 and 6 of the leak test, and the resulting membrane deflections determined with an AFM are marked with crosses on Figure 1d and Figure 2. Maximal deflections plotted as red, blue, and yellow crosses were obtained at a chamber pressure of approximately 50 mbar, 100 mbar, and 150 mbar, respectively. Since the duration of the pressure sweeps are small, compared to the whole leak test (see Figure 1d), it is assumed that these sweeps do not influence the leak tests significantly. In Figure 2, only the measurements from the pressure sweeps are included, and the maximal deflection is plotted against the chamber pressure. Using a linear fit, the change in maximal deflection per mbar change is determined to be -0.19 \AA/mbar (CI95: $[-0.23 \text{ \AA/mbar}, -0.15 \text{ \AA/mbar}]$).

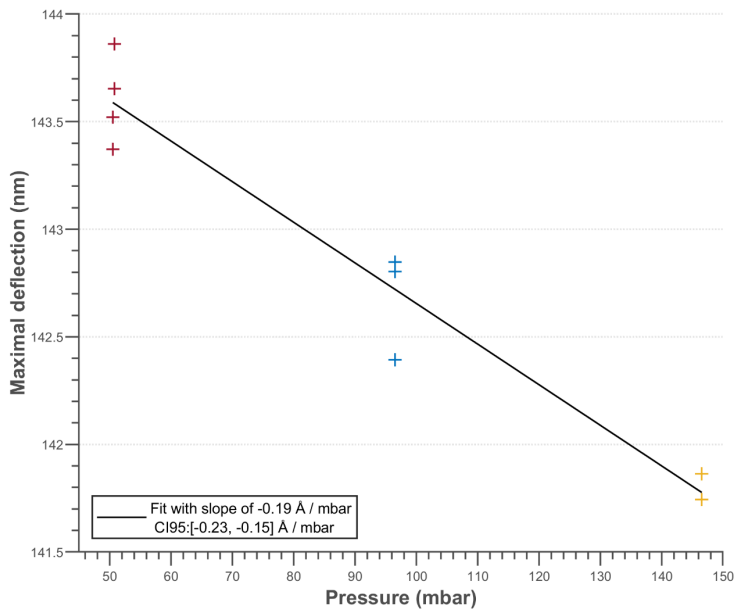


Figure 2. Sensitivity of studied graphite-sealed cavity on Sample 1 obtained with AFM inside the pressure chamber. The maximal deflection of the graphite membrane suspended over a cavity at 49.5-51.5 mbar (red crosses), 95.5-97.5 mbar (blue crosses) and 145.5-147.5 mbar (yellow crosses) is shown. A linear fit is plotted, and the total deflection change per mbar of the fit is noted in the legend.

Combining data from Figure 1d and Figure 2, the pressure change can be determined to be 66 mbar (CI95: [17 mbar, 115 mbar]) over the course of the leak test (confidence interval calculated using the error propagation law). Assuming a temperature of 293 K and using a cavity depth and

diameter of 1.3 μm and 6.5 μm , respectively, the time-averaged leak rate corresponds to 121 molecules/s (CI95: [31 molecules/s, 210 molecules/s]) (see SI). This record-low leak rate is surprising for a SiO_2 cavity sealed with graphite in ambient air, when no additional treatment has been carried out to further seal the cavity [3, 4]. Similar structures sealed by mechanical exfoliation have been reported to exhibit significantly higher leak rates; from approximately 300-2000 molecules/s (~ 300 only reported once) for ambient air or N_2 [2, 6]. As argued above, indirect measurements of the leak rate in principle leaves the leak rate of a specific gas undetermined. Using Sample 2, we address the need for a direct observation of the leakage of ambient air.

Information, about the species of the captive gas, is fundamentally inaccessible through measurements of the graphite-membranes deflection in structures such as that examined above. This motivated us to design and fabricate an electron-transparent sample, referred to as Sample 2 (see SI), on which gas captured with a graphite membrane can be investigated with EELS. We mimicked Sample 1, and structures studied in literature [1-4, 6, 7], by using thermally grown SiO_2 as the front side material in our design, and electron transparency was ensured by 100 nm thick SiO_2 cavity bottoms. Following the fabrication, graphite was mechanically exfoliated on Sample 2 using the same procedure as for Sample 1 (see SI). Although gas mixtures have been studied with EELS [19, 20], our electron transparent design is the first, to our knowledge, to facilitate direct EELS measurements on gas captured in SiO_2 cavities by a graphite-seal.

To investigate Sample 2, we used a FEI TITAN 80-300 ETEM (Environmental Transmission Electron Microscope) equipped with a differential pumping cell that allows the introduction of a few mbar of gas at the specimen plane [21]. We operated the microscope at a primary electron

energy of 300 keV in broad-beam image mode, keeping illumination conditions and the electron dose rate (approximately $300 \text{ e}/\text{\AA}^2/\text{s}$) constant from measurement to measurement. By choosing a beam diameter smaller than the studied cavities, we ensured that beam induced phenomena were limited to the studied cavity during measurements, and that adjacent cavities were minimally exposed. A post-column Gatan Image Filter (GIF) Tridiem 863 was used to acquire electron energy loss (EEL) spectra with an energy dispersion of approximately 0.2 eV/pixel and an energy resolution, defined as full-width half maximum of the zero loss peak, below 2 eV. Note that to remove energy drift of the GIF, the oxygen signal maximum was fitted with a Gaussian distribution and aligned with 532 eV in all EEL spectra obtained on cavities. This unfortunately also shifts the onset of the element specific EEL signal. The background EEL signal was modelled with a power-law function fitted to the spectrum regions preceding the elemental specific C K, N K and O K signal and finally removed from the ionization edge regions of the EEL spectra.

Figure 3a shows a raw EEL spectrum acquired on a cavity on Sample 2. After more than one hour of electron beam illumination of same graphite-sealed cavity, another spectrum was acquired. Both EEL spectra are plotted alongside each other on Figure 3a after background removal. The spectra clearly reveal the C K-, N K- and O K-ionization edges, and both the characteristic energy loss near edge structure of graphite [22], the gaseous fingerprint of N_2 [20], and the oxygen signal from the cavity bottoms can be identified.

Initially, a N K-edge signal was clearly seen at an energy loss of 401 eV, but after more than 1h of electron illumination, the C K-edge signal was significantly reduced, and the N K-edge signal had disappeared. The long-term electron illumination of the cavity therefore appears to have inflicted beam damage on the graphite seal with the consequent sudden disappearance of the nitrogen peak (when a leakage pathway was established). Furthermore, the N K-edge signal in

Figure 3a appears comparable in shape to that of a reference measurement of N₂ gas shown in Figure 3b. Note that the raw reference N₂ signal does not have an oxygen signal to align with. This is the cause of the shift in energy between the two spectra on Figure 3b. Unfortunately, the huge background signal in front of the O K EEL signal stemming from the electron transparent SiO₂ window masks the gaseous oxygen signal. Thus, these measurements unequivocal proof that the content of the cavity was air/nitrogen. Several other cavities were examined individually in the same way. In all investigated cases, the N K-edge signal disappeared after continuous electron illumination.

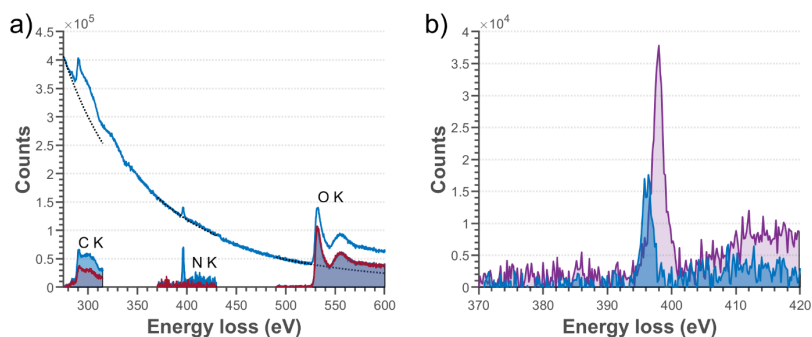


Figure 3. EELS data in the core-loss region including the C K (284 eV), N K (401 eV), and O K (532 eV) ionization edges. The spectra were acquired on TEM-transparent Sample 2. a) Energy-aligned EEL spectrum (blue) was collected by probing a sealed cavity a day after the sample was inserted in the vacuum of the microscope. In addition to the raw EEL spectrum (continuous spectrum), background fitting and extrapolation (stippled black lines), and background-corrected spectra at the three ionization edges are shown. After more than one hour of continuous electron illumination and data acquisition, the background-corrected EEL spectrum was obtained (red)

showing absence of nitrogen. The N K signal was magnified by a factor of four in this figure. b) Average of three raw nitrogen spectra (purple) acquired through a hole in the sample with 1 mbar nitrogen in the differentially pumped cell of the microscope. The N K edge from Figure 3a is superimposed for comparison.

The N K-edge signal is proportional to the number of nitrogen molecules in the cavities and can therefore be used to measure the leakage. Sample 2 was taken out of the microscope after two days and stored under vacuum ($< 10^{-1}$ mbar) for 17 days. Then, it was reinserted in the microscope to be examined using the same settings of microscope. The sample transfer through ambient took a short time. In order to quantify the N K signal, the nitrogen white line was fitted with a Gaussian, and the signal within three standard deviations of the center of the Gaussian fit was integrated. Low-loss spectra acquired directly before or after spectra containing the nitrogen signal were used to scale the integrated number of counts. During the initial part of the leak test, the content of nitrogen gas was verified for several cavities, as described above. The first measurements from these tests are plotted as black circles in Figure 4a for comparison. Representative data from one of these verifications are included in Figure 4b. The nitrogen content of three different graphite-covered cavities (red, yellow, and blue in Figure 4a) was measured several times during the leak test, and the integrated white-line of the nitrogen signal is shown in Figure 4a. Note that the scatter in the data of Figure 4a is similar for colored and black circles indicating that the scatter mainly is measurement related. Since the nitrogen signal is small, it is sensitive to fluctuations in the background signal. The data shown in Figure 4b illustrates how the nitrogen signal disappears suddenly during electron beam illumination, as described earlier. Besides establishing a leakage pathway, extensive beaming does not influence the measured nitrogen signal.

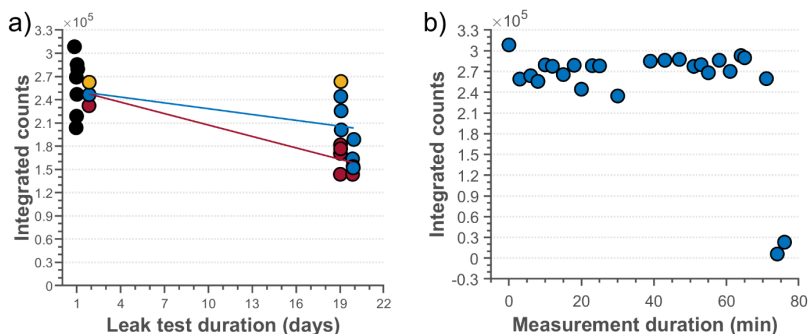


Figure 4. Leak test of Sample 2 based on EELS. a) The integrated background-corrected white-line N K edge signal for three different cavities (yellow, blue, and red) are plotted against the time under vacuum. Data from the first measurement on other cavities plotted as black circles for comparison. Linear fits to “blue” and “red” cavities colored blue and red, respectively. b) Representative integrated background-corrected white-line N K edge signal as function of measurement time.

We use Figure 4a to estimate the leak rate of two cavities. The beam punctured the “yellow” cavity after the second exposure. This cavity, however, appears to behave similarly to the blue cavity. Therefore, the “blue” and “yellow” cavities are examined as one. Since the cavity volume approximately is $130.2 \mu\text{m}^3$, the nitrogen signal did not differ a lot after two days in vacuum. However, after 19 days in vacuum, the difference became appreciable. From rough linear fits, the leak rates are estimated to 714 molecules/s and 368 molecules/s for the “red” and “blue” cavity, respectively (see SI “leak rate calculation”). As a consequence of the scatter in the data, both fits include the first measurements of the “red”, “blue”, and “yellow” cavity. The leak rate of the “blue”

cavity appears to be much lower than usually observed for SiO₂ cavities. The EELS measurement thus provides independent verification of the existence of SiO₂ cavities with low leak rates, and validates our interpretation of the AFM measurements.

Analysis of Figure 4 indicates that our design is useful and complementary to AFM studies, when measuring leak rates of ambient air. Now, we present a second electron transparent sample, Sample 3, in order to elaborate on the capabilities of our new design. So far, to our knowledge, mixtures of gasses captured with graphite-membranes have not been studied, as this is difficult through measurements of the graphite-membrane. However, with Sample 3, we obtain an EEL spectrum of a captured gas composed of both argon and nitrogen.

Conceptually, the design of Sample 3 and Sample 2 is the same, except that the electron transparent cavities are arranged differently on Sample 3 (see SI). After fabrication, a graphite flake was transferred to the sample using CAB (see SI). This sample exhibits higher leak rates than Sample 1 and 2 making it easier to exchange the captured gasses.

Sample 3 was stored in the pressure chamber, containing the AFM, for two days in 1 bar of ambient air and 0.8 bar of argon. Then, the sample was transported to the microscope used for investigations of Sample 2 to carry out EELS measurements on two graphite-sealed cavities. Figure 5a shows data from one of the cavities and reveals a clear Ar L_{2,3}- and N K-ionization edge indicating that Ar diffused into the cavity during its storage in the AFM chamber. An AFM overview of the graphite-covered area on Sample 3 is shown in Figure 5b. An arrow is used to indicate the cavity studied in Figure 5a. The EEL spectrum obtained on Sample 3 demonstrates that signals from several gas species captured in graphite-sealed membranes can be simultaneously investigated and compared in our design. This could be exploited to study the leak of gasses, while

simultaneously controlling the absolute pressure difference across graphite-membranes with another fast leaking gas. Such measurements could reveal whether the leakage of gasses depend on absolute or partial pressure differences [4]. Such investigations, however, are beyond the scope of this study.

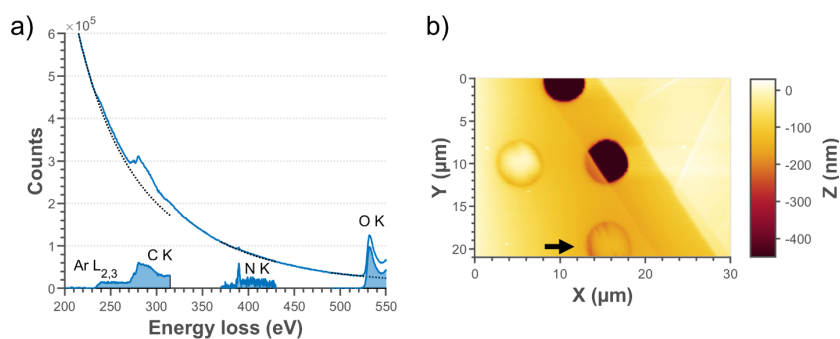


Figure 5. Perspectives of TEM-transparent design demonstrated with Sample 3. a) Background corrected EELS signal of Ar L_{2,3} (245 eV), C K (284 eV), N K (401 eV), and O K (532 eV) ionization edges. The N K signal is magnified by a factor of ten. b) AFM overview of graphite-covered area obtained at approximately zero mbar in the pressure chamber. The EELS data, presented to the right, is from the cavity indicated by an arrow.

In this study, we observed low leak rates on the wafer thick Sample 1 as well as on the TEM-transparent Sample 2 with 100 nm thick SiO₂ bottoms. This suggests that the distance to ambient through SiO₂ is not of great importance. Thus, our results are consistent with those of Lee et al. (2019) [3] and Manzanares-Negro et al. (2020) [4]. These studies successfully reduced the leak rates by plugging the graphene membrane edge with e-beam deposited SiO₂ [3], or by using an

AFM diamond tip to press the graphene sheet closer to the substrate [4]. Together, these findings and our data motivate the hypothesis that the mechanism, governing the leak rate, acts at the interface between the substrate and graphene. The nature of the leak mechanism is still, on a physical level, undetermined, and therefore the leak rates cannot be controlled and engineered. In our experience, both graphene transfer yield and leak tightness of the sealed cavities heavily depend on when the samples were plasma cleaned during the process. Furthermore, low SiO₂ surface roughness is also of great importance. Both of these observations support the hypothesis that the interface between graphite and substrate determines the leak rates, but there is a need for a rigorous statistical investigation.

To our knowledge, no one has yet achieved as low leak rates as we report in graphite/SiO₂ structures without additional treatment of the graphite-seal after transfer. This could be due to the fact that leak tests must be very long or carried out under non-ambient pressure with an AFM or with EELS in order to distinguish between very leak-tight and very fast leaking cavities.

In this study, we have presented data that proves the existence of sealed graphite/SiO₂ cavities with record-low leak rates. TEM investigations of cavities sealed with mechanically exfoliated graphite supported leak tests carried out with an AFM. Our TEM transparent design facilitated direct measurements of captive gasses, and we anticipate that the novel TEM-transparent design will bring new knowledge to the research field of 2D materials. The advantages of controlling and obtaining the minimal leak rate are obvious: Pressure sensors based on truly leak-tight graphite seals would be free of hysteresis/memory and molecular sieving will be even more selective. Our work shows that the leak rates can potentially be optimized even without additional treatment.

ASSOCIATED CONTENT

Supporting Information.

The following files are available free of charge.

- Description of sample preparation and data processing. (PDF)

AUTHOR INFORMATION

Corresponding Author

* E-mail: peter.vesborg@fysik.dtu.dk

Author Contributions

The manuscript was written through contributions of all authors. All authors have given approval to the final version of the manuscript.

Funding Sources

This project has received funding from the European Research Council (ERC) under the European Union's Horizon 2020 research and innovation programme (grant agreement No 758495).

The Center for Visualizing Catalytic Processes is sponsored by the Danish National Research Foundation (Grant no. DNRF146).



European Research Council
Established by the European Commission

Notes

The authors declare no competing financial interest.

ACKNOWLEDGMENT

Sample fabrication was performed at DTU Nanolab – National Centre for Nano Fabrication and Characterization and DTU Physics - Center for Nanostructured Graphene. We are thankful for the valuable help received by Tim Booth, Peter Bøggild, Jonas Michael-Lindhard, Jakob Birkedal Wagner, and in general the technical staff at DTU Nanolab and DTU NANOMADE. Equipment situated at DTU Physics - ATOMICAR and DTU Physics – VISION were used to characterize the samples. We are grateful for the technical support of Sven Ullmann and Sebastian Pirel Fredsgaard Jespersen from Haldor Topsoe A/S.

ABBREVIATIONS

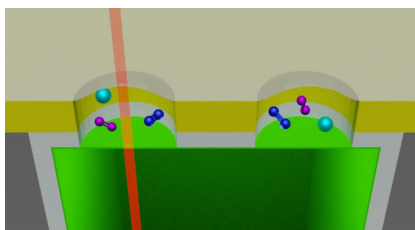
AFM, Atomic Force Microscopy; EEL, Electron Energy Loss; EELS, Electron Energy Loss Spectroscopy; TEM, Transmission Electron Microscopy.

REFERENCES

- [1] L. Wang, L. W. Drahushuk, L. Cantley, S. P. Koenig, X. Liu, J. Pellegrino, M. S. Strano, and J. S. Bunch, "Molecular valves for controlling gas phase transport made from discrete ångström-sized pores in graphene," *Nature nanotechnology*, vol. 10, no. 9, pp. 785-790, 2015.
- [2] J. S. Bunch, S. S. Verbridge, J. S. Alden, A. M. Van Der Zande, J. M. Parpia, H. G. Craighead, and P. L. McEuen, "Impermeable atomic membranes from graphene sheets," *Nano letters*, vol. 8, no. 8, pp. 2458-2462, 2008.
- [3] M. Lee, D. Davidovikj, B. Sajadi, M. Šiškins, F. Alijani, H. S. van der Zant, and P. G. Steeneken, "Sealing graphene nanodrums," *Nano letters*, vol. 19, no. 8, pp. 5313-5318, 2019.
- [4] Y. Manzanares-Negro, P. Ares, M. Jaafar, G. Lopez-Polin, C. Gomez-Navarro, and J. Gomez-Herrero, "Improved graphene blisters by ultrahigh pressure sealing," *ACS Applied Materials & Interfaces*, vol. 12, no. 33, pp. 37750-37756, 2020.
- [5] P. Sun, Q. Yang, W. Kuang, Y. Stebunov, W. Xiong, J. Yu, R. Nair, M. Katsnelson, S. Yuan, I. Grigorieva, M. Lozada-Hidalgo, F. Wang, and A. Geim, "Limits on gas impermeability of graphene," *Nature*, vol. 579, no. 7798, pp. 229-232, 2020.
- [6] S. P. Koenig, L. Wang, J. Pellegrino, and J. S. Bunch, "Selective molecular sieving through porous graphene," *Nature nanotechnology*, vol. 7, no. 11, pp. 728-732, 2012.
- [7] S. P. Koenig, N. G. Boddeti, M. L. Dunn, and J. S. Bunch, "Ultrastrong adhesion of graphene membranes," *Nature nanotechnology*, vol. 6, no. 9, p. 543, 2011.
- [8] V. Berry, "Impermeability of graphene and its applications," *Carbon*, vol. 62, pp. 1-10, 2013.
- [9] H. Tian, Y. Shu, X.-F. Wang, M. A. Mohammad, Z. Bie, Q.-Y. Xie, C. Li, W.-T. Mi, Y. Yang, and T.-L. Ren, "A graphene-based resistive pressure sensor with record-high sensitivity in a wide pressure range," *Scientific reports*, vol. 5, no. 1, pp. 1-6, 2015.
- [10] A. D. Smith, F. Niklaus, A. Paussa, S. Schröder, A. C. Fischer, M. Sterner, S. Wagner, S. Vaziri, F. Forsberg, and D. Esseni, "Piezoresistive properties of suspended graphene membranes under uniaxial and biaxial strain in nanoelectromechanical pressure sensors," *ACS nano*, vol. 10, no. 11, pp. 9879-9886, 2016.
- [11] A. D. Smith, S. Vaziri, F. Niklaus, A. C. Fischer, M. Sterner, A. Delin, M. Östling, and M. C. Lemme, "Pressure sensors based on suspended graphene membranes," *Solid-State Electronics*, vol. 88, pp. 89-94, 2013.
- [12] A. Hurst, S. Lee, N. Petrone, J. VanDeWeert, A. Van der Zande, and J. Hone, "A transconductive graphene pressure sensor," in *2013 Transducers & Eurosensors XXVII: The 17th International Conference on Solid-State Sensors, Actuators and Microsystems (TRANSDUCERS & EUROSENSORS XXVII)*, 2013: IEEE, pp. 586-589.
- [13] G. Dunn, V. P. Adiga, T. Pham, C. Bryant, D. J. Horton-Bailey, J. N. Belling, B. LaFrance, J. A. Jackson, H. R. Barzegar, and J. M. Yuk, "Graphene-Sealed Flow Cells for In Situ Transmission Electron Microscopy of Liquid Samples," *ACS nano*, vol. 14, no. 8, pp. 9637-9643, 2020.
- [14] J. Park, H. Park, P. Ercius, A. F. Pegoraro, C. Xu, J. W. Kim, S. H. Han, and D. A. Weitz, "Direct observation of wet biological samples by graphene liquid cell transmission electron microscopy," *Nano letters*, vol. 15, no. 7, pp. 4737-4744, 2015.

- [15] N. Mohanty, M. Fahrenholtz, A. Nagaraja, D. Boyle, and V. Berry, "Impermeable graphenic encasement of bacteria," *Nano letters*, vol. 11, no. 3, pp. 1270-1275, 2011.
- [16] J. M. Yuk, J. Park, P. Ercius, K. Kim, D. J. Hellebusch, M. F. Crommie, J. Y. Lee, A. Zettl, and A. P. Alivisatos, "High-resolution EM of colloidal nanocrystal growth using graphene liquid cells," *Science*, vol. 336, no. 6077, pp. 61-64, 2012.
- [17] H. Rasool, G. Dunn, A. Fathalizadeh, and A. Zettl, "Graphene-sealed Si/SiN cavities for high-resolution in situ electron microscopy of nano-confined solutions," *physica status solidi (b)*, vol. 253, no. 12, pp. 2351-2354, 2016.
- [18] D. J. Kelly, M. Zhou, N. Clark, M. J. Hamer, E. A. Lewis, A. M. Rakowski, S. J. Haigh, and R. V. Gorbachev, "Nanometer resolution elemental mapping in graphene-based TEM liquid cells," *Nano letters*, vol. 18, no. 2, pp. 1168-1174, 2018.
- [19] S. Vendelbo, P. Kooyman, J. Creemer, B. Morana, L. Mele, P. Dona, B. Nelissen, and S. Helveg, "Method for local temperature measurement in a nanoreactor for in situ high-resolution electron microscopy," *Ultramicroscopy*, vol. 133, pp. 72-79, 2013.
- [20] P. A. Crozier and S. Chenna, "In situ analysis of gas composition by electron energy-loss spectroscopy for environmental transmission electron microscopy," *Ultramicroscopy*, vol. 111, no. 3, pp. 177-185, 2011.
- [21] J. Jinschek and S. Helveg, "Image resolution and sensitivity in an environmental transmission electron microscope," *Micron*, vol. 43, no. 11, pp. 1156-1168, 2012.
- [22] M. Takeuchi, S. Muto, T. Tanabe, S. Arai, and T. Kuroyanagi, "Damage process in electron-irradiated graphite studied by transmission electron microscopy. II. Analysis of extended energy-loss fine structure of highly oriented pyrolytic graphite," *Philosophical Magazine A*, vol. 76, no. 3, pp. 691-700, 1997.

For Table of Contents Only



Bibliography

- [1] Statistics Denmark, “Employment in agriculture by type, unit, region and time.” <https://www.statistikbanken.dk/BDF307>, Accessed 09-21-2021.
- [2] Danish Agriculture & Food Council, “Facts & Figures: Denmark - a Food and Farming Country.” <https://agricultureandfood.dk/prices-and-statistics/annual-statistics>, 2019.
- [3] Maddison Project Database, version 2020. Bolt, Jutta and Jan Luiten van Zanden, “Maddison style estimates of the evolution of the world economy. A new 2020 update.” <https://www.rug.nl/ggdc/historicaldevelopment/maddison/releases/maddison-project-database-2020?lang=en>, 2020.
- [4] bp, “Statistical Review of World Energy 2021.” <https://www.bp.com/en/global/corporate/energy-economics/statistical-review-of-world-energy.html>, 2021.
- [5] IPCC, “Climate Change 2021: The Physical Science Basis. Contribution of Working Group I to the Sixth Assessment Report of the Intergovernmental Panel on Climate Change [Masson-Delmotte, V., P. Zhai, A. Pirani, S.L. Connors, C. Péan, S. Berger, N. Caud, Y. Chen, L. Goldfarb, M.I. Gomis, M. Huang, K. Leitzell, E. Lonnoy, J.B.R. Matthews, T.K. Maycock, T. Waterfield, O. Yelekçi, R. Yu, and B. Zhou (eds.)]. Cambridge University Press. In Press.” <https://www.ipcc.ch/report/ar6/wg1/#InteractiveAtlas>, 2021.
- [6] European Commission website, “European climate law.” https://ec.europa.eu/clima/policies/eu-climate-action/law_en, Accessed 09-22-2021.
- [7] A. Belke, F. Dobnik, and C. Dreger, “Energy consumption and economic growth: New insights into the cointegration relationship,” *Energy Economics*, vol. 33, no. 5, pp. 782–789, 2011.
- [8] S. Blundell and K. M. Blundell, *Concepts in thermal physics*. Oxford Univ. Press, 2006.
- [9] Z. W. Seh, J. Kibsgaard, C. F. Dickens, I. Chorkendorff, J. K. Nørskov, and T. F. Jaramillo, “Combining theory and experiment in electrocatalysis: Insights into materials design,” *Science*, vol. 355, no. 6321, p. eaad4998, 2017.

- [10] I. Chorkendorff and J. W. Niemantsverdriet, *Concepts of modern catalysis and kinetics*. Wiley-VCH, 2003.
- [11] R. Daiyan, I. Macgill, and R. Amal, “Opportunities and challenges for renewable power-to-x,” *Acs Energy Letters*, vol. 5, no. 12, pp. 3843–3847, 2020.
- [12] P. C. K. Vesborg and T. F. Jaramillo, “Addressing the terawatt challenge: Scalability in the supply of chemical elements for renewable energy,” *R S C Advances*, vol. 2, no. 21, pp. 7933–7947, 2012.
- [13] F. Abild-Pedersen, J. Greeley, F. Studt, J. Rossmeisl, T. R. Munter, P. G. Moses, E. Skúlason, T. Bligaard, and J. K. Nørskov, “Scaling properties of adsorption energies for hydrogen-containing molecules on transition-metal surfaces,” *Phys. Rev. Lett.*, vol. 99, p. 016105, Jul 2007.
- [14] G. Jones, T. Bligaard, F. Abild-Pedersen, and J. Nørskov, “Using scaling relations to understand trends in the catalytic activity of transition metals,” *Journal of physics. Condensed matter : an Institute of Physics journal*, vol. 20, p. 064239, 02 2008.
- [15] J. Greeley, “Theoretical heterogeneous catalysis: Scaling relationships and computational catalyst design,” *Annual Review of Chemical and Biomolecular Engineering*, vol. 7, no. 1, pp. 605–635, 2016. PMID: 27088666.
- [16] A. Vojvodic and J. K. Nørskov, “New design paradigm for heterogeneous catalysts,” *National Science Review*, vol. 2, pp. 140–143, 04 2015.
- [17] A. Khorshidi, J. Violet, J. Hashemi, and A. A. Peterson, “How strain can break the scaling relations of catalysis,” *Nature Catalysis*, vol. 1, pp. 263–268, 2018.
- [18] J. K. Nørskov, T. Bligaard, J. Rossmeisl, and C. H. Christensen, “Towards the computational design of solid catalysts.,” *Nature chemistry*, vol. 1 1, pp. 37–46, 2009.
- [19] R. Michalsky, Y.-J. Zhang, A. J. Medford, and A. A. Peterson, “Departures from the adsorption energy scaling relations for metal carbide catalysts,” *Journal of Physical Chemistry C*, vol. 118, pp. 13026–13034, 2014.
- [20] W. Gao, Z. D. Hood, and M. Chi, “Interfaces in heterogeneous catalysts: Advancing mechanistic understanding through atomic-scale measurements,” *Accounts of Chemical Research*, vol. 50, no. 4, pp. 787–795, 2017.
- [21] J. B. Sambur and P. Chen, “Approaches to single-nanoparticle catalysis,” *Annual Review of Physical Chemistry*, vol. 65, no. 1, pp. 395–422, 2014. PMID: 24423372.
- [22] J. K. Nørskov, T. Bligaard, B. H. Larsen, F. Abild-Pedersen, I. Chorkendorff, and C. H. Christensen, “The nature of the active site in heterogeneous metal catalysis,” *Chemical Society Reviews*, vol. 37, no. 10, pp. 2163–2171, 2008.

- [23] H. Wang and J. Lu, "A review on particle size effect in metal-catalyzed heterogeneous reactions," *Chinese Journal of Chemistry*, vol. 38, no. 11, pp. 1422–1444, 2020.
- [24] M. Haruta, S. Tsubota, T. Kobayashi, H. Kageyama, M. Genet, and B. Delmon, "Low-temperature oxidation of CO over gold supported on TiO₂, Fe₂O₃, and Co₃O₄," *Journal of Catalysis*, vol. 144, no. 1, pp. 175–192, 1993.
- [25] L. Liu and A. Corma, "Metal catalysts for heterogeneous catalysis: From single atoms to nanoclusters and nanoparticles," *Chemical Reviews*, vol. 118, no. 10, pp. 4981–5079, 2018.
- [26] P. L. Hansen, J. B. Wagner, S. Helveg, J. R. Rostrup-Nielsen, B. S. Clausen, and H. Topsøe, "Atom-resolved imaging of dynamic shape changes in supported copper nanocrystals," *Science*, vol. 295, no. 5562, pp. 2053–2055, 2002.
- [27] S. B. Vendelbo, C. F. Elkjær, H. Falsig, I. Puspitasari, P. Dona, L. Mele, B. Morana, B. J. Nelissen, R. Van Rijn, J. F. Creemer, P. J. Kooyman, and S. Helveg, "Visualization of oscillatory behaviour of Pt nanoparticles catalysing CO oxidation," *Nature Materials*, vol. 13, no. 9, pp. 884–890, 2014.
- [28] G. D. Barmparis, Z. Lodziana, N. Lopez, and I. N. Remediakis, "Nanoparticle shapes by using Wulff constructions and first-principles calculations," *Beilstein Journal of Nanotechnology*, vol. 6, no. 1, pp. 361–368, 2015.
- [29] F. Tao and P. A. Crozier, "Atomic-scale observations of catalyst structures under reaction conditions and during catalysis," *Chemical Reviews*, vol. 116, no. 6, pp. 3487–3539, 2016.
- [30] M. Bertau, H. Offermanns, L. Plass, F. Schmidt, and H. J. Wernicke, *Methanol: The basic chemical and energy feedstock of the future: Asinger's vision today*. Springer Berlin Heidelberg, 2014.
- [31] A. de Klerk, "10 - transport fuel: Biomass-, coal-, gas- and waste-to-liquids processes," in *Future Energy (Third Edition)* (T. M. Letcher, ed.), pp. 199–226, Elsevier, third edition ed., 2020.
- [32] W. Xu, J. Kong, Y.-T. E. Yeh, and P. Chen, "Single-molecule nanocatalysis reveals heterogeneous reaction pathways and catalytic dynamics," *Nature materials*, vol. 7, no. 12, pp. 992–6, 2008.
- [33] S. Levin, J. Fritzsche, S. Nilsson, A. Runemark, B. Dhokale, H. Ström, H. Sundén, C. Langhammer, and F. Westerlund, "A nanofluidic device for parallel single nanoparticle catalysis in solution," *Nature Communications*, vol. 10, 09 2019.

- [34] J. Gao, H. Su, and W. Wang, "A microwell array-based approach for studying single nanoparticle catalysis with high turnover frequency," *The Journal of Chemical Physics*, vol. 155, no. 7, p. 071101, 2021.
- [35] S. C. Lai, P. V. Dudin, J. V. MacPherson, and P. R. Unwin, "Visualizing zeptomole (electro)catalysis at single nanoparticles within an ensemble," *Journal of the American Chemical Society*, vol. 133, no. 28, pp. 10744–10747, 2011.
- [36] D. A. Shapiro, Y. S. Yu, T. Tyliczszak, J. Cabana, R. Celestre, W. Chao, K. Kaznatcheev, A. L. Kilcoyne, F. Maia, S. Marchesini, Y. S. Meng, T. Warwick, L. L. Yang, and H. A. Padmore, "Chemical composition mapping with nanometre resolution by soft x-ray microscopy," *Nature Photonics*, vol. 8, no. 10, pp. 765–769, 2014.
- [37] S. Alekseeva, I. I. Nedrygailov, and C. Langhammer, "Single particle plasmonics for materials science and single particle catalysis," *Acs Photonics*, vol. 6, no. 6, pp. 1319–1330, 2019.
- [38] T. Hartman, C. S. Wondergem, N. Kumar, A. van den Berg, and B. M. Weckhuysen, "Surface- and tip-enhanced raman spectroscopy in catalysis," *Journal of Physical Chemistry Letters*, vol. 7, no. 8, pp. 1570–1584, 2016.
- [39] Y. Suchorski, J. Zeininger, S. Buhr, M. Raab, M. Stoeger-Pollach, J. Bernardi, H. Groenbeck, and G. Rupprechter, "Resolving multifrequential oscillations and nanoscale interfacet communication in single-particle catalysis," *SCIENCE*, vol. 372, pp. 1314+, JUN 18 2021.
- [40] J. F. Creemer, F. Santagata, B. Morana, L. Mele, T. Alan, E. Iervolino, G. Pandraud, and P. M. Sarro, "An all-in-one nanoreactor for high-resolution microscopy on nanomaterials at high pressures," *Proceedings of the Ieee International Conference on Micro Electro Mechanical Systems (mems)*, pp. 1103–1106, 2011.
- [41] J. F. Creemer, S. Helveg, P. J. Kooyman, A. M. Molenbroek, H. W. Zandbergen, and P. M. Sarro, "A mems reactor for atomic-scale microscopy of nanomaterials under industrially relevant conditions," *Journal of Microelectromechanical Systems*, vol. 19, no. 2, pp. 254–264, 2010.
- [42] L. Allard, W. Bigelow, S. Overbury, D. Nackashi, and J. Damiano, "Development of a novel environmental cell for in-situ gas reaction experiments via aberration-corrected stem imaging," *Microscopy and Microanalysis*, vol. 16, no. S2, pp. 296–297, 2010.
- [43] S. Zhang, P. N. Plessow, J. J. Willis, S. Dai, M. Xu, G. W. Graham, M. Cargnello, F. Abild-Pedersen, and X. Pan, "Dynamical observation and detailed description of catalysts under strong metal-support interaction," *Nano Letters*, vol. 16, no. 7, pp. 4528–4534, 2016.

- [44] M. Schumann, M. R. Nielsen, T. E. L. Smitshuysen, T. W. Hansen, C. D. Damsgaard, A.-C. A. Yang, M. Cargnello, J.-D. Grunwaldt, A. D. Jensen, and J. M. Christensen, “Rationalizing an unexpected structure sensitivity in heterogeneous catalysis—co hydrogenation over rh as a case study,” *Acs Catalysis*, vol. 11, no. 9, pp. 5189–5201, 2021.
- [45] D. B. Williams and C. B. Carter, *Transmission electron microscopy: A textbook for materials science*. Springer US, 2009.
- [46] M. J. N. Sibley, *Introduction to Electromagnetism*. CRC Press, 2021.
- [47] J. I. Goldstein, D. E. Newbury, J. R. Michael, N. W. Ritchie, J. H. J. Scott, and D. C. Joy, *Scanning electron microscopy and x-ray microanalysis*. Springer New York, 2017.
- [48] J. Jinschek and S. Helveg, “Image resolution and sensitivity in an environmental transmission electron microscope,” *Micron*, vol. 43, no. 11, pp. 1156–1168, 2012. In situ TEM.
- [49] P. Tiemeijer, “Titan condenser manual,” 2005.
- [50] R. Egerton, “Radiation damage to organic and inorganic specimens in the tem,” *Micron*, vol. 119, pp. 72–87, 2019.
- [51] R. F. Egerton and R. Egerton, *Electron energy-loss spectroscopy in the electron microscope*. Springer, 2011.
- [52] Gatan Corporate, “EELS Atlas.” <https://eels.info/atlas>, Accessed 12-03-2021.
- [53] Gatan, “GIF Tridiem - Owner’s Manual,” 2004.
- [54] FEI Company, “The Quanta FEG 200, 400, 600 User’s Operation Manual.” <https://engineering.unl.edu/downloads/files/UserManual-Quanta200SEM-sm.pdf>, 2003.
- [55] L. Reimer, *Scanning electron microscopy. Physics of image formation and microanalysis*. Springer-Verlag, 1998.
- [56] B. Voigtländer, *Scanning probe microscopy : atomic force microscopy and scanning tunneling microscopy*. Springer, 2015.
- [57] J. P. Cleveland, B. Anczykowski, A. E. Schmid, and V. B. Elings, “Energy dissipation in tapping-mode atomic force microscopy,” *Applied Physics Letters*, vol. 72, no. 20, pp. 2613–2615, 1998.
- [58] Nanosurf, “Nanosurf FlexAFM - Operating Instructions.”

- [59] H. Hölscher and U. D. Schwarz, “Theory of amplitude modulation atomic force microscopy with and without q-control,” *International Journal of Non-linear Mechanics*, vol. 42, no. 4, pp. 608–625, 2007.
- [60] DTU NANOLAB, “DTU NANOLAB webpage.” <https://www.nanolab.dtu.dk/english>, accessed 2021/11/01.
- [61] H. H. Gatzten, V. Saile, and J. Leuthold, *Micro and nano fabrication: Tools and processes*. Springer Berlin Heidelberg, 2015.
- [62] S. Franssila, *Introduction to Microfabrication*. John Wiley & Sons, Ltd, 2010.
- [63] K. S. Novoselov, A. K. Geim, S. V. Morozov, D. Jiang, Y. Zhang, S. V. Dubonos, I. V. Grigorieva, and A. A. Firsov, “Electric field in atomically thin carbon films,” *Science*, vol. 306, no. 5696, pp. 666–669, 2004.
- [64] G. F. Schneider, V. E. Calado, H. Zandbergen, L. M. K. Vandersypen, and C. Dekker, “Wedging transfer of nanostructures,” *Nano Letters*, vol. 10, no. 5, pp. 1912–1916, 2010.
- [65] H. C. Lee, W. W. Liu, S. P. Chai, A. R. Mohamed, A. Aziz, C. S. Khe, N. M. Hidayah, and U. Hashim, “Review of the synthesis, transfer, characterization and growth mechanisms of single and multilayer graphene,” *Rsc Advances*, vol. 7, no. 26, pp. 15644–15693, 2017.
- [66] J. y. Sun, Y. s. Lian, Y. m. Li, X. t. He, and Z. l. Zheng, “Closed-form solution of elastic circular membrane with initial stress under uniformly-distributed loads: Extended hencky solution,” *Zamm Zeitschrift Fur Angewandte Mathematik Und Mechanik*, vol. 95, no. 11, pp. 1335–1341, 2015.
- [67] J. J. Vlassak and W. D. Nix, “A new bulge test technique for the determination of young’s modulus and poisson’s ratio of thin films,” *Journal of Materials Research*, vol. 7, no. 12, pp. 3242–3249, 1992.
- [68] J. Hu, L. Yu, J. Deng, Y. Wang, K. Cheng, C. Ma, Q. Zhang, W. Wen, S. Yu, Y. Pan, J. Yang, H. Ma, F. Qi, Y. Wang, Y. Zheng, M. Chen, R. Huang, S. Zhang, Z. Zhao, J. Mao, X. Meng, Q. Ji, G. Hou, X. Han, X. Bao, Y. Wang, and D. Deng, “Sulfur vacancy-rich mos₂ as a catalyst for the hydrogenation of co₂ to methanol,” *Nature Catalysis*, vol. 4, no. 3, pp. 242–250, 2021.
- [69] S. G. Jadhav, P. D. Vaidya, B. M. Bhanage, and J. B. Joshi, “Catalytic carbon dioxide hydrogenation to methanol: A review of recent studies,” *Chemical Engineering Research and Design*, vol. 92, no. 11, pp. 2557–2567, 2014.
- [70] K. Ueda, T. Kawasaki, H. Hasegawa, T. Tanji, and M. Ichihashi, “First observation of dynamic shape changes of a gold nanoparticle catalyst under reaction gas environment by transmission electron microscopy,” *Surface and Interface Analysis*, vol. 40, no. 13, pp. 1725–1727, 2008.

- [71] N. de Jonge, W. C. Bigelow, and G. M. Veith, "Atmospheric pressure scanning transmission electron microscopy," *Nano Letters*, vol. 10, no. 3, pp. 1028–1031, 2010.
- [72] C. Kittel and H. Kroemer, *Thermal physics*. Freeman,, 1980.
- [73] J. S. Bunch, S. S. Verbridge, J. S. Alden, A. M. Van Der Zande, J. M. Parpia, H. G. Craighead, and P. L. McEuen, "Impermeable atomic membranes from graphene sheets," *Nano Letters*, vol. 8, no. 8, pp. 2458–2462, 2008.
- [74] P. Z. Sun, Q. Yang, W. J. Kuang, Y. V. Stebunov, W. Q. Xiong, J. Yu, R. R. Nair, M. I. Katsnelson, S. J. Yuan, I. V. Grigorieva, M. Lozada-Hidalgo, F. C. Wang, and A. K. Geim, "Limits on gas impermeability of graphene," *Nature*, vol. 579, no. 7798, pp. 229–232, 2020.
- [75] A. D. Smith, F. Niklaus, A. Paussa, S. Schröder, A. C. Fischer, M. Sterner, S. Wagner, S. Vaziri, F. Forsberg, D. Esseni, M. Östling, and M. C. Lemme, "Piezoresistive properties of suspended graphene membranes under uniaxial and biaxial strain in nanoelectromechanical pressure sensors," *Acs Nano*, vol. 10, no. 11, pp. 9879–9886, 2016.
- [76] A. D. Smith, S. Vaziri, F. Niklaus, A. C. Fischer, M. Sterner, A. Delin, M. Östling, and M. C. Lemme, "Pressure sensors based on suspended graphene membranes," *Solid-state Electronics*, vol. 88, pp. 89–94, 2013.
- [77] A. M. Hurst, S. Lee, N. Petrone, J. Vandeweert, A. M. Van Der Zande, and J. Hone, "A transconductive graphene pressure sensor," *2013 Transducers and Eurosensors Xviii: the 17th International Conference on Solid-state Sensors, Actuators and Microsystems, Transducers and Eurosensors 2013*, pp. 586–589, 2013.
- [78] G. Dunn, V. P. Adiga, T. Pham, C. Bryant, D. J. Horton-Bailey, J. N. Belling, B. Lafrance, J. A. Jackson, H. R. Barzegar, J. M. Yuk, S. Aloni, M. F. Crommie, and A. Zettl, "Graphene-sealed flow cells for in situ transmission electron microscopy of liquid samples," *Acs Nano*, vol. 14, no. 8, pp. 9637–9643, 2020.
- [79] J. Park, H. Park, P. Ercius, A. F. Pegoraro, C. Xu, J. W. Kim, S. H. Han, and D. A. Weitz, "Direct observation of wet biological samples by graphene liquid cell transmission electron microscopy," *Nano Letters*, vol. 15, no. 7, pp. 4737–4744, 2015.
- [80] N. Mohanty, M. Fahrenholtz, A. Nagaraja, D. Boyle, and V. Berry, "Impermeable graphenic encasement of bacteria," *Nano Letters*, vol. 11, no. 3, pp. 1270–1275, 2011.
- [81] J. M. Yuk, J. Park, P. Ercius, K. Kim, D. J. Hellebusch, M. F. Crommie, J. Y. Lee, A. Zettl, and A. P. Alivisatos, "High-resolution em of colloidal nanocrystal growth using graphene liquid cells," *Science*, vol. 336, no. 6077, pp. 61–64, 2012.

- [82] H. Rasool, G. Dunn, A. Fathalizadeh, and A. Zettl, "Graphene-sealed si/sin cavities for high-resolution in situ electron microscopy of nano-confined solutions," *Physica Status Solidi (b) Basic Research*, vol. 253, no. 12, pp. 2351–2354, 2016.
- [83] D. J. Kelly, M. Zhou, N. Clark, M. J. Hamer, E. A. Lewis, A. M. Rakowski, S. J. Haigh, and R. V. Gorbachev, "Nanometer resolution elemental mapping in graphene-based tem liquid cells," *Nano Letters*, vol. 18, no. 2, pp. 1168–1174, 2018.
- [84] L. Wang, L. W. Drahushuk, L. Cantley, S. P. Koenig, X. Liu, J. Pellegrino, M. S. Strano, and J. Scott Bunch, "Molecular valves for controlling gas phase transport made from discrete ångström-sized pores in graphene," *Nature Nanotechnology*, vol. 10, no. 9, pp. 785–790, 2015.
- [85] S. P. Koenig, L. Wang, J. Pellegrino, and J. S. Bunch, "Selective molecular sieving through porous graphene," *Nature Nanotechnology*, vol. 7, no. 11, pp. 728–732, 2012.
- [86] S. P. Koenig, N. G. Boddeti, M. L. Dunn, and J. S. Bunch, "Ultrastrong adhesion of graphene membranes," *Nature Nanotechnology*, vol. 6, no. 9, pp. 543–546, 2011.
- [87] Y. Manzanares-Negro, P. Ares, M. Jaafar, G. López-Polín, C. Gómez-Navarro, and J. Gómez-Herrero, "Improved graphene blisters by ultrahigh pressure sealing," *Acs Applied Materials and Interfaces*, vol. 12, no. 33, pp. 37750–37756, 2020.
- [88] J. D. Whittaker, E. D. Minot, D. M. Tanenbaum, P. L. McEuen, and R. C. Davis, "Measurement of the adhesion force between carbon nanotubes and a silicon dioxide substrate," *Nano Letters*, vol. 6, no. 5, pp. 953–957, 2006.
- [89] P. Blake, E. W. Hill, A. H. Castro Neto, K. S. Novoselov, D. Jiang, R. Yang, T. J. Booth, and A. K. Geim, "Making graphene visible," *Applied Physics Letters*, vol. 91, no. 6, p. 063124, 2007.
- [90] W. Gao, P. Xiao, G. Henkelman, K. M. Liechti, and R. Huang, "Interfacial adhesion between graphene and silicon dioxide by density functional theory with van der waals corrections," *Journal of Physics D: Applied Physics*, vol. 47, no. 25, p. 255301, 2014.
- [91] V. Dimitrov and T. Komatsu, "Classification of simple oxides: A polarizability approach," *Journal of Solid State Chemistry*, vol. 163, no. 1, pp. 100–112, 2002.
- [92] S. I. Raider, R. Flitsch, J. A. Aboaf, and W. A. Pliskin, "Surface oxidation of silicon nitride films," *J Electrochem Soc*, vol. 123, no. 4, pp. 560–565, 1976.

- [93] A. CARIM, M. DOVEK, C. QUATE, R. SINCLAIR, and C. VORST, "High-resolution electron-microscopy and scanning tunneling microscopy of native oxides on silicon," *Science*, vol. 237, no. 4815, pp. 630–633, 1987.
- [94] C. H. Lui, L. Liu, K. F. Mak, G. W. Flynn, and T. F. Heinz, "Ultraflat graphene," *Nature*, vol. 462, no. 7271, pp. 339–341, 2009.
- [95] T. Y. Kwon, M. Ramachandran, and J. G. Park, "Scratch formation and its mechanism in chemical mechanical planarization (cmp)," *Friction*, vol. 1, no. 4, pp. 279–305, 2013.
- [96] M. Lee, D. Davidovikj, B. Sajadi, M. Šiškins, F. Alijani, H. S. Van Der Zant, and P. G. Steeneken, "Sealing graphene nanodrums," *Nano Letters*, vol. 19, no. 8, pp. 5313–5318, 2019.
- [97] J. Yeom, Y. Wu, J. C. Selby, and M. A. Shannon, "Maximum achievable aspect ratio in deep reactive ion etching of silicon due to aspect ratio dependent transport and the microloading effect," *Journal of Vacuum Science and Technology B: Microelectronics and Nanometer Structures*, vol. 23, no. 6, pp. 2319–2329, 2005.
- [98] J. Chu and D. Zhang, "Mechanical characterization of thermal sio2 microbeams through tensile testing," *Journal of Micromechanics and Microengineering*, vol. 19, no. 9, p. 095020, 2009.
- [99] T. Tsuchiya, "Tensile testing of silicon thin films," *Fatigue and Fracture of Engineering Materials and Structures*, vol. 28, no. 8, pp. 665–674, 2005.
- [100] M. JUN, Y. KIM, M. HAN, J. KIM, and K. KIM, "Polycrystalline silicon oxidation method improving surface-roughness at the oxide polycrystalline silicon interface," *Applied Physics Letters*, vol. 66, no. 17, pp. 2206–2208, 1995.
- [101] D. L. Goldfarb, A. P. Mahorowala, G. M. Gallatin, K. E. Petrillo, K. Temple, M. Angelopoulos, S. Rasgon, H. H. Sawin, S. D. Allen, M. C. Lawson, and R. W. Kwong, "Effect of thin-film imaging on line edge roughness transfer to underlayers during etch processes," *Journal of Vacuum Science and Technology B: Microelectronics and Nanometer Structures*, vol. 22, no. 2, pp. 647–653, 2004.
- [102] V. Ishchuk, B. E. Volland, M. Hauguth, M. Cooke, and I. W. Rangelow, "Charging effect simulation model used in simulations of plasma etching of silicon," *Journal of Applied Physics*, vol. 112, no. 8, p. 084308, 2012.
- [103] L. Mele, S. Konings, P. Dona, F. Evertz, C. Mitterbauer, P. Faber, R. Schampers, and J. R. Jinschek, "A mems-based heating holder for the direct imaging of simultaneous in-situ heating and biasing experiments in scanning/transmission electron microscopes," *Microscopy Research and Technique*, vol. 79, no. 4, pp. 239–250, 2016.

- [104] C. W. Lee, Y. Ikematsu, and D. Shindo, "Measurement of mean free paths for inelastic electron scattering of si and sio₂," *Journal of Electron Microscopy*, vol. 51, no. 3, pp. 143–148, 2002.
- [105] J. N. Hansen, H. Prats, K. K. Toudahl, N. Mørch Secher, K. Chan, J. Kibsgaard, and I. Chorkendorff, "Is there anything better than pt for her?," *Acs Energy Letters*, vol. 6, no. 4, pp. 1175–1180, 2021.
- [106] M. D. Fischbein and M. Drndić, "Electron beam nanosculpting of suspended graphene sheets," *Applied Physics Letters*, vol. 93, no. 11, p. 113107, 2008.
- [107] B. Sommer, J. Sonntag, A. Ganczarczyk, D. Braam, G. Prinz, A. Lorke, and M. Geller, "Electron-beam induced nano-etching of suspended graphene," *Scientific Reports*, vol. 5, no. 1, p. 7781, 2015.
- [108] P. A. Crozier and S. Chenna, "In situ analysis of gas composition by electron energy-loss spectroscopy for environmental transmission electron microscopy," *Ultramicroscopy*, vol. 111, no. 3, pp. 177–185, 2011.
- [109] M. Takeuchi, S. Muto, T. Tanabe, S. Arai, and T. Kuroyanagi, "Damage process in electron-irradiated graphite studied by transmission electron microscopy. ii. analysis of extended energy-loss fine structure of highly oriented pyrolytic graphite," *Philosophical Magazine A: Physics of Condensed Matter, Structure, Defects and Mechanical Properties*, vol. 76, no. 3, pp. 691–700, 1997.
- [110] L. F. Allard, W. C. Bigelow, S. A. Bradley, and J. Liu, "A novel heating technology for ultra-high resolution imaging in electron microscopes," *Microscopy Today*, vol. 17, no. 04, p. 50, 2009.
- [111] D. Alsteens, V. Dupres, S. Yunus, J.-P. Latgé, J. J. Heinisch, and Y. F. Dufrène, "High-resolution imaging of chemical and biological sites on living cells using peak force tapping atomic force microscopy," *Langmuir*, vol. 28, no. 49, pp. 16738–16744, 2012.
- [112] J. S. Bunch, A. M. Van Der Zande, S. S. Verbridge, I. W. Frank, D. M. Tanenbaum, J. M. Parpia, H. G. Craighead, and P. L. McEuen, "Electromechanical resonators from graphene sheets," *Science*, vol. 315, no. 5811, pp. 490–493, 2007.